APPLICATION OF MULTI-INPUT MULTI-OUTPUT FEEDBACK CONTROL FOR F-16
VENTRAL FIN BUFFET ALLEVIATION USING PIEZOELECTRIC ACTUATORS

THESIS

Tomoyuki D. Ono, Captain, USAF

AFIT/GAE/ENY/12-M31

Application of Multi-Input Multi-Output Feedback Control for F-16 Ventral Fin Buffet Alleviation Using Piezoelectric Actuators

THESIS

Presented to the Faculty

Department of Aeronautics and Astronautics

Graduate School of Engineering and Management

Air Force Institute of Technology

Air University

Air Education and Training Command

In Partial Fulfillment of the Requirements for the

Degree of Master of Science in Aeronautical Engineering

Tomoyuki D. Ono, MS

Captain, USAF

March 2012

Application of Multi-Input Multi-Output Feedback Control for F-16 Ventral Fin Buffet Alleviation Using Piezoelectric Actuators

Tomoyuki D. Ono, MS

Captain, USAF

Approved:

/signed/	5 Mar 2012
Richard G. Cobb, PhD (Chairman)	Date
/signed/	5 Mar 2012
Bradley S. Liebst, PhD (Member)	Date
/signed/	5 Mar 2012
Lt Col Timothy R. Jorris, PhD (Member)	Date

AFIT/GAE/ENY/12-M31

Abstract

Efforts to reduce buffet induced vibrations and structural damage has been a continuing effort for years. Aircraft structures, especially, are prone to buffeting due to the unpredictable aerodynamic forces that interact with the structure, sometimes leading to flutter and failure. The commonly used methods to combat these situations have been to use passive methods such as adding more material to strengthen the structure or change the characteristic of the aerodynamic forces that cause the buffeting. An alternate solution is to use an active method by using smart materials and feedback loops to reduce the magnitude of the vibrations. The ACTIVE FIN research used the Block 15 F-16D ventral fin as the test structure to implement an active vibration control system using piezoelectric actuators with co-located sensors. The Block 15 ventral fin was an ideal test structure to test the application of piezoelectric actuators and sensors due to its minimal effect on safety of flight in case of catastrophic failure. The original proposal was researched by Morgenstern and a preliminary analysis was completed using finite element model (FEM) analysis. Browning implemented Morgenstern's results and designed the piezoelectric actuators and co-located sensors and analyzed the effectiveness of single-input single-output (SISO) positive position feedback (PPF) controller in actual flight in the ACTIVE FIN project. This research attempts to improve the ACTIVE FIN design to overcome the shortcomings of the original design. In addition to testing the new design, advanced control algorithms are tested and readied for implementation for flight-testing. This research required experimental identification of the test structure using modal analysis with both accelerometers and a Laser Doppler Vibrometer. Once the structure was identified, the structure's frequency response functions (FRF) were determined experimentally. An Eigensystem Realization Algorithm was used to develop a mathematical model of the ventral fin. The control algorithms that were tested during this research included

the previously tested SISO PPF and, new in this research, multi-input multi-output (MIMO) control schemes to include multivariable PPF and MIMO linear quadratic Gaussian (LQG). Multiple modes of the structure were targeted for attenuation with each control algorithm. The laboratory results showed that reductions of 7.4 dB, 17.7 dB, 15.7 dB and 3.2 dB in modes one, two, three, and four respectively were achieved using the MIMO LQG controller while maintaining sufficient gain and phase margins. Further tests were accomplished to determine the robustness of the controllers. The MIMO LQG controller again performed the best by attenuating modes that were shifted in frequency by up to seven Hertz. The system is projected to be flown at the USAF Test Pilot School in the near future. To implement the system on the USAF TPS F-16, a custom power amplifier was also developed. During this research, laboratory testing was accomplished using the custom amplifier and non-optimal controllers and shown to be able to achieve the desired attenuation levels at the targeted modes.

Acknowledgements

I would like to first of all thank the members of the committee for providing guidance and the path forward to complete this thesis in conjunction with USAF Test Pilot School.

I would like to also acknowledge the countless hours Mr. Sean Miller has put into this project. The custom power supply required many innovations to allow its implementation on the F-16. I could not have safely and efficiently gone about this project without Sean's vast technical knowledge and skills.

I would like to thank the staff of USAF Test Pilot School for allowing me to continue with this project despite the many setbacks. Their patience and trust in my abilities were a constant encouragement throughout the duration of this project.

Tomoyuki D. Ono

Table of Contents

List of Figures

x

List of Tables

List of Symbols

List of Abbreviations

Application of Multi-Input Multi-Output Feedback Control for F-16 Ventral Fin Buffet Alleviation Using Piezoelectric Actuators

I. Introduction

The study of active control of structural vibrations has been a popular topic amongst the research community and varies in scope from actively controlling massive buildings during earthquakes [17] to suppressing vibration during solar array deployment in space [22]. Controlling vibration in aircraft structures is one of the many research areas that have been investigated. So far, most research in aircraft structures have been limited to theoretical and laboratory studies, but in 2009 the ACTIVE FIN research and flight test was conducted by Joseph Browning as an Air Force Institute of Technology (AFIT) and USAF Test Pilot School (TPS) joint project [8, 9]. This project implemented an active vibration control system using smart structures on an F-16D ventral fin and was flown in flight tests. Several high profile active control research using smart structures had been conducted to actively control the F/A-18 [33] and F-15 [19] vertical stabilizers but were limited to partial structures or scale models in wind-tunnels and never took flight.

The ACTIVE FIN project originated from a study that was conducted in 1997 by the Air Force of a F-16 ventral fin failure [35]. The ventral fin had a catastrophic failure in which more than half of the structure was ripped off. The pilot, however, did not notice the missing ventral fin until his post-flight inspections (Figure 1.1). The ACTIVE FIN flight test produced some promising results with some reductions in vibrations, but several unexpected shortcomings in the design prevented the project from reaching its full potential.

A study by Shawn Morgenstern at AFIT introduced the idea of using this structure as a testbed for active vibration control due to its minimal effects on flight in

Figure 1.1:   Ventral Fin Damage [29]

case of failure [29]. Morgenstern conducted a finite element model (FEM) analysis and developed a design for an active control system using piezoelectric actuators. During the same time, the Air Force Flight Test Center (AFFTC) conducted project HAVE PUFF, which used synthetic jet actuators to disrupt the buffet inducing flow around the ventral fin [30]. The test produced negligible vibration reduction but provided valuable flight data on the dynamics of the ventral fin.

In 2008, Browning conducted a study at AFIT to implement the active control systems using piezoelectric actuators on the same ventral fin used during the HAVE PUFF project [9]. Browning continued on to TPS to fly his system on the F-16D, achieving a significant milestone in the application of an active vibration control system in flight [8]. Figure 1.2 shows the ventral fin installed and being tested on an F-16D. Browning concentrated his research on single-input single-output (SISO) control algorithms. The two SISO algorithms studied were the positive position feedback (PPF), first introduced by Goh and Caughey [42], and the linear quadratic Gaussian control (LQG), which was developed in the 1960's.

Browning finished his research by analyzing the flight test results and developing recommendations to further improve the system. The next iteration in the short

Figure 1.2:   ACTIVE FIN Flight [9]

history of the ventral fin active vibration control was to take the recommendations from Browning and implement them for another round of flight tests.

1.1 Problem

The research problem in this thesis was to determine what design improvements over the ACTIVE FIN project were needed to successfully implement an effective active vibration control system using piezoelectric actuators and sensors and multi-input multi-output (MIMO) control algorithms for in flight application.

1.2 Scope

The research included physical improvements of the design by addition or exchange of components, but the majority of the time was to be spent on designing the MIMO control algorithms. The overall scope of the project was reduced when it was identified that the test item (the new ventral fin) was not the same one used in the ACTIVE FIN research. This required significant 'retesting' of the 'new' ventral fin to match flight data to the new configuration. As a result, this led to suboptimal controller designs and minimal testing with the control computer that will be used in flight. Although finding the optimum design for each control algorithm was desired, it was decided that developing a practical controller design process that can be implemented in the future would be sufficient for this research.

1.3 Approach/Methodology

Six distinct tasks were accomplished in support of the defined problem. A new ventral fin was obtained by TPS and was visually identified to be a different fin. The first task was to experimentally determine the identity of the fin. The second task was to investigate ACTIVE FIN's flight test results to determine the physical modifications necessary to meet the shortcomings experienced during that test. Once the decision was made, the third task was to decide on the actuator locations and install them. The fourth task was to determine a mathematical model of the fully instrumented fin for use in the controller design process. The fifth task was to develop a control algorithm design process and design the different controllers. Finally the entire system with the control algorithms were tested to determine the active control performance. The final task also included tests to determine if the performance can be achieved in adverse situations, such as a change in plant dynamics, similar to a flutter condition.

II. Literature Review

This chapter presents a study of topics relevant to this research. The history of the research is covered in more detail from the failure of the ventral fin to the most recent flight test of the active vibration control system. The section also covers recent research into power flow through piezoelectric actuators in vibration control applications. Finally a brief history and concept of MIMO control algorithms will be covered. This chapter provides the reader with a broad understanding of the background of this research and the reasons for approaching it the way it was.

2.1 Ventral Fin History

High performance aircraft such as those in the military have experienced the negative effects of structural vibrations up to a point where serious consequences have been encountered. Take for example the the F-15 which is a highly reliable aircraft but is still susceptible to the effects of buffeting causing secondary structural cracking [19, 27] and fatigue issues on the vertical tails. The F-15 program incurred costs by redesigning the aircraft several times in the 1980s. Another high profile aircraft that experienced problems with buffeting was the F/A-18. It was found that during a high angle of attack maneuver, the air flow was disturbed by the fuselage creating unsteady pressures hitting the vertical tails [39]. The concentration of energy in the low frequencies interacted with the vertical tails and excited the structural modes, which were in the same frequency range, resulting in buffeting. The damage caused by buffeting led the Navy to also invest in redesign of the structures, again increasing the cost of the overall program [33].

Although two major cases of primary aerodynamic structures were mentioned, the more common structural failures due to buffeting occurs on secondary structures such as antennas, panels, and fins. The F-16 carries two such fins towards the aft of the aircraft and was designed to stabilize the aircraft during high angle of attack maneuvers where the vertical tail could be masked by the fuselage. Early versions were susceptible to structural failures due to disturbed flow caused by engine inlet

spillage and a redesign of the fin was accomplished [29]. In the 1980's the USAF F-16 received a Low Altitude Navigation and Targeting Infrared for Night (LANTIRN) pod upgrade that placed a cylindrical sensor package on the front half of the bottom of the fuselage. The disturbance of airflow by the LANTIRN pod created an environment that made the ventral fin, located behind the pod to experience flutter and lead to complete structural failure (Figure 1.1). The solution to the failures were investigated by the Royal Netherlands Air Force and led to another redesign of the ventral fin by adding structural enhancements and stronger materials [41]. The ventral fins used on the active F-16's have been continuously modified with new materials technology and design processes [5].

2.2   *Active Vibration Control of the Ventral Fin*

Three major research projects have been conducted so far to develop an active vibration control system for the F-16 ventral fin. The ventral fin was chosen to be the ideal testbed for active vibration control in flight due to its failure posing "relatively little risk to the pilot or the aircraft" [29].

The first of these research was project HAVE PUFF conducted by USAF TPS at the AFFTC as part of the Active Load Control (ALC) program [30]. The test project was a study on the effectiveness of active flow control to reduce the vibrations of the fin. Phase one of the program was to test a modified LANTIRN pod that included six Dual Bimorph Synthetic Jet (DBSJ) actuators to actively change the flow over the ventral fins (Figure 2.1). The test project claimed the use of a Block 15 right ventral fin and instrumented it with accelerometers and strain gauges to measure the fin response during flight. The effectiveness of the active flow control system was described as follows in their final technical report:

> The DBSJs did not significantly affect the response variables. The effect of the DBSJs on strains (S1) or static pressures (P1) was insignificant across most of the flight envelope and the LANTIRN-ALC was determined to be ineffective when operating with external wing tanks [30].

6

Figure 2.1:   HAVE PUFF Test Flight [30]

Although the active control system was not successful in reducing the vibrations, the test program did yield valuable data on fin dynamics in flight. The main form of data obtained were the power spectral densities at the different sensors, which provided information on the structural modes of the fin in flight as well as energy concentrations of the buffeting. The ALC results showed that, although dependent on the sensor location, the largest concentrations of energy were seen in modes one and four followed by three and two.

The second research was conducted by Morgenstern at AFIT in which he introduced the use of smart materials as a candidate for active control actuators [29]. Morgenstern first developed an FEM model of the Block 15 ventral fin based off of a NASTRAN Block 40 model that was used during the investigation in 1997 [35]. The Block 40 model was altered slightly to better reflect the Block 15 configuration and fine tuned to match the modal frequencies as those found in the 1997 study. Morgenstern then analyzed the model and determined the critical modes of the fin to be the first, second, and fourth. Morgenstern finalized his research by proposing a piezoelectric actuator design and installation location from the FEM results. The piezoelectric actuators used in his modeling were of the piezoceramic composition in a macro-fiber composite (MFC) form. Morgenstern also conducted a comparison of

his FEM model with the ALC flight test data and noted discrepancies in the modal frequencies. These discrepancies were never fully investigated.

The third and final research prior to this paper was the study conducted by Joseph Browning at AFIT and subsequently flight tested as the ACTIVE FIN project [8,9] at USAF TPS. Browning conducted extensive research on methods to implement Morgenstern's proposed system. Browning's first order of business was to create the MFC actuators and co-located sensors. Smart-Material Corporation provided the required services to manufacture the MFC actuators in the desired configuration. The ACTIVE FIN project obtained the same ventral fin that was used in the ALC program for implementation of the system. Browning conducted a structural identification of the fin and found that the modal frequencies were similar to the ALC flight test results but different from Morgenstern's FEM analysis. The differences were not investigated any further and were accepted as inaccuracies in the FEM results. To ensure that the actuators would be effective in controlling the target modes, which Browning chose to be modes one and two, the principal strain directions were determined at those frequencies. He found the directions to match Morgenstern's analysis closely and decided to follow the installation configuration derived from the FEM analysis. With the actuators and sensors installed, Browning proceeded to determine the mathematical model of the instrumented ventral fin and test the SISO control algorithms. Laboratory tests showed promise with both the SISO PPF and SISO LQG controllers with attenuations of up to 20 dB in mode two. Flight test was limited to SISO PPF due to the lack of processing power of the control computer. The actuator power source was also limited to ± 425 volts, which took into account the -500 volt limit of the actuators and some safety margin. The final flight test results showed only a 4 dB reduction in mode two and none at mode one. The results were attributed to the control saturation seen due to the larger than expected vibrations. In addition there was a failure of one of the actuator amplifiers during the flight test which did not produce results showing the capabilities of the full control system. The test did,

however, produce flight data related to the MFC actuators and sensors which were valuable to this research.

2.3   Piezoelectric Power Requirements

Use of piezoelectric actuators in active control systems have many advantages such as weight and versatility. There are, however, drawbacks to it as well, one of them being power consumption. Several studies have been conducted to determine the power consumption of these actuators.

The first study was conducted by Matthew Brennan where he first created a mathematical model of the power usage of a piezoelectric actuator using its dielectric properties and dimensions in a structural vibration control application [7]. Brennan followed up with experiments to prove his theories. Piezoelectric actuators by nature act as capacitors in a circuitry and Brennan determined that the power requirements were independent of the structures they were attached to. This meant that the power requirements were solely dependent on the size and number of actuators and not how they are implemented on the structure.

Another study was conducted by Chandrasekaran and Lindner [11] where they analyzed power flow through piezoelectric actuators and determined that controlling the current flow was proportional to an acceleration feedback, the feedback setup for their experiment, rather than controlling voltage. This meant that even if the voltages are present, without sufficient current flow to match the power, the actuator will not be at the expected performance level.

For applications on an aircraft where amount of power available is limited, understanding and being able to predict the power usage of the system was critical to this research.

2.4   Feedback Control Algorithms for Vibration Reduction

Active control of structural vibration has been a popular topic and there have been numerous control methods that have been studied for this application. One of the critical components of an active control system that determines which control algorithm is best suited is the choice of feedback sensor. Acceleration feedback has been one of the most popular due to its simple implementation and ease of accurate measurement [14]. The F-18 vertical fin research used such acceleration feedback to study the effects of active control using piezoelectric actuators [31]. Velocity and position on the other hand were harder to measure accurately and were not prevalent until the development of strain sensors such as those used in this research.

In the late 1980's Goh and Caughey developed a structural vibration control algorithm based off of position measurements [18]. They developed the positive position feedback control algorithm and proved that it was far superior for application in structural vibration control because "conditional global stability conditions can be derived analytically and are easily satisfied" [18]. Up to that point, the best feedback method for structural vibration was considered to be co-located velocity feedback due to its unconditional stability, but in the absence of actuator dynamics. The position feedback allowed for stabilizing conditions despite actuator dynamics and was less prone to spillover effects. With the availability of piezoelectric strain sensors, PPF controllers for vibration control have gained popularity and can be found in many research studies. Multivariable PPF, where there is more than one actuator and one sensor, was the next step of research since Caughey and Goh. Fanson and Caughey continued to experiment with the PPF control and eventually applied it to multivariable applications [15]. Since the advent of PPF, there has been multiple research on the subject to include Kwak's study on real time tuning of MIMO PPF control [23] and application to systems with non-equal number of actuators versus target modes [24]. Further experimental results were published by Moheimani, which proved the effectiveness of multivariable PPF controller using co-located piezoelectric

sensors. In summary the benefits of the PPF controller is the ability to design the controller to effectively attenuate the target modes without destabilizing effects.

Another commonly occurring control algorithm in the research for vibration attenuation is the optimal control methods such as the linear quadratic regulator (LQR) in the F-18 research [31], H_2 methods used in the F-15 study [19] and H_∞ methods used in B-1B vibration suppression research [25]. Each method uses a different optimization algorithm (i.e. minimization of H_2 norm versus H_∞ norm) that achieves different objectives. These optimal control methods were plagued, however, with observation spillover that had destabilizing effects when dealing with high-order plant models [9], which Goh and Caughey's study of PPF controllers was one solution to. The preferred control method for MIMO systems is still the optimal control method, as seen in a study by Zhang. Using independent mode space control techniques to design the LQR, the method narrowed down the design parameters to modal states and control inputs, despite the number of actuators or sensors of the plant system [42].

One of the drawbacks to LQR is that it requires full-state information of the plant. When the number of sensors is limited, it is not possible to observe every state of the plant system. This limits the LQR controller to achieve the desired reductions only in the modes that the sensors can observe. The solution to this problem is to either reduce the plant model to only those states that are observable, which can introduce inaccuracies in the model due to missing dynamics, or add a Kalman filter, or linear quadratic estimator (LQE), to estimate the unobservable states. The combination of the LQR and the LQE is what is now known as the LQG and was selected as a controller to investigate in this research.

III. Methodology

This chapter covers the steps taken to accomplish the objectives of this research. The chapter includes the theoretical background of the methods used and how they were implemented. The first step of the research was to determine the identity of the new ventral fin using modal analysis. Once the structure was identified, placement of the actuators and sensors were investigated and the patches installed. Next, changes in system design based on the literature review and past research were implemented to improve the system. After the entire system was setup, a mathematical model of the new fin was derived and the control algorithms were developed. Finally, simulations and laboratory tests were conducted to determine the effectiveness of the system.

3.1   Ventral Fin Identification

This research began with the premise that an identical ventral fin used in the ACTIVE FIN research [9] would be available. When the previously used ventral fin was examined, it was noted that there were damages of unknown cause on the actuator patches that rendered them ineffective. It was not possible to remove the patches without damaging the fin, so a replacement ventral fin was ordered. When the replacement fin was received, however, there were clear visual differences that were of concern. This difference alone led to further analysis of the fin to identify whether similar installation of the piezoelectric actuator and sensors to the ACTIVE FIN research would be valid. The newly obtained fin was taken off a Block 15 F-16; however, it was discovered that not all Block 15 fins are identical. A Block 15 ventral fin was the fin that Morgenstern conducted his analysis [29] on and also the fin used in the ACL program and the ACTIVE FIN project. But, the visual cue that immediately led to the concern was the non-uniform surface of the new fin. Contrary to the fin used in the ACL and ACTIVE FIN, where the entire fin surface was aluminum, the rear ten-plus inches of the fin had different coloring than the rest of the aluminum surface and was clearly made of some type of polymer (Figure 3.1).
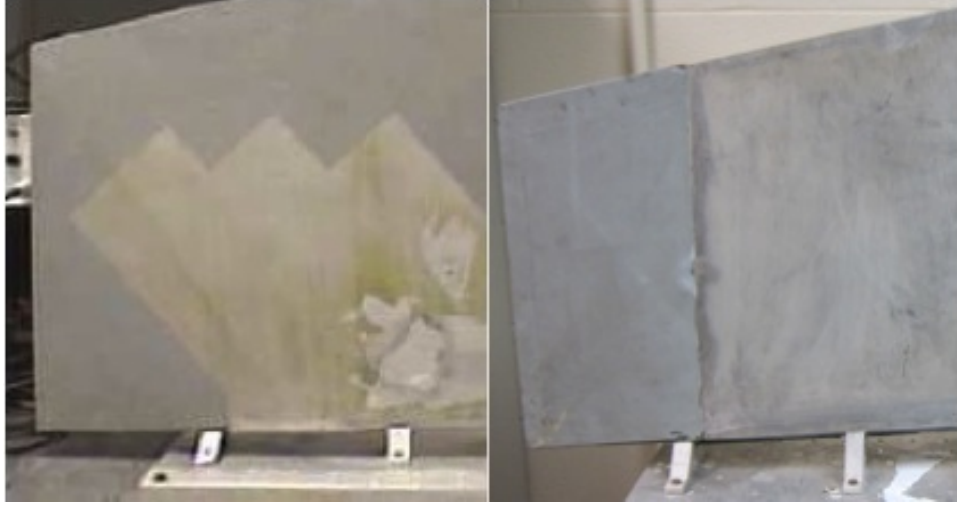
Figure 3.1:   ACTIVE FIN (left) vs. New Fin (right)

The difference in structural material can cause some differences in the dynamics of the fin and further analysis was required before proceeding with the installation of the MFC actuators and sensors. Investigation into the history of the fins did not produce any useful results so experimental identification of the fins were conducted. Modal analysis was used to determine whether the fins were truly different by comparing their natural frequencies and mode shapes. For a preliminary analysis, an impact hammer and an accelerometer were used to obtain modal frequency information from the new fin. A PCB Piezotronics, Inc. Impact Hammer Model 086C01 was used as the input force and a PCB Model 352C22 accelerometer was used to measure the structure's output in relation to the input force. The impact point of the hammer was kept constant at the top corner of the fin while the accelerometer was moved to several different locations on the fin (Figure 3.2). It was also possible, due to reciprocity, to move the impact point around and maintain the accelerometer location to obtain the same result [6].

Both the accelerometer and impact hammer were connected to a signal conditioner and fed into Data Physics Corporation's SigCalc 620 Spectrum Analyzer to produce frequency response functions (FRFs) relating the input (impact hammer) to the output (accelerometer) signal. Multiple locations for the accelerometer were used

13
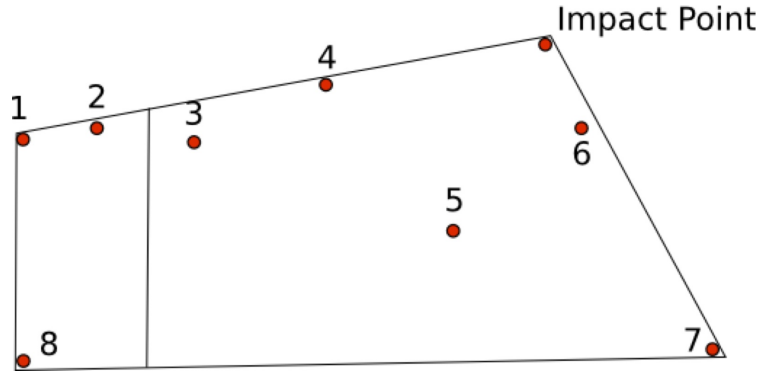
Figure 3.2:   Accelerometer and Impact Hammer Locations for Modal Analysis

to ensure that no modes were missed. Modes can be missing from FRFs if the impact point is at a node for that mode [6]. To ensure that each impact was acceptable, the spectral density after each impact was looked at to ensure enough energy was input for the frequency range of interest. The exceptions are at the anti-nodes where the coherence is known to be bad. The selection of the impact hammer tip and the impact itself affected the coherence. A Piezotornics, Inc. model 084B04 'Medium' hammer tip produced the necessary input to cover frequencies of interest. Another key item noted by a paper written by Avitabile on modal analysis, and used during the experiment for obtaining good measurements was the windowing. Avitabile suggests the use of windowing to minimize leakage issues, especially with lightly damped structures (Figure 3.3). A rectangular window was used on the hammer signal and an exponential window on the accelerometer signal.
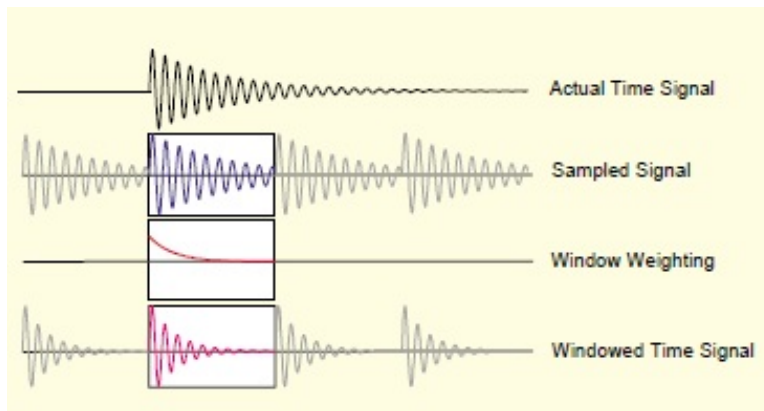
Figure 3.3:   Example of Exponential Windowing [6]

14

The results using the accelerometer and an impact hammer provided the natural frequencies of the new fin to compare with the ACTIVE FIN ventral fin (Figure 3.4).
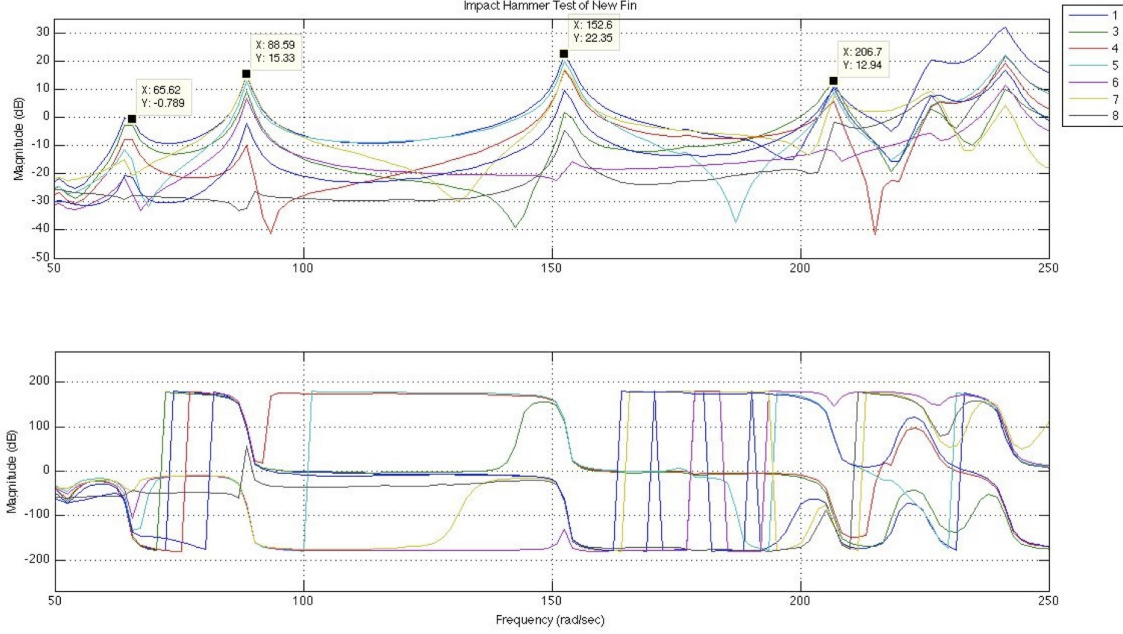
Figure 3.4:   Result of Accelerometer Modal Analysis

The first four natural frequencies of the new fin from the first modal analysis were located at 65.62, 88.59, 152.6, and 206.7 Hz. Keeping in mind that the way the fin is secured and where it is secured, the equipment used to gather the data and other minor structural anomalies, the modal frequencies can differ slightly between two identical structures. However, when compared to the modal frequencies obtained by Morgenstern for his original FEM analysis [29] and the frequencies determined by Browning on the actual ventral fin [9], this ventral fin matched more closely to Morgenstern's than Browning's (Table 3.1). The discrepancies in frequencies were noted by both Morgenstern and Browning when they were comparing the FEM model to the ACTIVE FIN fin, but was dismissed as an error in modeling, but with these results, that assumption was put in doubt.

15

Table 3.1:   Comparison of Modal Frequencies
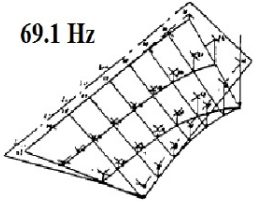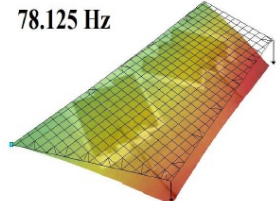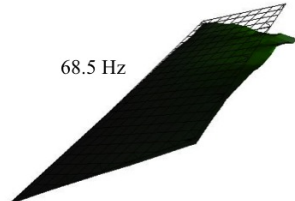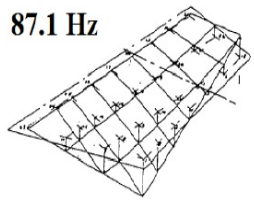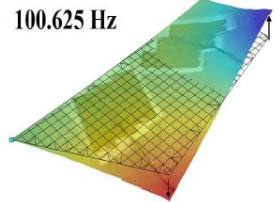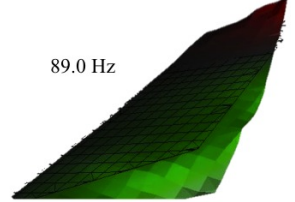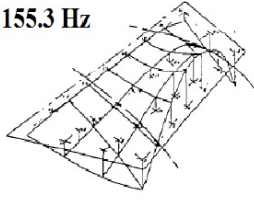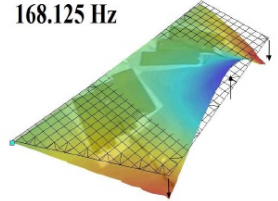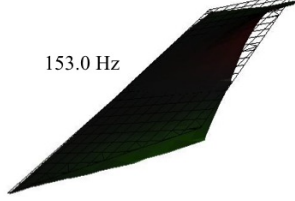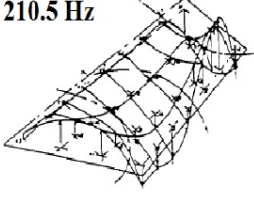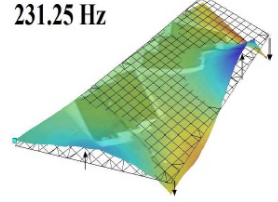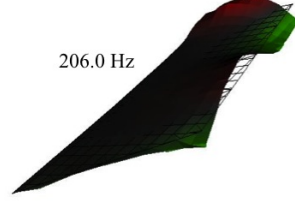
	Mode 1	Mode 2	Mode 3	Mode 4
Block 15 GVT [9]	69.1 Hz	87.1 Hz	155.3 Hz	210.5 Hz
ACTIVE FIN [29]	80.4 Hz	94.0 Hz	162.5 Hz	236.4 Hz
New Fin Accelerometer	65.6 Hz	88.59 Hz	152.6 Hz	206.7 Hz

From the comparison of the modal frequencies, preliminary conclusion was that the new fin and the Block 15 GVT fin that Morgenstern conducted his analysis on were the same and the ACTIVE FIN fin was a different fin.

Just comparing modal frequencies would not have been a complete comparison of the two fins. In fact, the measurements still resulted in differences but it was unclear as to the specifics without identifying detailed mode shapes. A scanning Laser Doppler Vibrometer (LDV) using PolyTec software version 8.6 by PolyTec Inc. was used to measure the frequency response of the fin and visually represent the modal shapes. The concept of gathering the frequency response is the same as the accelerometer test but used an LDV instead. A chirp signal was input to an APS Electro-Seis long stroke shaker, which was connected at the same location as the impact hammer impact point, to cover a wide range of frequencies. The LDV gathered velocity data at each point for the time period of the chirp signal which produces the same desired results as an impact hammer [6]. The advantage of using the shaker was the consistent input rather than individual human input. The PolyTec software analyzed and processed the measurements and produced the FRF of the magnitude and phase of the velocity measurements compared to the input signal. Since a velocity measurement is simply a derivative of position data or an integral of acceleration data, it did not change the measured modal frequencies. In addition to the modal frequency data, the software produced graphical representations of the mode shapes to allow comparison to the graphical models from Morgenstern's model and results from ACTIVE FIN.

When the mode shapes from the LDV results were visually compared to Morgenstern's and Browning's respective mode shape models, a major discrepancy was noted in the mode one shape where both the FEM model and the LDV results showed

Table 3.2:   Mode Shape Comparisons

Mode	Block 15 GVT [29]	ACTIVE FIN [9]	New Fin LDV
1st	69.1 Hz	78.125 Hz	68.5 Hz
2nd	87.1 Hz	100.625 Hz	89.0 Hz
3rd	155.3 Hz	168.125 Hz	153.0 Hz
4th	210.5 Hz	231.25 Hz	206.0 Hz

the fin displacement only in the aft end while the ACTIVE FIN fin showed a displacement of the entire fin. By comparing the mode shapes and the corresponding natural frequencies (Table 3.2), further verification was made that the ACTIVE FIN ventral fin was of a different model than the newly obtained fin or the fin analyzed by Morgenstern.

This result led to the requirement of analyzing the principal strain directions again due to the uncertainty that it will be the same as the FEM model. Installation of patches were also delayed until this information was obtained instead of merely installing the same configuration as in ACTIVE FIN.

3.2 Experimental Determination of Principal Strain Direction

According to Morgenstern and the HAVE PUFF test project, modes one, two, and four contributed significantly to the aeroelastic instability [29]. Browning decided to control modes one and two for the ACTIVE FIN research to simplify the required setup of the fin. For this research, and since the fin is different from ACTIVE FIN, the decision was made to target modes two and three, two modes that showed the highest magnitude peaks in relation to the other modes during both the impact hammer and LDV analysis. These modes were also chosen to measure the effectiveness of vibration reduction rather than the effectiveness to keep the fin intact (which were identified as modes 1, 2 and 4).

For mode two Morgenstern recommended placing the actuators on the front base of the fin where the maximum strain occurs for that mode. The suggested angle in Morgenstern's coordinate system [29] was 15.0 degrees (Figure 3.5). For mode three the suggested location was at the rear of the fin (Figure 3.6) at an angle of 110 degrees and in addition a second layer with fiber direction of 20 deg. Only the 110-degree direction was considered keeping in mind that the single fiber direction may not be as effective.
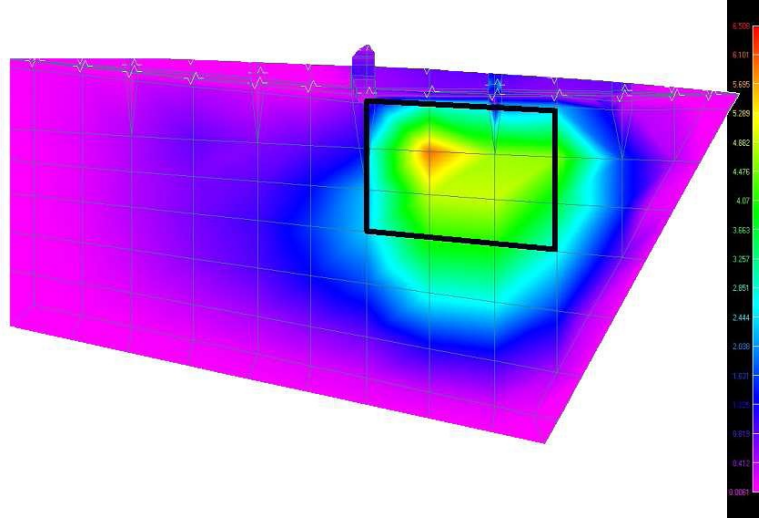
Figure 3.5:   Mode 2 Strain Energy Plot and Suggested Patch Location [29]
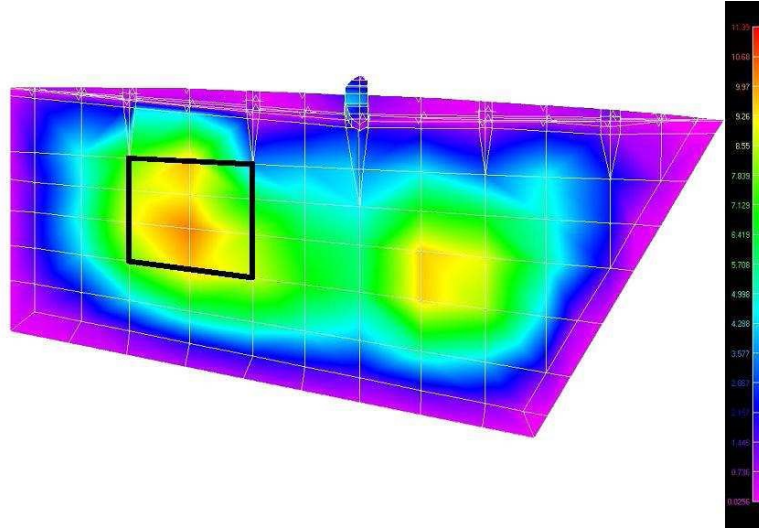
Figure 3.6:   Mode 3 Strain Energy Plot and Suggested Patch Location [29]

For the highest probability of success, the piezoelectric actuator and sensor fibers must be aligned with the principal strain vectors of the mode of interest [9]. Morgenstern's suggested fiber directions also corresponded to the principal strain vectors of the fin. To verify that the directions were valid for this fin, the LDV was used again. This time around, the points scanned were concentrated to the regions of the fin where the patches would be placed to control modes two and three. An automated impact hammer was obtained and used instead of the electromagnetic

shaker due to the suspicion that the shaker may have been adding its own dynamics to the structure affecting the fin's characteristic [6]. The use of the impact hammer as described before, should provide the same information as the shaker but with minimal external dynamics.

Experimental determination of principal strains required the use of multiple-element strain gages. In most cases, and certainly for the new ventral fin, the strain directions are not known and require the use of at least three strain gauges. Dally proved that three gauges in three different directions was sufficient to determine the principal strains of a surface, thus the use of a rectangular rosette (Figure 3.7) is a typical practice when determining the stress or strain fields [13].
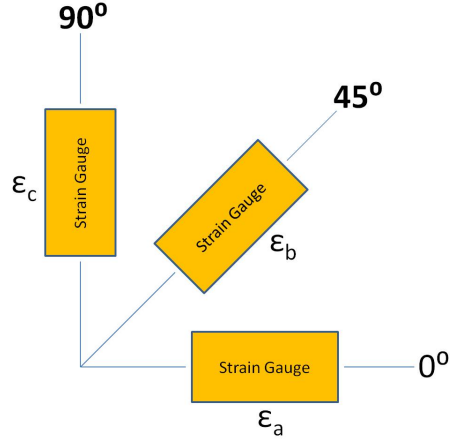
Figure 3.7:   Typical Rectangular Strain Gauge Rosette

The three-element rectangular rosette uses gauges that are placed at 0, 45, and 90 degree positions as seen in Figure 3.7 and the strain components (ϵ_a, ϵ_b, ϵ_c) corresponding to:

$$\epsilon_a = \epsilon_{xx}, \quad \epsilon_b = \tfrac{1}{2}(\epsilon_A + \epsilon_{xx} + \gamma_{xy}), \quad \epsilon_c = \epsilon_{yy}$$
$$\gamma_{xy} = 2\epsilon_b - \epsilon_a - \epsilon_c$$

(3.1)

By measuring the strains ϵ_a, ϵ_b, and ϵ_c, the principal strains, ϵ_1 and ϵ_2 can be determined by

$$\epsilon_1 = \frac{1}{2}(\epsilon_a + \epsilon_c) + \frac{1}{2}\sqrt{(\epsilon_a - \epsilon_c)^2 + (2\epsilon_b - \epsilon_a - \epsilon_c)^2} \tag{3.2}$$

$$\epsilon_2 = \frac{1}{2}(\epsilon_a + \epsilon_c) - \frac{1}{2}\sqrt{(\epsilon_a - \epsilon_c)^2 + (2\epsilon_b - \epsilon_a - \epsilon_c)^2} \tag{3.3}$$

and the principal angle ϕ with:

$$\tan 2\phi = \frac{2\epsilon_b - \epsilon_a - \epsilon_c}{\epsilon_a - \epsilon_c} \tag{3.4}$$

As explained by Browning, the use of actual strain gauges was impractical when trying to determine principal strain directions of an entire surface due to strict requirements to installation accuracy and the intensive installation and removal process [9]. Browning, through his analysis verified that the use of an LDV was a good alternative to determining principal strain directions. His results although not exact, produced principal strain directions similar to those of the FEM results previously conducted by Morgenstern [29]. The LDV measured velocity of the vibrating surface at different points and covered a wide range of frequencies. By determining the modal frequencies and taking the velocity data at those frequencies, the curvature of the surface was calculated and the strain directions were obtained.

The strain-curvature relationship holds when displacement is integrated rather than velocity. However, since the velocity data collected is frequency specific (modal frequencies), the only difference between the second derivative of the displacement and second derivative of the velocity is $j\omega$, where j is the $\sqrt{(-1)}$ and ω is the frequency. The end result is a scalar difference from actual curvature (or strain).

To obtain the curvature, the measured velocity values were differentiated spatially twice. Since the measured value is of discrete points, a central difference method

was used to obtain the derivative at the point. Consider a matrix of scanned points in Figure 3.8. By dividing the difference in displacement of the two adjacent points
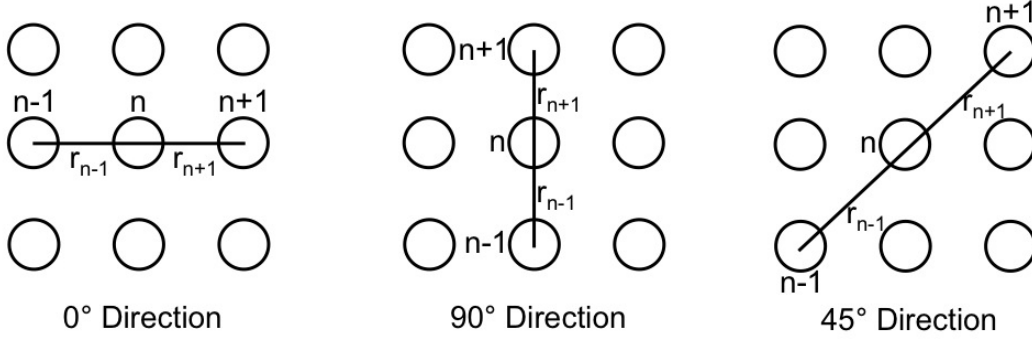
Figure 3.8:   Central difference method

from the difference in the magnitude of the same two points, an approximation of the derivative of the center point can be determined. The first derivative (Equation 3.5) corresponds to the slope and the second derivative (Equation 3.6) to the curvature

$$\left(\frac{dv}{dr}\right)_n = \frac{v_{n+1} - v_{n-1}}{r_{n+1} - r_{n-1}} \tag{3.5}$$

$$\left(\frac{d^2v}{dr^2}\right)_n = \frac{\frac{dv}{dr}_{n+1} - \frac{dv}{dr}_{n-1}}{r_{n+1} - r_{n-1}} \tag{3.6}$$

where v_n was the velocity magnitude measured by the LDV at point n and r_n was the length between the point of interest and the center point.

The validity of this method was researched and confirmed by Schussler [37] where he compared the results from the laser vibrometer to a finite element model. Schussler showed that the strain values determined through vibrometer measurements were in high agreement with the finite element model at all tested modes.

The scanned area for strain determination was concentrated to those actuator locations that targeted modes two and three. Figure 3.9 shows the actual scan area.

22
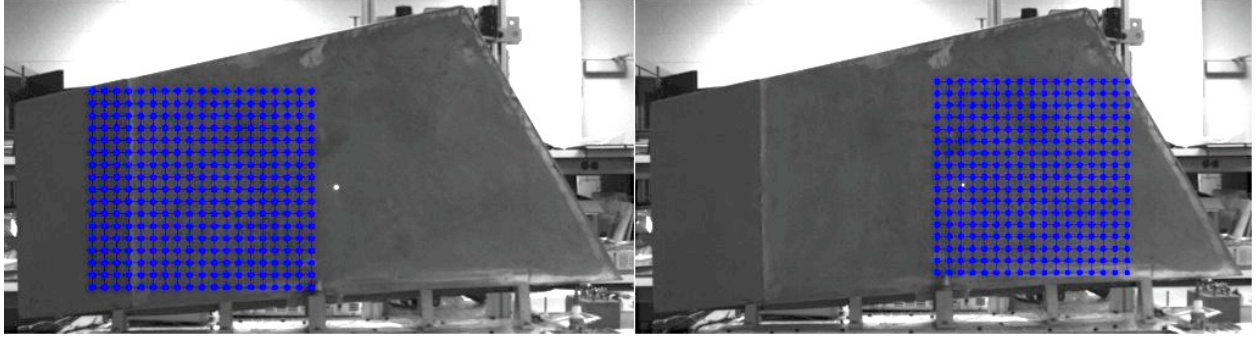
Figure 3.9:   Scan Points for Strain Direction Determination

The principal strain directions and their relative magnitudes were calculated taking the resulting second derivatives at the three rosette angles and applying them to Equations 3.2 through 3.4. An arbitrary value of ten degrees was chosen as the acceptable difference between the LDV results and Morgenstern's model to assume the fin was the same model analyzed in his research.

Implementation of the above method was accomplished using MATLAB® and the resulting plots of modes two and three scan area are shown in Figure 3.10. The figure shows the LDV determined principal angles and the points where the angles matched within 10 degrees of Morgenstern's proposed angles. Each scan area was specifically measured at the individual modes because of Morgenstern's proposed patch locations for those modes.
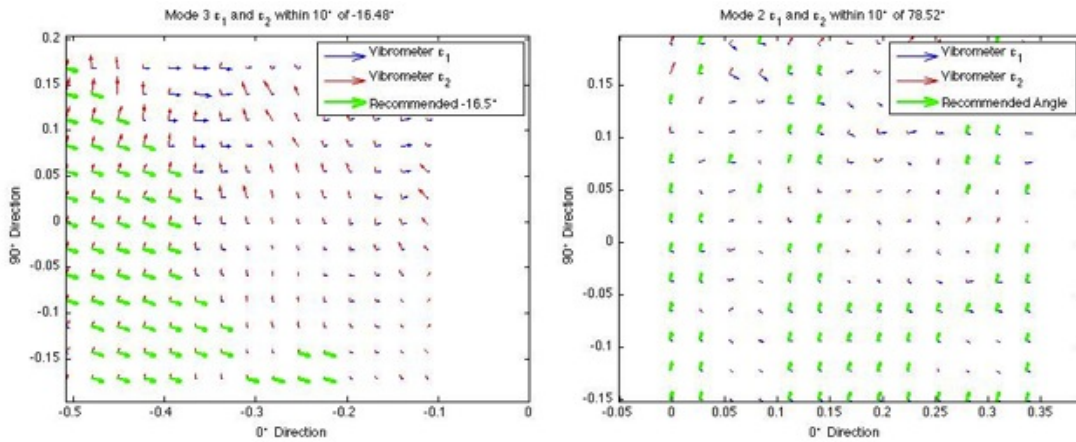
Figure 3.10:   Mode 2 (left) and Mode 3 (right) Principal Strains Results

The result of the scans were not of the best quality due to the noise that was seen in the measurements but it was enough to determine that the principal angles closely matched those of Morgenstern's FEM analysis and a decision was made to proceed with installing the patches at the proposed angles. An additional decision was made on how to line the patches in each section from the LDV results. Looking at the mode three plot, it was seen that the principal angles that matched the FEM model was vertically stacked at the left edge of the scan area. This led to the decision to spread the patches to cover as much vertical space rather than horizontal. Mode two on the other hand showed that matching principal angles were equally spread. The mode two patches were installed to cover the entire area more completely, which ended up being lined horizontally (Figure 3.11). These patch locations corresponded very well with Morgenstern's proposed locations seen in Figures 3.5 and 3.6.

Figure 3.11:   Final Patch Locations

An opportunity came up to attempt another LDV scan after the patches were installed with an addition of a reflective sheet that could be adhered to the fin surface. The sheet significantly increased the reflected LDV signal and produced a much cleaner result. The new scan pattern is shown in Figure 3.12 and the principle strain direction results in Figure 3.13.
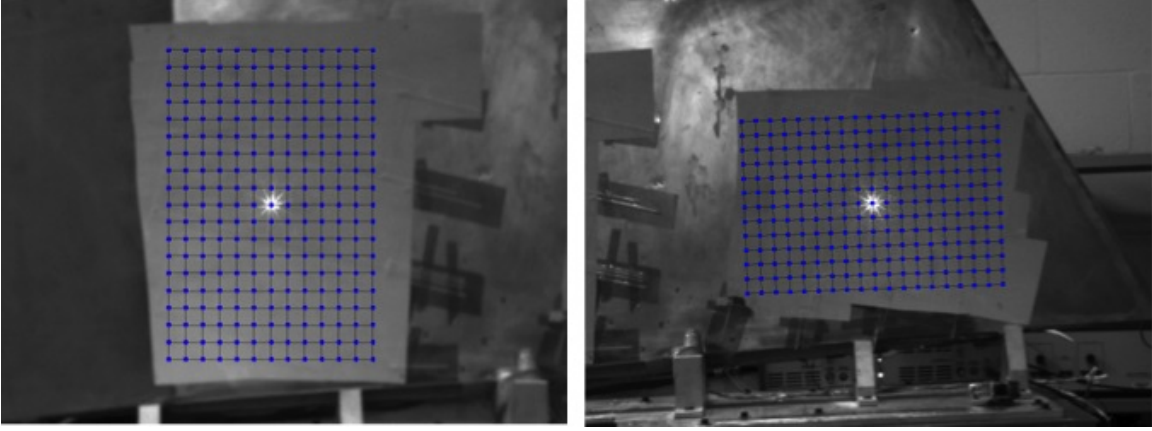
Figure 3.12:   Post Patch Mode 2 (right) and Mode 3 (left) LDV Scan Areas
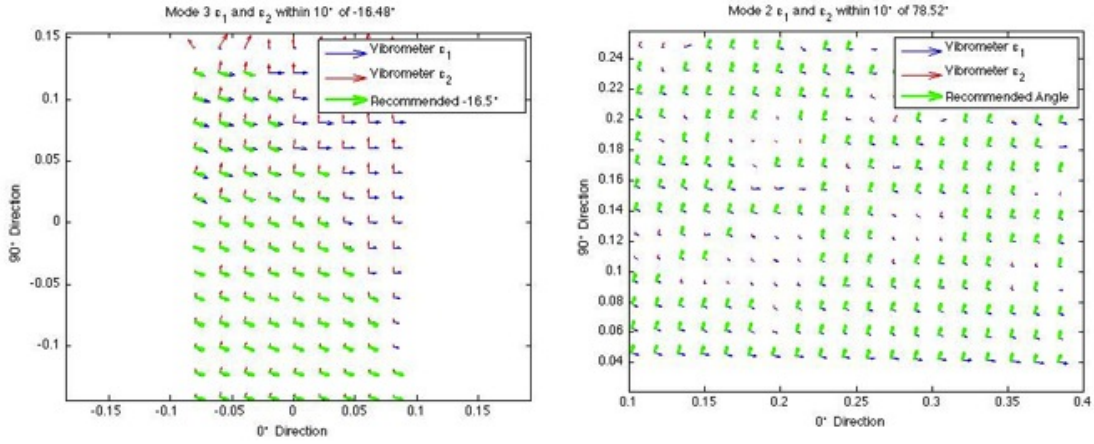
Figure 3.13:   Post Patch Mode 2 (right) and Mode 3 (left) Principle Strains Results

3.3   *Actuator and Sensor Selection*

The MFC actuator and sensor patches used in this research were identical to those custom-built for the ACTIVE FIN. There were two types of patches manufactured by Smart Material Corporation: an actuator only patch and an actuator with collocated sensor patch (Figure 3.14).

Both designs are 12 by 4 inches in area with the actuator only patch covering the entire surface while the sensor patch had a smaller actuator section to accommodate the thin strip of the sensor.
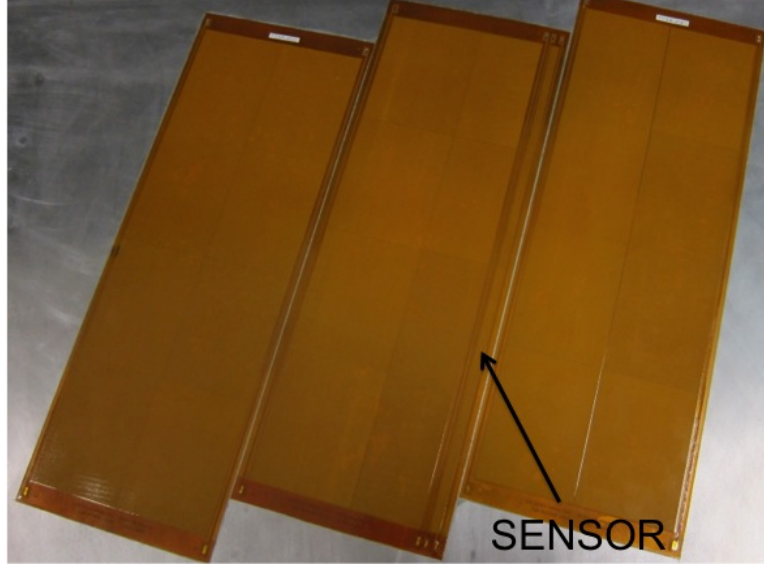
Figure 3.14:   Actuator (left and right) and Actuator-Sensor (center) Patches

3.4   Actuator Modification

Increasing the control authority was one of the primary requirements to improve upon the ACTIVE FIN setup as seen from the control saturations during flight. Two changes in the setup were used to achieve the higher control authority. First was to double the number of MFC actuators. The total strain can be increased by layering multiple actuators on top of each other. Research by Luo et al [26] has shown mathematically that the raw force and moment produced by layering increases linearly with the number of layers. During his experimental analysis, Luo was able to show that depending on the targeted mode, the effectiveness of layering the actuators can plateau as the number of layers increase. For this research, the number of layers was set to two to take advantage of the increase in control power from layering while limiting the cost.

The second control modification was accomplished by adding an offset to the signal going to the actuators. When the inboard and outboard actuators were operated using inverse signals as it was in ACTIVE FIN, the voltage range was limited to 1000 volts alternating current (AC) peak to peak. This was due to the fact that the actuators were only limited to -500 volts, which led to limiting the positive range

to +500 volts despite the +1500-volt design limit. Adding an offset direct current (DC) signal would allow for increase in range in both the positive and negative side. For example, a 500 volt DC offset will allow a signal of up to 1000 volts in either direction. Figure 3.15 shows an example of this concept. This offset capability was added to the system design through software on the control computer.
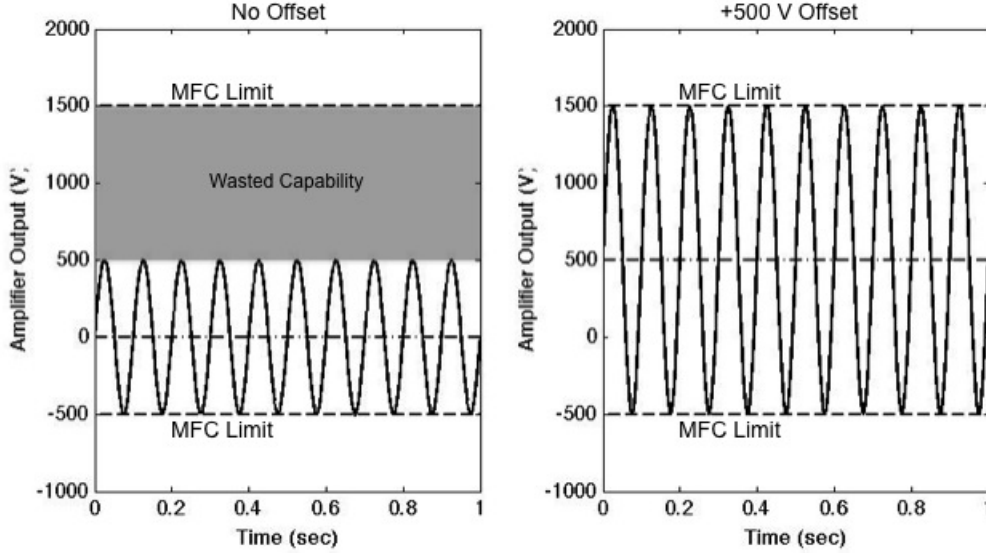
Figure 3.15:   Example of Offsetting Actuator Signal

3.5   Patch Installation

The piezoelectric patches were installed on the fin by following methods conducted by Browning [9]. The fin surface was first cleaned thoroughly using acetone and isopropyl alcohol. The fin locations were verified and the surrounding areas taped to ensure a clean surface after the installation was complete. Once the locations were marked, the Loctite® M-121HP Hysol epoxy was used as the bonding agent. A thin film of the epoxy was applied to both the fin and the patches and air bubbles removed for maximum area coverage. Once the air bubbles were removed, a layer of nylon release peel ply was laid on top of the patches to capture excess epoxy, then a layer of high-fill non-woven polyester breather and bleeder material was laid to allow even suction of air during the vacuum bagging process. Finally, sealant tape was

27
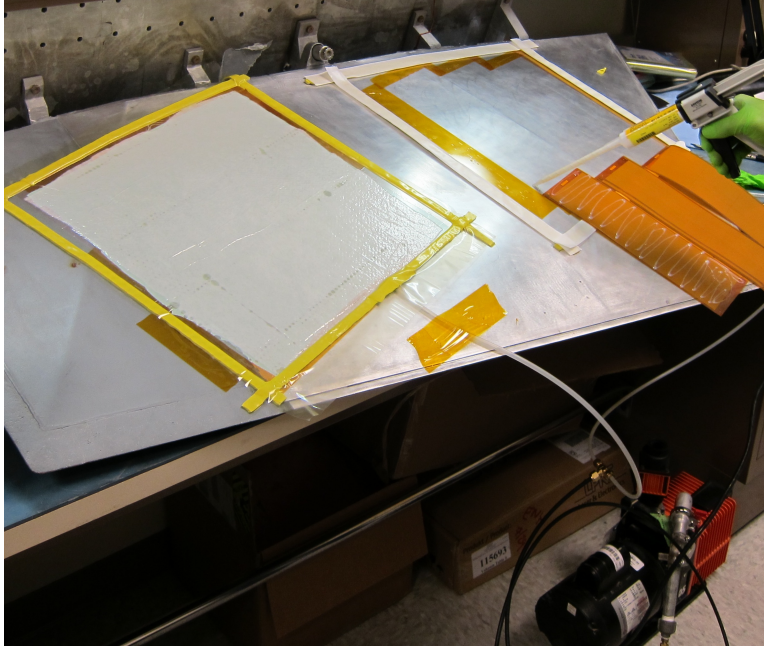
Figure 3.16:   Vacuum Bagging Process

laid around the patched area and a nylon bagging film was placed on top to cover
the entire patched area. A 2.5-horsepower vacuum pump was connected to the setup
and vacuum was maintained for about 24 hours to allow the epoxy to fully cure.
Figure 3.16 shows the vacuum bagging setup used during this research.

3.6   Power Requirements

Before determining the controller design, the power required by the feedback
system needed to be determined. Since the system will be on a fighter jet with limited
power availability, a maximum input voltage to the actuators was set to stay within
the aircraft power limit. Piezoelectric actuator power usage was investigated and
proven through experiment by Brennan [7] that the power requirements of a surface-
bonded piezo actuator was independent of the dynamics of the structure and the
actuator. This simplified the power usage equation to the generally accepted power

(P) as a function of frequency (ω), voltage (V), and capacitance (C) in equation 3.7.

$$P = \frac{\omega C V^2}{2} \tag{3.7}$$

The total capacitance for the 24 patches was the sum of the capacitance of each actuator. Capacitance of each actuator was experimentally determined to be related to voltage and an empirical solution for the actual capacitance was proposed by Brennan to be:

$$C_{\text{actual}} = C_0 + \frac{\partial C}{\partial V} V(\omega). \tag{3.8}$$

For this research the capacitance, C_0, of three patches was measured to be 281 nF. The partial derivative, $\partial C / \partial V$, was determined experimentally by measuring the current required by the patches at two voltages using a constant frequency sine wave input. The result showed that at 250 Hz, $\partial C / \partial V = 1.72$ nF/V. The final equation used to predict the maximum expected power requirement is shown in equation 3.9.

$$P_{\text{max}} = \frac{1}{2} \omega_{\text{max}} V_{\text{max}}^2 \sum_{i=1}^{n} C_i. \tag{3.9}$$

Since the target modes of the controller was at maximum 215 Hz, a value of 250 Hz was used for the input frequency, 1000 volts AC (from Section 3.4) for the input magnitude, and the previously defined C_0 and $\partial C / \partial V$ were used in equation 3.9. This resulted in a maximum power requirement of about 4600 Watts. From discussions with experts of the F-16, this amount of power was not available at any of the power sources. A decision was made to limit the maximum voltage of input at 700 volts AC, which resulted in a maximum power of about 1870 watts. This value was more acceptable to the available power sources from the aircraft.
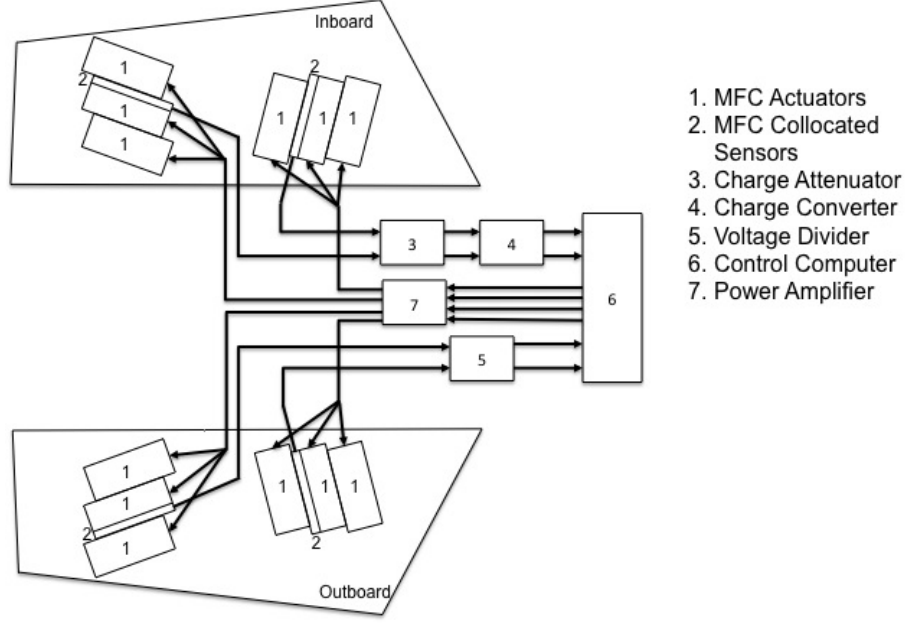
Figure 3.17:   System Configuration for Vibration Control

3.7   Control System Design

The whole system design developed by Browning was re-evaluated based off of the study conducted by Shankar [38] to pinpoint areas of possible improvement. Shankar's study proposed a system setup that ensured all the signals were properly fed through with minimal noise and adverse effects. First the piezoelectric sensors are connected to a signal conditioning setup consisting of a charge attenuator and charge converters. The signal conditioners then feed the measurements to the control computer and a control signal is produced. The control signal is fed through a power amplifier and then finally to the piezoelectric actuator patches. Figure 3.17 is a diagram of the entire setup and following are detailed descriptions of the each part.

MFC Actuators (1). The MFC actuators act as the feedback control input to the fin. The mechanical response to the electrical signal from the controller in this case is strain. As mentioned earlier, the two sections, front and rear, target modes two and three respectively. Each section had six total actuators, three side-by-side in two layers. 24 patches were used in total for four sections.

MFC Sensors (2). The MFC sensors measure the response of the fin due to outside disturbances. The strain measured is converted to electrical signal and is used for feedback control. One signal from the inboard front section and one signal from the inboard aft section is used for feedback. The sensors on the other side (outboard) were reserved for backup purposes. The sensor-actuator patch mentioned in Section 3.3 was placed in each section as the center bottom layer patch. This setup realized the co-located sensor system.

Charge Attenuator (3) and Charge Converter (4). The MFC sensor produces charge as well as voltage directly proportional to the sensed strain. In contrast to ACTIVE FIN, the inboard sensors were connected to a charge converter to measure charge produced instead of voltage. This decision was made due to the high impedance output of the MFC sensors. High impedance signals can be a cause of signal inaccuracies when it travels long distances through wires. In addition most measuring devices requires low input impedances from sensors [40]. Use of a charge mode amplifier, whose gain is independent of input capacitance, was also added to ensure that the signal sensitivity would not be affected by cable length or type, allowing this setup to be more flexible for installation [4]. An Endevco 2771C-01 was used for the inboard forward and aft sensors (Figure 3.18) as the charge mode amplifier. The 2771C-01 has fixed gain of 0.1 mV/pC and a peak-to-peak output of 10 volts [3]. The direct sensor output and the charge amplifier output was compared by inputting a known signal level and was determined that a relationship of 1:1.4 volts existed. This led to the assumption that if ACTIVE FIN's direct sensor output showed 120 volts peak output during flight, the charge going into the amplifier had to be reduced to meet the charge converter's operating range. A charge attenuator was added between the sensor and the converter to bring down the charge to the converter's operational range of ±5 volts. A Kistler Type 5361A 100:1 Charge Attenuator (later analysis resulted in 20:1) was proposed (Figure 3.18) for flight but omitted in the laboratory due to lower than flight excitation signals used. A method of exciting the fin at the levels seen in flight test was not available.

31

Figure 3.18: Endevco 2771C-01 Charge Converter [3] (left) and Kistler Type 5361A Charge Attenuator [1] (right)

Voltage Divider (5). Custom built voltage dividers were added to the outboard sensors. The outboard sensors were used for backup purposes in case the inboard sensor setup failed. The direct voltage measurement is not ideal for high impedance sensors but since this setup was used during ACTIVE FIN and would provide signals to compare directly to its results, it was repeated in this research. The voltage divider gain was set to 60:1 to meet the control computer's analog-to-digital converter input range of 5-volts peak-to-peak. A 2:1 voltage divider was also placed in line with the charge converter to change the 10-volts peak-to-peak signal into 5-volts peak-to-peak signal.

Control Computer (6). For this research a dSpace Inc. MicroAutoBox II (MABXII) Model 1501 (Figure 3.19) was used as the digital controller of choice to house the feedback control algorithm. The MicroAutoBox II was chosen for its high power processor and ease of programming using MathWorks SIMULINK® software. The unit communicates with a host computer through Ethernet but is capable of running autonomously. The analog-to-digital converter has a 10 kHz cutoff which acted as a low-pass filter, which is always recommended for signal processing. This natural cutoff restricted the control algorithms to be simple enough to enable the MicroAutoBox II to run at 20 kHz sample frequency or higher to meet the Nyquist frequency requirement. A dSpace DS1103 was used during laboratory experiments.

Power Amplifier (7). A power amplifier was required to drive the actuators. For this research a Trek, Inc. Model PZD 700 Dual Channel Amplifier was used while the flight test amplifier was being built. The Trek amplifier was capable of amplifying

Figure 3.19:   dSpace MicroAutoBox II Digital Controller [2]

signals to 700 volts at 200:1 gain, which was more than enough for lab testing. The amplifier designed for the flight test was an AFIT custom-built Class-D switching amplifier. The amplifier was designed to convert a unipolar 0 to 5-volt control signal from the MicroAutoBox II to signals ranging from -500 to +1000 volts. Limited testing was accomplished with the custom built amplifier to ensure the design was at least useable in the flight application.

3.8   Plant Transfer Function Development

Although it is possible to develop feedback control algorithms without a mathematical model of the plant, developing one allowed for computer simulations of the control system as well as development of advanced control algorithms that require a plant model. As practiced by Browning [9] the plant model was defined as everything after its digital-to-analog converter (DAC), to right before its analog-to-digital (ADC) converter. This allowed the controller to be separated from the plant and also simplified the whole system (without the digital controller) into one model. Another reason for this was to take out any digitization effects of the ADC and DAC, making it possible to work in the continuous domain all the way until implementation to the digital controller. The model for this research contained the power amplifier, MFC actuator, the ventral fin, MFC sensors, and signal conditioning components. (Figure 3.20).
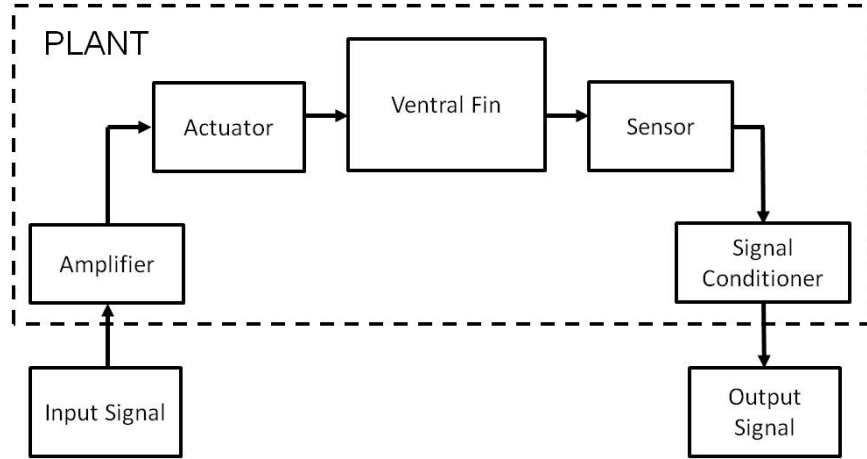
Figure 3.20:   Plant Model Diagram

Two sets of FRFs were collected for this research. The first set treated the front inboard and outboard actuators as one and the aft inboard and outboard actuators as one. By inverting the outboard actuator signal, the inboard and outboard actuators worked together to bend the fin in the same direction. If the outboard actuator compressed, the inboard actuator expanded (Figure 3.21). The two inboard sensors were used as output signal sources leading to four FRFs to characterize the two-input two-output plant. The second set treated all the actuators independently but with the same sensors. This four-input two-output plant required a set of eight FRF's to characterize. The SigCalc 620 was used to collect the FRF data. Each FRF,
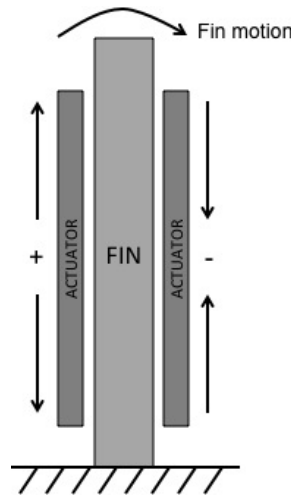
Figure 3.21:   Example of Inverted Signal

34

from one actuator to one sensor, was developed by actuating the one actuator with a periodic chirp signal and collecting the sensor measurement. The SigCalc 620 software calculated the same number of FRF's for each actuator as the number of sensors. The process was repeated for each input to collect all the input-output relationships. For the two-input two-output configuration, the front actuator signal set was input one (u_1) and the aft actuator signal set was input two (u_2). The front sensor signal was output one (y_1) and the aft sensor signal was output two (y_2). Equation 3.10 is the transfer function representation of the two-input two-output plant, a matrix of four transfer functions.

$$H(j\omega) = \begin{bmatrix} \frac{Y_1(j\omega)}{U_1(j\omega)} & \frac{Y_1(j\omega)}{U_2(j\omega)} \\ \frac{Y_2(j\omega)}{U_1(j\omega)} & \frac{Y_2(j\omega)}{U_2(j\omega)} \end{bmatrix} \tag{3.10}$$

For the four-input two-output configuration, the front inboard actuator signal was input one (u_1), the aft inboard actuator signal was input two (u_2), the front outboard actuator signal was input three (u_3), and the aft outboard actuator signal was input four (u_4). The same outputs y_1 and y_2 were used. Equation 3.11 is the transfer function representation of the four-input two-ouput plant model.

$$H(j\omega) = \begin{bmatrix} \frac{Y_1(j\omega)}{U_1(j\omega)} & \frac{Y_1(j\omega)}{U_2(j\omega)} & \frac{Y_1(j\omega)}{U_3(j\omega)} & \frac{Y_1(j\omega)}{U_4(j\omega)} \\ \frac{Y_2(j\omega)}{U_1(j\omega)} & \frac{Y_2(j\omega)}{U_2(j\omega)} & \frac{Y_2(j\omega)}{U_3(j\omega)} & \frac{Y_2(j\omega)}{U_4(j\omega)} \end{bmatrix} \tag{3.11}$$

To ensure enough frequency resolution and adequate coverage of all the modes, the SigCalc settings in Table 3.3 were used. The frequency span was set high enough to characterize the plant beyond the highest target frequency to allow observation of the controller effects on higher modes. The number of lines equated to frequency resolution. An averaging of 25% was used to reduce the errors caused by noise but still maintain accuracy. For the laboratory Trek amplifier, a 100 millivolt input signal equated to a 20-volt output and was sufficient to excite the structure and produce strong enough sensor signals.

Table 3.3:   Plant Characterization SigCalc Setup

Parameter	Setting
F Span	2000 Hz
Lines	6400
Overlap	25% Hann
Avg	10 Stable
Trig	Free Run
Waveform	Chirp
Level	100 mV
Freq 1	0.01 Hz
Freq 2	2000 Hz
Width	100%

To develop a mathematical model of the plant from the FRF data, the eigensystem realization algorithm (ERA) developed by Juang and Pappa [21] was used. The details of the algorithm is omitted here and can be found in the aforementioned reference. The ERA Toolbox developed by Cobb [12] for use with MATLAB® was used to implement the ERA and generate a MIMO state space model from the FRFs. The state space model took the well accepted form of:

$$\dot{x} = \mathbf{A}x + \mathbf{B}u$$
$$y = \mathbf{C}x + \mathbf{D}u$$

(3.12)

where x is the plant state vector, $\mathbf{A}$ is the state matrix in diagonal form, $\mathbf{B}$ is the input matrix, $\mathbf{C}$ is the sensor matrix, $\mathbf{D}$ was the feedthrough matrix, u is the actuator or input vector, and y is the sensor or measurement vector. The experimental FRF data allowed the ERA code to fit a stable sixty-state MIMO continuous state-space model. This resulted in a 60 by 60 state matrix ($\mathbf{A}$), 60 by 2 input matrix ($\mathbf{B}$), 2 by 60 output matrix ($\mathbf{C}$) and a 2 by 2 feedthrough matrix ($\mathbf{D}$) for the two-input two-output model. An eighty-state stable model was possible for the four-input two-output model resulting in a 80 by 80 $\mathbf{A}$, 80 by 4 $\mathbf{B}$, 2 by 80 $\mathbf{C}$ and a 2 by 4 $\mathbf{D}$ matrix for the four-input two-output model. Sixty states still accurately fit all modes in the FRF and was more than enough to meet the needs of this research.

36

Table 3.4:   Tested Controller Configurations

Plant Configuration	Controller	Number of Modes
2-Input-2-Output	SISO PPF	2 and 4
	Multivariable PPF	2
	MIMO LQG	2 and 4
4-Input-2-Output	MIMO LQG	2 and 4

3.9   Control Algorithm Development

Control algorithms were developed using MATLAB®, simulated on SIMULINK® and finally run on a dSpace DS1103 digital controller in the laboratory to assess actual performance. Three different types of control algorithms were developed for this research. First was the SISO PPF since the ACTIVE FIN project used this algorithm as its primary controller. Second was the multivariable PPF and the third was the MIMO LQG. For each control algorithm, two sets were tested, one targeting only modes two and three (the design actuator placement), and a second targeting modes one through four. Table 3.4 shows the different configurations the control algorithms developed. Each algorithm required a trial and error approach with the design parameters. In MATLAB®, each controller candidate was added to the plant model and the Bode plot of the new system was compared to the plant only Bode plot. The attenuations were calculated by taking the difference in magnitude at each modal frequency. The minimum attenuation desired was chosen to be 6 dB to ensure the attenuation would not be masked by random noise. Next the margins were calculated in MATLAB® as will be discussed in Section 3.10. The best combinations of design parameters were kept and continued with the SIMULINK simulations and eventually with the actual ventral fin.

3.9.1   SISO PPF.   For the SISO PPF, the forward and aft actuator-sensor pairs were separated so that the front actuator pair and the front sensor was a system, and the aft actuator pair and aft sensor was another system. The front signal was only fed back to the front actuator while the aft signal was only fed back to the aft actuator. The front system was used to target mode two (two and four for four-mode)

37

and the aft system targeted mode three (one and three for four-mode). The SISO PPF algorithm did not take into account the interactions between the front and aft systems other than to ensure the entire system was stable and produced sufficient stability margins. The use of co-located sensors made this a possibility.

For the two-mode configuration, each system had one second-order PPF transfer function targeting one mode. Equation 3.13, a PPF filter, was used as the controller equation for a single mode.

$$G_{ci}(s) = -g_{ci} \left(\frac{\omega_{ci}^2}{s^2 + 2\zeta_{ci}\omega_{ci}s + \omega_{ci}^2} \right) \tag{3.13}$$

$G_{ci}(s)$ is the controller equation for the i-th system. The three parameters control gain (g_{ci}), control frequency (ω_{ci}), and control damping ratio (ζ_{ci}) were the design parameters and were adjusted to determine the best control. The control frequency was matched to the measured frequency of the targeted mode. This left only two parameters to adjust for each system. The two PPF controllers were then combined in a diagonal matrix to create a single control algorithm (G_c). The resulting matrix of transfer functions was as follows:

$$G_c(s) = \begin{bmatrix} G_{c1} & 0 \\ 0 & G_{c2} \end{bmatrix} \tag{3.14}$$

The G_c was then fed back using the *feedback.m* function in MATLAB®. The function assumed a negative feedback. The closed loop system transfer function ($G_{cl}(s)$) was mathematically represented as follows:

$$G_{cl}(s) = \begin{bmatrix} \frac{G_{p1}(s)}{1+G_{p1}(s)G_{c1}(s)} \\ \frac{G_{p2}(s)}{1+G_{p2}(s)G_{c2}(s)} \end{bmatrix} \tag{3.15}$$

where is G_{p1} and G_{p2} are the forward and aft system plant transfer functions respectively. A graphical representation of the system is shown in Figure 3.22.
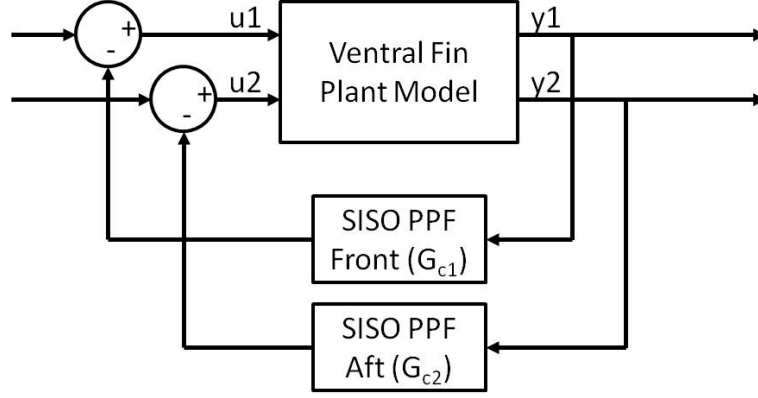
Figure 3.22:   Two Mode SISO PPF Block Diagram

The four-mode configuration was possible by placing the second-order controllers in parallel. For one controller to affect more than one mode, second-order transfer functions for each mode needs only to be added [34]. This method retains the second-order qualities of a single PPF at multiple frequency range without adverse effects [9]. The resulting single controller is shown in Equation 3.16 with the j being the target modes:

$$G_{ci}(s) = \sum_{j=1}^{2} -g_{cij} \left(\frac{\omega_{cij}^2}{s^2 + 2\zeta_{cij}\omega_{cij}s + \omega_{cij}^2} \right) \tag{3.16}$$

The transfer function above was applied to Equation 3.14 and fed back in the same configuration as Equation 3.15 and Figure 3.22.

3.9.2 *Multivariable PPF.*   Multivariable PPF control has been studied and re-arranged by many since Goh and Caughey [42] as well as Fanson [15] introduced it in the 1980's. A modified version was introduced by Kwak for cases where the number of modes to be controlled is not equal to the number of actuators [24]. For this research Kwak's proposed controller development was used. Kwak's controller took the form:

$$\ddot{Q} + 2Z_f\Omega_f\dot{Q} + \Lambda_f Q = G^{\frac{1}{2}}\Lambda_f\hat{C}q \tag{3.17}$$

39

The equation is in modal form where Q is a $n \times 1$ modal control force vector, Z_f is an $n \times n$ damping factor matrix, Ω_f is an $n \times n$ compensator frequency matrix, $\Lambda_f = \Omega_f{}^2$, and G is an $n \times n$ gain matrix. The estimate of modal displacement, q, is a generalized displacement vector. $\hat{C}$ is an identity matrix for a controller with equal number of modes as actuators. For cases of unequal number of modes versus actuators, Kwak introduces a block inverse technique where:

$$C_s = \begin{bmatrix} \bar{c}_{s1} & \bar{c}_{s2} \end{bmatrix} \tag{3.18}$$

then

$$\hat{C} = \begin{bmatrix} I & (\bar{c}_{s1})^{-1}\bar{c}_{s2} \\ (\bar{c}_{s2})^{-1}\bar{c}_{s1} & I \end{bmatrix} \tag{3.19}$$

This block inverse method allows one to estimate the necessary modal coordinates from the available sensor measurements. A similar transformation is applied to the actuator participation matrix, B_a, to obtain actuator signals from modal control force vector, Q. The resulting matrix $\hat{B}$ is an identity matrix for a controller with the same number of modes as actuators or if

$$B_a = \begin{bmatrix} \bar{b}_{a1} \\ \bar{b}_{a2} \end{bmatrix} \tag{3.20}$$

then

$$\hat{B} = \begin{bmatrix} I & \bar{b}_{a1}(\bar{b}_{a2})^{-1} \\ \bar{b}_{a2}(\bar{b}_{a1})^{-1} & I \end{bmatrix} \tag{3.21}$$

Implementing this control algorithm required a specific form of the plant. First a reduced-order model was used to simplify the plant to only the modes that would be targeted. In this case, a reduced-order model with the second and third modes were used. Omitting the higher frequency modes from the plant model has minimal

effect on PPF controller development because of the fast rolloff of the filter at higher frequencies [28]. The lower frequency modes need to be looked at during design parameter selection due to spillover effects that could occur. The filter can have an effect of shifting the natural frequencies of the lower modes, adding flexibility to those modes [23]. Careful selection of damping ratio versus gain was important to keep the spillover effects to a minimum. The specific second-order plant transfer function model required by this method was as follows:

$$\ddot{q} + 2Z\Omega\dot{q} + \Lambda q = B_a v_a, \ v_s = C_s q \tag{3.22}$$

where q is an $n \times 1$ generalized displacement vector, Ω is an $n \times n$ eigenvalue matrix, Z is an $n \times n$ plant damping factor matrix, $\Lambda = \Omega^2$, B_a and C_s are the actuator and sensor participation matrices respectively, and v_a and v_s are actuator and sensor signals respectively.

A simple way to mathematically change the existing diagonal modal ERA model into the required second-order transfer function format above could not be found. To accomplish this modification a first-order state-space representation was necessary. The first-order state-space representation for a two mode setup was as follows:

$$\dot{x} = \begin{bmatrix} 0 & 1 & 0 & 0 \\ -\omega_1^2 & -2\zeta_1\omega_1 & 0 & 0 \\ 0 & 0 & 0 & 1 \\ 0 & 0 & -\omega_2^2 & -2\zeta_2\omega_2 \end{bmatrix} x + \begin{bmatrix} 0 & 0 \\ b_{11} & b_{12} \\ 0 & 0 \\ b_{21} & b_{22} \end{bmatrix} u \tag{3.23}$$

$$y = \begin{bmatrix} c_{11} & 0 & c_{12} & 0 \\ c_{21} & 0 & c_{22} & 0 \end{bmatrix} x + \begin{bmatrix} d_{11} & d_{12} \\ d_{21} & d_{22} \end{bmatrix} u$$

The frequencies and damping ratios were easy to extract from the existing state matrix. An optimization algorithm was used, however, to identify the rest of the variables b, c, and d that fit the first-order state-space model. This method was

41

investigated by Moheimani [28] and proved useful in this case. Moheimani suggested the use of the following cost function as the minimizer to determine the necessary parameters for the required model:

$$J = \sum_{i,j=1}^{2} \sum_{k=1}^{N} \left| \frac{G_{ij}^{N}(j\omega_k) - G_{ij}(j\omega_k)}{G_{ij}(j\omega_k)} \right|^2 \tag{3.24}$$

The i and j represent the input and output number, the k represents the mode, $G_{ij}^{N}(j\omega_k)$ is the magnitude of the i-th actuator and j-th sensor first order fit at the k-th modal frequency ω_k, and $G_{ij}(j\omega_k)$ is the magnitude of the ERA model, reduced to only the two target modes (see Section 3.9.3), at the same frequency. Only the two-mode controller was developed for the MIMO PPF due to the complexity of accomplishing this transformation. The *fminunc.m* function in MATLAB® was used to execute the optimization algorithm. As noted by Moheimani, depending on the initial values of the variables, the results can differ greatly due to many possible local minima. To ensure that the match was accurate, the phase plots of the fit were compared to the reduced ERA model phase plots. Deviations of more than 90 degrees in phase indicated an improper optimization and new initial values were selected.

Once the b and c values were determined, the B_a and the C_s matrices were just a matter of removing the zeros from the input and sensor matrices in equation 3.23, and this relationship holds for the first-order state-space representation. Equation 3.25 shows the resulting participation matrices.

$$B_a = \begin{bmatrix} b_{11} & b_{12} \\ b_{21} & b_{22} \end{bmatrix}, \; C_s = \begin{bmatrix} c_{11} & c_{12} \\ c_{21} & c_{22} \end{bmatrix} \tag{3.25}$$

With the proper modal format identified, the controller (Equation 3.17) and the plant (Equation 3.22) is combined to produce the coupled structure-compensator

equation:

$$\left\{ \begin{array}{c} \ddot{q} \\ \ddot{Q} \end{array} \right\} + \left[\begin{array}{cc} 2Z\Omega & 0 \\ 0 & 2Z_f\Omega_f \end{array} \right] \left\{ \begin{array}{c} \dot{q} \\ \dot{Q} \end{array} \right\} + \left[\begin{array}{cc} \Lambda & -\hat{B}G^{\frac{1}{2}}\Lambda \\ -G^{\frac{1}{2}}\Lambda_f\hat{C} & \Lambda_f \end{array} \right] \left\{ \begin{array}{c} q \\ Q \end{array} \right\} = \left\{ \begin{array}{c} 0 \\ 0 \end{array} \right\}$$

(3.26)

From this coupled equation, the closed loop system is stable if the following condition is met:

$$\left[\begin{array}{cc} \Lambda & -\hat{B}G^{\frac{1}{2}}\Lambda \\ -G^{\frac{1}{2}}\Lambda_f\hat{C} & \Lambda_f \end{array} \right] > 0$$

(3.27)

This stability condition was one criterion that was verified before continuing with the controller selection process. The final format of the two-input two-output MIMO PPF controller in transfer function form, for equal number of actuators to target modes, was:

$$G_c(s) = -B_a{}^{-1}G^{\frac{1}{2}}\Lambda H_{PPF}(s)G^{\frac{1}{2}}C_s^{-1}$$

(3.28)

$H_{PPF}(s)$ is a diagonal of single PPF transfer functions targeting each mode as shown in equation 3.29.

$$H_{PPF}(s) = \left[\begin{array}{cc} H_1(s) & 0 \\ 0 & H_2(s) \end{array} \right]$$

(3.29)

When combined, the transfer function for the controller becomes:

$$G_c(s) = \left[\begin{array}{cc} G_{c1} & G_{c2} \\ G_{c3} & G_{c4} \end{array} \right]$$

(3.30)

The controller above was fed back with a negative feedback the same way as in the SISO PPF control. Figure 3.23 is the graphical representation of the entire system.
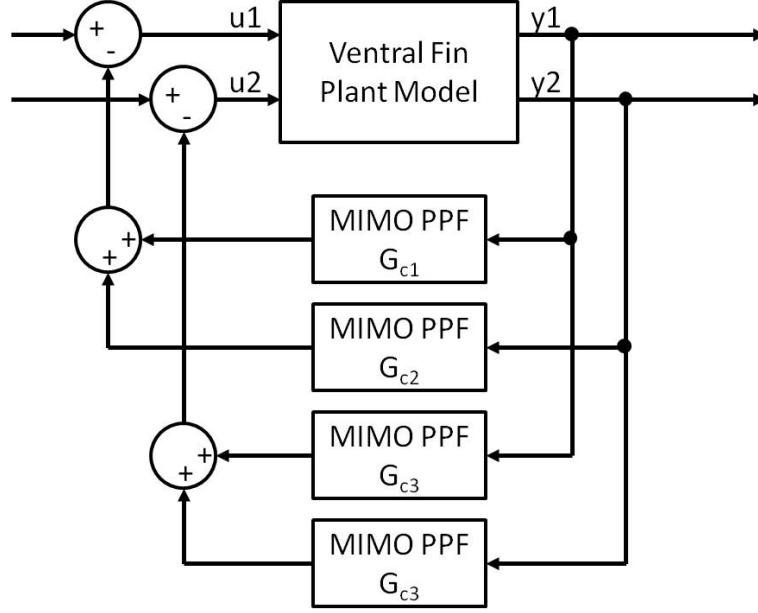
Figure 3.23:   Two Mode Multivariable PPF Block Diagram

The key difference between MIMO and SISO PPF controllers was the use of the participation matrices in the control algorithm to have all actuators and sensors work together to attenuate the vibrations at the target modes.

3.9.3   MIMO LQG.   The LQG control is a commonly used algorithm that combines the LQR and the LQE. The algorithm is more complex than the PPF algorithm and requires significant computational power to implement.

LQR is an optimal control problem where the cost function is quadratic and the full-state information is known. Detailed description of the theory can be found in the text book by Burl [10] and will not be covered here. The application of the of the LQR is ideal for vibration control because of the optimal control problem that attempts to minimize the energy in the states. The design parameters for the LQR were the state weighting matrix ($\mathbf{Q}$) and the control weighing matrix ($\mathbf{R}$) in the steady-state LQR cost function:

$$J\left(x(t), u(t)\right) = \frac{1}{2}\int_0^\infty x^T(t)\mathbf{Q}x(t) + u^T\mathbf{R}u(t)dt \qquad (3.31)$$

The diagonals of the state weighting matrix corresponds to the modes of the ventral fin when the plant model is diagonalized with the eigenvalues on the diagonal. For first-order modes, the eigenvalue is real only and takes up one element while a second-order modes are real plus imaginary and takes up two elements. Minimizing the $\mathbf{Q}$ term of the cost function minimizes the average energy in the system, damping out the appropriate modes [10]. Equation 3.32 is the format of the weighting matrix used for this research where n is the number of states in the plant model.

$$
\mathbf{Q} = \begin{bmatrix} q_1 & 0 & 0 & & 0 \\ 0 & q_2 & 0 & \cdots & 0 \\ 0 & 0 & q_3 & & 0 \\ & \vdots & & \ddots & 0 \\ 0 & 0 & 0 & 0 & q_n \end{bmatrix}
\tag{3.32}
$$

The q_n terms were chosen appropriately to achieve the desired control. For any modes that did not require control, their corresponding q terms were set to zero. This meant that only the q's corresponding to the target modes had a positive value. Each pair of q that belonged to the same modes were set to the same value. For example, if mode one states corresponded to q_1 and q_2 then $q_1 = q_2$. The q values were kept at positive values to meet one of the requirements for the cost function, which was for the $\mathbf{Q}$ matrix to be positive definite.

The control weighting matrix term minimizes the energy required to perform the control. The size of $\mathbf{R}$ depended on how many inputs were used for the system. For an l input system, $\mathbf{R}$ is a $l \times l$ diagonal matrix with each element corresponding

to an input (equation 3.33).

$$\mathbf{R} = \begin{bmatrix} r_1 & 0 & 0 & & 0 \\ 0 & r_2 & 0 & \cdots & 0 \\ 0 & 0 & r_3 & & 0 \\ & \vdots & & \ddots & 0 \\ 0 & 0 & 0 & 0 & r_l \end{bmatrix} \tag{3.33}$$

The goal of the optimization problem was to find the regulator matrix ($\mathbf{K}$) in Equation 3.34 that minimizes the cost function.

$$u(t) = -\mathbf{K}(t)x(t) \tag{3.34}$$

The regulator matrix was derived in this research using the *lqr.m* function in MATLAB®, where by providing it with the plant model and the weighting matrices it solves the Riccati equation to determine the matrix $\mathbf{K}$. Details on the Riccati equation can also be found in Burl [10].

The second part of LQG control is the LQE. The LQE is a Kalman filter that estimates the state of a plant given a set of known inputs and a set of measurements [10]. As mentioned in Section 2.4, the LQR can only function if the entire state information is known. The state information available is limited to the observable states from the existing sensors. The Kalman filter fills in that void and estimates all the states from the measurements to allow the LQR to work on more modes. The Kalman filter design process begins by assuming that the plant model includes unknown random input noise ($w(t)$) and random measurement noise ($v(t)$). The following equations represents the plant model with the added inputs and noise:

$$\begin{aligned} \dot{x}(t) &= \mathbf{A}x(t) + \mathbf{B}_u u(t) + \mathbf{B}_w w(t) \\ y(t) &= \mathbf{C}_y x(t) + v(t) \end{aligned} \tag{3.35}$$

where $\mathbf{B}_u$ is the known input matrix, $\mathbf{B}_w$ is the unknown random input matrix, and $\mathbf{C}_y$ is the known sensor matrix. The Kalman filter is another optimization problem that minimizes the error in the state estimates. First the random input and measurement noise covariances are represented by $\mathbf{S}_w$ and $\mathbf{S}_v$ as follows:

$$E[w(t)w^T(t+\tau)] = \mathbf{S}_w\delta(\tau) \tag{3.36}$$

$$E[v(t)v^T(t+\tau)] = \mathbf{S}_v\delta(\tau) \tag{3.37}$$

In the method approached by Burl, the two matrices are determined either theoretically or empirically. In this research determination of the two matrices were not possible and the values of identity were used, which simply indicated that all spectral densities are equal.

The two matrices and the plant model were fed into the function *lqe.m* in MATLAB®, which ran the Riccati equation for the estimator [10] to come up with the estimator gain ($\mathbf{L}$). The Riccati equation solves for the covariance matrix of the estimation error ($\mathbf{\Sigma}_e(t)$) using the two matrices. Equation 3.38 shows the final form of $\mathbf{L}$.

$$\mathbf{L}(t) = \mathbf{\Sigma}_e(t)\mathbf{C}_y^T\mathbf{S}_v^{-1} \tag{3.38}$$

Another problem that had to be dealt with was the unknown $\mathbf{B}_w$ matrix which was used in the Riccati equation to determine $\mathbf{\Sigma}_e(t)$. There was no model or experimental data to determine this matrix. To combat this problem, the loop transfer recovery (LTR) method was used. LTR is traditionally used to recover the robustness of an LQR controller that is lost in LQG controller. LTR adds a fictitious noise to the control system that affects the Kalman filter's reliance on the control input reducing the dynamic effects of the filter on the system. This results in achieving the robustness gained by a full-state regulator [10]. The fictitious noise, w_f was added to the plant

state equation 3.40 before proceeding with the LQG design.

$$\dot{x}(t) = \mathbf{A}x(t) + \mathbf{B}_u u(t) + \mathbf{B}_w w(t) + \mathbf{B}_u w_f(t) \tag{3.39}$$

In this research the unknown plant noise, w, was ignored and assumed to be part of the fictitious noise, w_f since there was no way to determine w. A scalar multiplier (q) was added to the $\mathbf{B}_u$ as another design parameter to change the fictitious noise participation. As the multiplier was changed, $\boldsymbol{\Sigma}_e(t)$ was affected and resulted in a new $\mathbf{L}$. Equation 3.40 was modified and the controller was developed using the following plant state equation:

$$\dot{x}(t) = \mathbf{A}x(t) + \mathbf{B}_u u(t) + q\mathbf{B}_u w_f(t) \tag{3.40}$$

where q for simplicity's sake, was a single multiplier applied to all components of $\mathbf{B}_u$.

$\mathbf{S}_w$ and $\mathbf{S}_v$ matrices were set to identity and q set to one to limit the scope of this research. This limitation may not have led to the best solution for $\mathbf{L}$ during this research and further investigation is required to assess the effects of these parameters on the controller. It is, however, expected to change the robustness of the controller.

Finally to develop the LQG control, the Regulator gain and the Kalman gain was combined as follows:

$$\dot{x}(t) = [\mathbf{A}_p - \mathbf{L}\mathbf{C}_p - (\mathbf{B}_p - \mathbf{L}\mathbf{D}_p)\mathbf{K}]\, x(t) + \mathbf{L}u(t)$$
$$y(t) = \mathbf{K}x(t) \tag{3.41}$$

Equation 3.41, as is, produces a controller with the same number of states as the plant model used. As will be noted in Section 3.10, the control computer adds computational delay as the number of states are increased. The number of states for the LQG control was limited to 12 to allow for estimation beyond the target modes but also to keep the computational delay low. Because of the plant state-space model was set up in diagonal form, the controller states were reduced to the first 12 states, which cor-

responded to the first 12 plant states. This model reduction method was studied by Henriot and determined to be the most efficient method while retaining the accuracy of the lower frequency dynamics despite the missing higher order states [16]. Figure 3.24 shows a comparison of a sample full state LQG controller versus a reduced state LQG. As can be seen from the plot, this method of model reduction maintained the
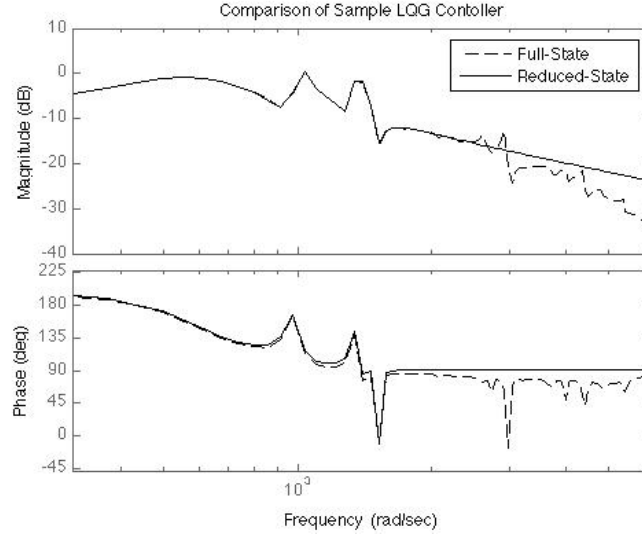
Figure 3.24:   Sample Reduced State Controller

same properties of the controller at the target frequencies and had minimal effects at higher frequencies due to the controllers roll-off in magnitude that already existed from the design. The resulting 12-state controller was then fed back with a negative feedback the same as in the SISO and multivariable PPF controller.

3.10   Stability Margins

Stability analysis is always an important task for any control design process. In addition to the traditional gain and phase margin requirements to ensure adequate safety margin, one of the criteria for the control algorithm was that the phase margins had to be large enough to ensure that there would still be that safety margin in phase after the discretization process. Converting from continuous to discrete (analog to digital) adds a phase delay equivalent to the frequency times the sample time. In

Table 3.5:   Phase Delays at 200 Hz

Controller	States	Sample Time (sec)	Phase Delay (deg)	Time Delay (sec)
SISO PPF	4	1/10000	14.2	2.0
SISO PPF	4	1/40000	4.6	2.6
LQG	8	1/10000	11.3	1.6
LQG	8	1/40000	4.7	2.6
LQG	12	1/10000	9.1	1.3
LQG	12	1/40000	5.1	2.8

addition the digital controllers processing speed (transport time delay), the signal conversion (zero order hold) process adds more phase delay. The capability of the digital controller (MABXII) was experimentally determined using various control algorithms run through SigCalc to compare the phase plot of the FRF's at different frequencies. Table 3.5 shows the phase delays and the equivalent time steps for different sample times and control algorithms at 200 Hz. The control algorithms were deemed acceptable if the most conservative phase margins (the independent phase margin) were greater than the above phase delays. At 40 kHz sample rate, a phase margin of 10 degrees or greater (twice that of actual phase delay) was considered adequate to take into account the digitization phase delay.

Margins were meaningless if the closed-loop system was unstable. The basic determination of stability came from looking at the poles of the closed-loop system. It can be shown from the following equation of the closed-loop system derived from the plant transfer function (G_p) and the controller (G_c),

$$G_{cl} = \frac{G_p}{1 + G_p G_c} \qquad (3.42)$$

is stable if and only if the solutions to the characteristic equation,

$$1 + G_p G_c = 0 \qquad (3.43)$$

all have negative real parts [10]. The solutions to the characteristic equation correspond to the closed-loop poles of the system. For each candidate algorithm, this

stability criteria was checked by ensuring all the solutions had a negative real part. This check was implemented using the function *damp.m* in MATLAB® to produce all the poles for the system by calculating the eigenvalues of the *A* matrix for the state-space closed-loop model.

Once the stability of the system was determined, traditional gain and phase margins were calculated by looking at the Bode plot of the open-loop system. The gain margin was the difference in amplitude from zero dB at the point where the phase crossed -180 degrees. The phase margin was the difference in phase from -180 degrees at the point the amplitude crossed the zero dB point. Since the ventral fin and the closed-loop system was complex, the bode plot was not the most practical method to determine the margins. Another method of determining the stability of the system was to look at the Nichols chart. The Nichols chart provided an alternative graphical method for stability analysis and was more suited for structural applications where there are multiple modes and typically multiple gain and phase margin points. Figure 3.25 is an example of an open-loop gain and phase of a stable and unstable SISO system plotted on the Nichols chart. From zero dB and -180 degree point, the vertical distance to the open-loop system is the gain margin and the horizontal distance is the phase margin. As seen in the figure as long as the open-loop plot does not go above the zero dB and left of the -180 degree point, the gain margin stays positive and the system is stable.

The methods described above worked well for SISO systems where the gain and phase margins were strictly dependent on the one system. Application to the MIMO system was not as direct due to the interactions between the different inputs and outputs. Two stability analysis methods were used for the MIMO systems. The first was to break the system into single loops and applying the SISO stability analysis described above. The second was to use Ridgely and Banda's independent gain and phase margin concept.

51
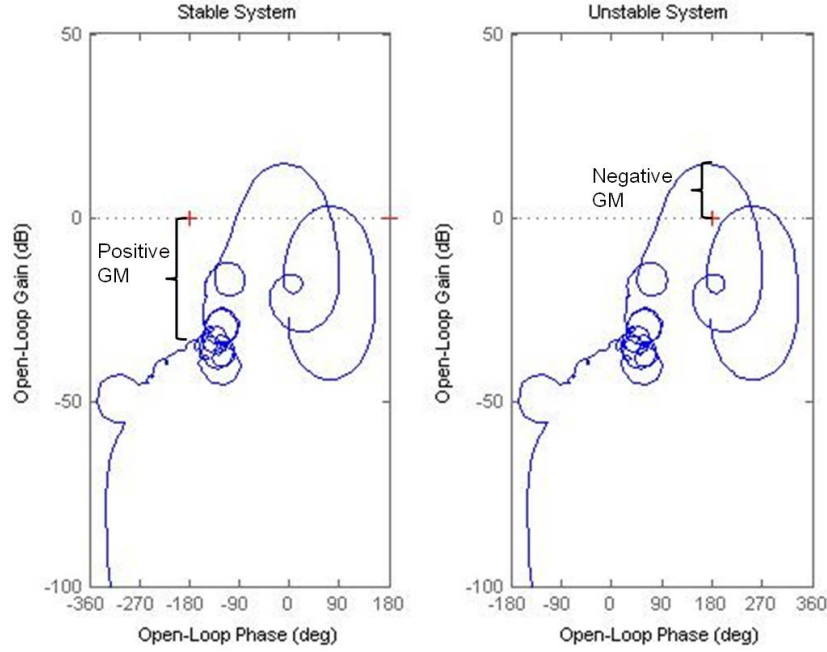
Figure 3.25:   Nichols Chart Stability Example

The first method takes the SISO gain and phase margin development and applies it to the MIMO system. By opening a single loop at the input or output, the gain and phase margin of that loop can be calculated while keeping the gain and phase of the other loops at nominal values. This concept was suggested for SISO, multi-input single-output, and single-input multiple-output systems by Ridgely and Banda [36] but was applied to the MIMO system as another form of stability test during this research. This test was applied to the two-input two-output system and the margins were calculated by breaking the loop at each input and output. This resulted in four loops, which then the Nichols plots were drawn and the margins calculated. Figure 3.26 is an example of the first input, u_1, loop opened. The margins are then calculated for the u_{1i} and u_{1o} system. Three more loops were created by accomplishing similar breaks at u_2, y_1 and y_2.

The idea of independent gain and phase margins (IGM and IPM) was derived in detail by Ridgely and Banda and used the concept of singular values. The derivation

52
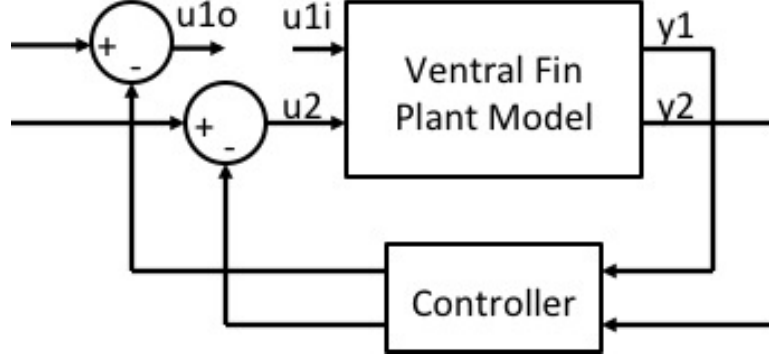
Figure 3.26: One Loop at a Time Example

of the IGM and IPM can be found in [36] in detail. In summary, Ridgely and Banda
proved that the gain space or the region of stability can be expressed by using the
minimum singular value of the characteristic equation. The equation for the stable
gain space is:

$$\frac{1}{1 + a_0} < \text{Stable Gain Space} < \frac{1}{1 - a_0} \tag{3.44}$$

where $a_0 = \underline{\sigma}[I + G_p(s)G_c(s)]$ (the minimum singular value) or 1, whichever is less.
In the same way as the IGM, the IPM can also be determined by using a_0 in the
following equation:

$$-2sin^{-1}(\frac{a_0}{2}) < \text{Stable Phase Space} < 2sin^{-1}(\frac{a_0}{2}) \tag{3.45}$$

Since the minimum singular value was taken and used to derive the gain and phase
margins, the IGM and IPM was the worst case scenario. If these margins meet the
design criteria, then the rest of gain and phase margins will be better. The function
$sigma.m$ in MATLAB® was used to find the minimum singular value of the system.
Figure 3.27 shows an example singular value plot of a 2×2 system, showing both the
maximum and minimum singular values as a function of input frequency.

The margin design criteria used is described in Table 3.6. These values were
chosen to allow enough margin to ensure a stable system in any condition. The

53
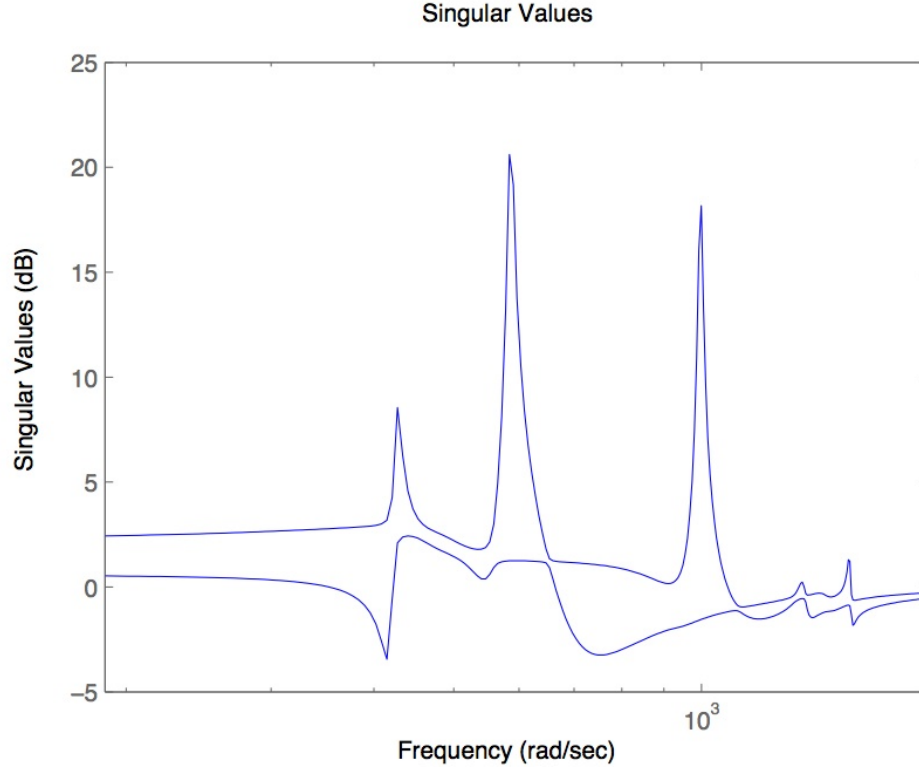
Figure 3.27:   Singular Value Plot Example

Table 3.6:   Stability Margin Crieteria

Margin	Criteria
Single Loop Gain	> 6 dB
Single Loop Phase	$> 16°$
Independent Gain	> 6 dB
Independent Phase	$> 16°$

minimum gain margin was chosen to be 6 dB, a common number chosen for gain margin criteria in feedback control [10]. The minimum phase margin was chosen to be 16 degrees. This number was picked by taking the phase lag seen in the 12-state LQG in Table 3.5 and multiplying by a safety factor of π, or 3.14 (a commonly used safety margin).

3.11 SIMULINK® Simulation

One limitation in the control algorithm that had to be taken into account was the maximum control signal. Since the amplifier would be limited to its maximum voltage output of 700 volts peak (see Section 3.6), the control signal had to be within that range to stay linear. For this simulation, sensor signals with the highest amplitude from ACTIVE FIN flight test [8] were fed into the sensor measurements (s_1 and s_2) of the SIMULINK® model (Figure 3.28) and the output of the controller (u_1 and u_2) were evaluated to see if the control signals were within range. Controlled sensor output (y_{c1} and y_{c2}) were also looked at to ensure the vibrations were being attenuated.
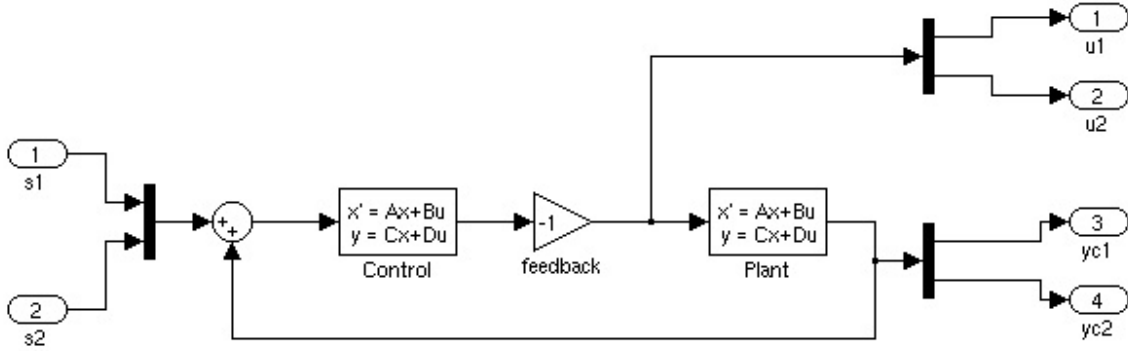
Figure 3.28:   SIMULINK® Simulation Model

The sensor measurements from ACTIVE FIN (V_{AF}) were first modified as equivalent signals (V_{eq}) for the lab setup by multiplying the voltage gain ($g_{div} = 15$) used in ACTIVE FIN and then by the gain difference between the raw voltage sensor and the charge converter ($g_{cc} = 1/1.4$), which was determined by inputting a known signal and measuring both outputs at the same time.

$$V_{eq} = g_{div}g_{cc}V_{AF} = \frac{15}{1.4}v_{AF} \tag{3.46}$$

Continuous models of both the plant and the controller were used for this simulation. The controller values were deemed acceptable if the peak of the control signals from the simulation multiplied by the amplifier gain ($\times 200$) were within the maximum

allowable voltage range. An example output of the simulation is shown in Figure 3.29 comparing the control signal (u_1) to the input signal (s_1).
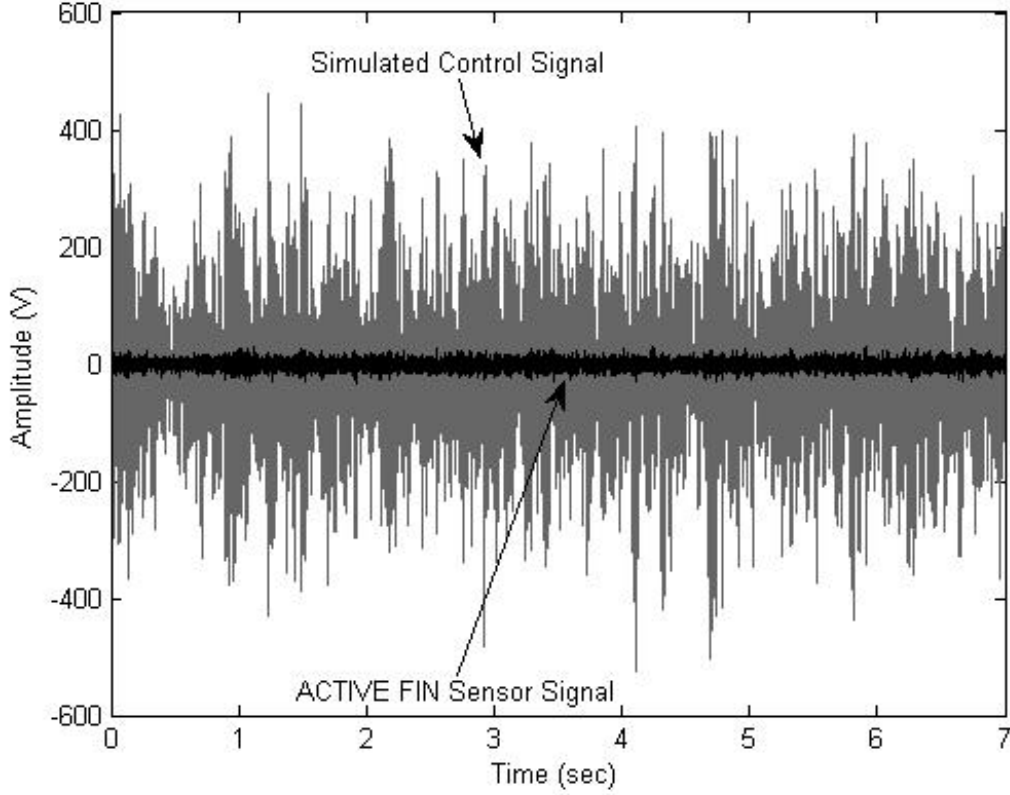
Figure 3.29:   Example of SIMULINK® Simulation Output

3.12 Laboratory Experimental Analysis

The control algorithms that met the requirements were tested in the laboratory on the actual fin to determine its actual performance. In the laboratory, the sensor signals were only fed through the charge converter and the actuator signals were amplified using Trek Model PZD700 Piezo Driver/Amplifiers. The dSpace DS1103 digital controller was used with its associated software package, dSpace ControlDesk V.2.6.5. The SIMULINK® model used for implementing the control on dSpace accounted for the inversion of the control signal to the opposite actuators for the 2×2 controller. Due to the minimal disturbance force that was going to be applied in

the laboratory, the offsetting of the actuator signal mentioned in Section 3.8 was not applied. An example SIMULINK® model used for testing the MIMO PPF control is shown in Figure 3.30.
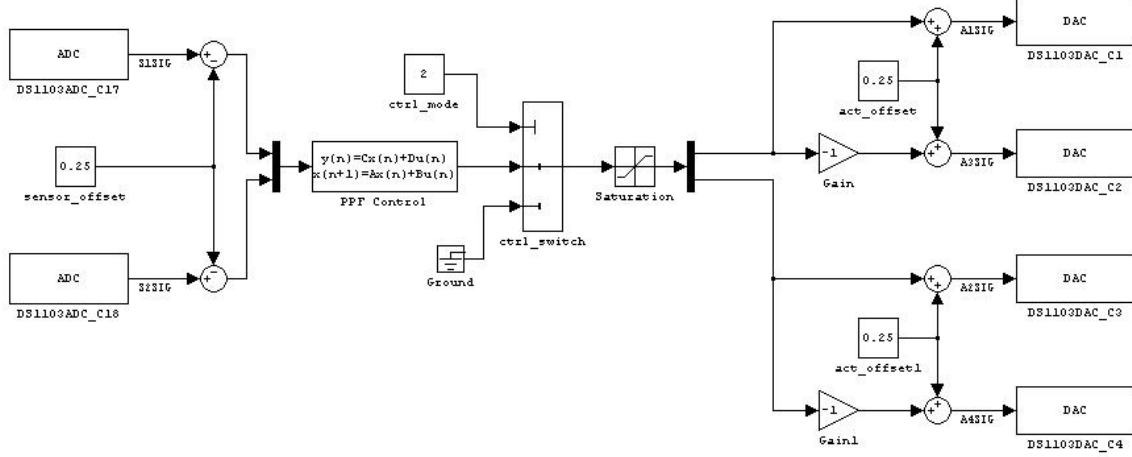
Figure 3.30:   SIMULINK® Model of PPF Control Used in the Laboratory with dSpace DS1103

So far the control algorithms were developed in the continuous domain. Now that the controller had to be implemented into an actual control computer, discretization of the control algorithm was required to ensure accurate translation of the continuous model. The *c2d.m* function in MATLAB® was used with the default zero-order-hold (ZOH) method. The ZOH method converted the continuous model into a discrete model in the time domain by holding each sample value constant over the sample period.

$$\underline{x}(t) = e^{\mathbf{A}(t-t_0)}\underline{x}(t_0) + \int_{t_0}^{t} e^{\mathbf{A}(t-\tau)}\mathbf{B}u(\tau)d\tau \tag{3.47}$$

Equation 3.47 allows the calculation of the state vector at any time t given the state vector at time t_0 and the control input, $u(t)$, between t and t_0. In the discrete space, the point of interest is the next sample time compared to the current. If the current

sample instance, $t_0 = kT$, then the state vector at the next sample instance becomes:

$$\underline{x}(kT + T) = e^{\mathbf{A}T}\underline{x}(kT) + \int_{kT}^{kT+T} e^{\mathbf{A}(kT+T-\tau)}\mathbf{B}u(\tau)d\tau \qquad (3.48)$$

This discrete state vector equation can be manipulated to derive the discrete state-space model. A simplified derivation can be found in [32]. The final result is the following equation:

$$\begin{aligned}
\underline{x}(k+1) &= \mathbf{\Phi}\underline{x}(k) + \mathbf{\Gamma}u(k) \\
y(k) &= \mathbf{C}\underline{x}(k) + \mathbf{D}u(k)
\end{aligned} \qquad (3.49)$$

where

$$\mathbf{\Phi} = \mathbf{I} + \mathbf{A}T\mathbf{\Psi}, \ \mathbf{\Gamma} = T\mathbf{\Psi}\mathbf{B} \qquad (3.50)$$

and

$$\mathbf{\Psi} = \mathbf{I} + \frac{\mathbf{A}T}{2!} + \frac{(\mathbf{A}T)^2}{3!} + ... \qquad (3.51)$$

The resulting discrete state matrix $\mathbf{\Phi}$, input matrix $\mathbf{\Gamma}$ and the same $\mathbf{C}$ and $\mathbf{D}$ matrices were used in the Discrete State-Space block in SIMULINK® to implement in the control computer. Sample time, T, of 1/40000 sec was used for all algorithms during the laboratory tests.

Once the control algorithm was programmed into dSpace, performance was measured by comparing the impulse responses of an uncontrolled and controlled fin. To collect the necessary FRFs of the open and closed-loop system, an impact hammer was used as the excitation force and an accelerometer, forward sensor, and the rear sensor, were used as the measurements. The impact hammer was applied at a constant point on the fin chosen arbitrarily near the bottom front of the fin (Figure 3.31). The
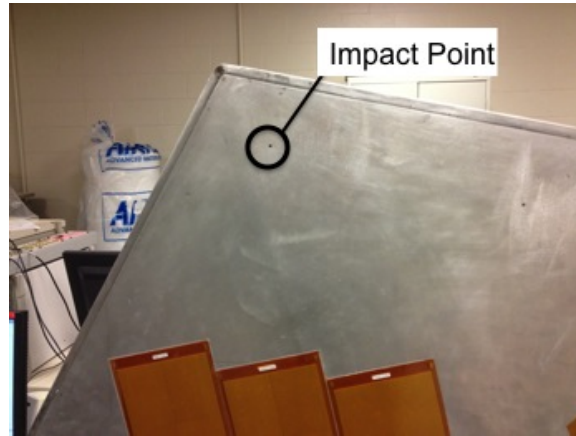
Figure 3.31:   Impact Hammer Location

accelerometer was placed on the front bottom tip of the fin, expecting the magnitudes of the acceleration to be the largest at that point (Figure 3.32).
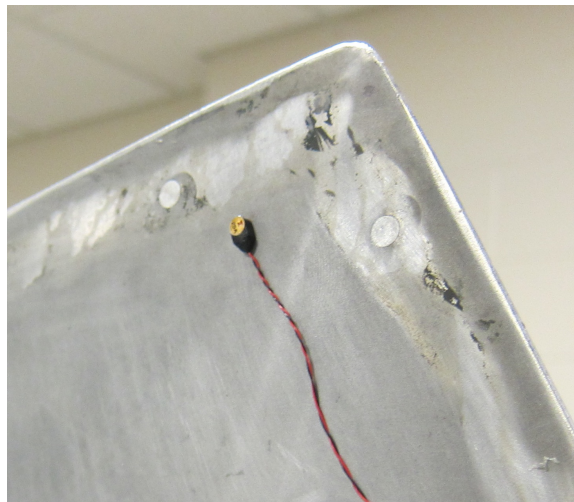
Figure 3.32:   Accelerometer Location

SigCalc 620 was used again to collect FRF data of the complete system, once with the controller off and another with the controller on. The setup in Table 3.7 was used in SigCalc to collect the data. The overall system is represented graphically in Figure 3.33. The actual attenuations were determined by comparing the controlled and uncontrolled FRFs directly. The attenuation level (dA), in dB, was taken as the difference between the controlled and uncontrolled magnitudes at each modal

Table 3.7:   SigCalc Setup for Controller Testing

Parameter	Setting
F Span	1600 Hz
Lines	3200
Overlap	25% Hann
Avg	10 Stable
Trig	Free Run
Window (Hammer)	Rect (width 500 msec)
Window (Sensors)	Rect (width 1.5 sec)
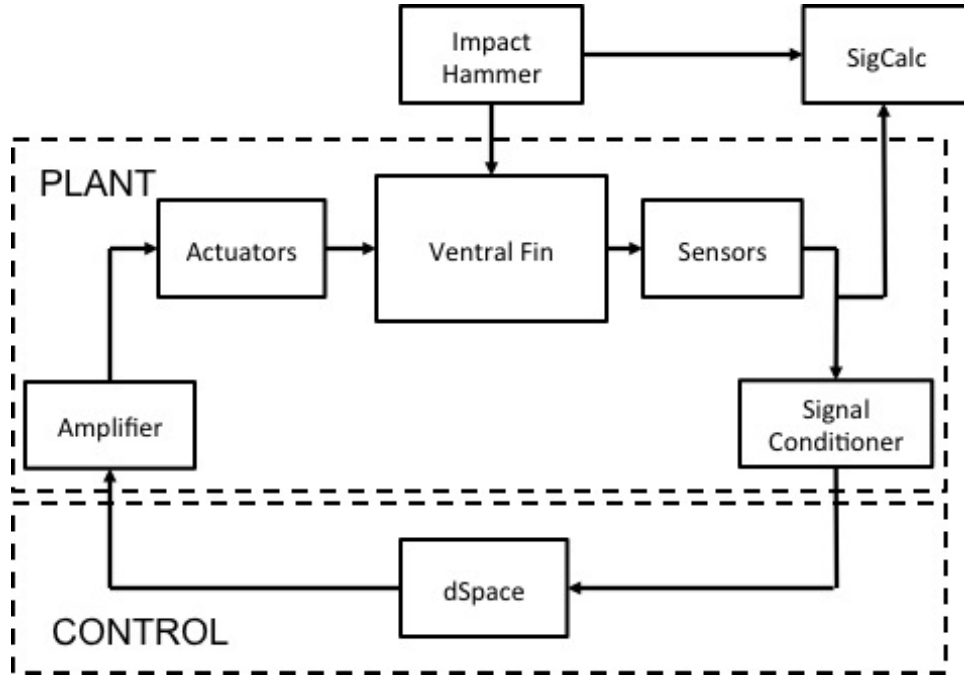
Figure 3.33:   Diagram of Controller Test Setup

frequencies (equation 3.52).

$$dA|_{dB} = 20log_{10}(|H_{\text{uncontrolled}}(j\omega_i)|) - 20log_{10}(|H_{\text{controlled}}(j\omega_i)|)$$
$$i = \text{Mode 1, 2, 3, ...}$$

(3.52)

Comparisons were made at each target mode for each sensor as well as the total attenuation of all target modes at each sensor and the average attenuation of all modes at each sensor.

60
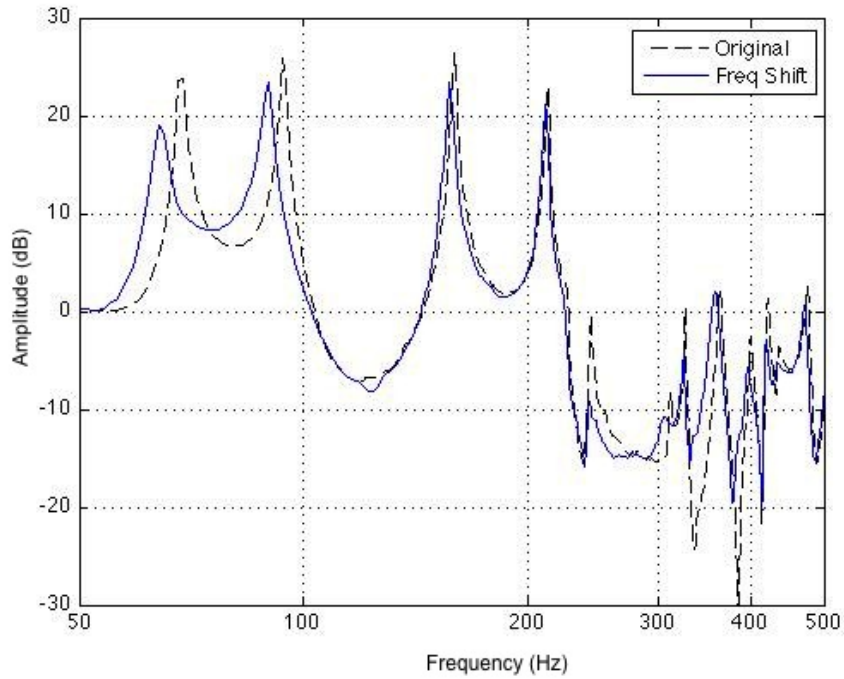
Figure 3.34:   Modified Plant with Frequency Shift

3.13   Robustness Testing

Once the final design parameters were chosen for each algorithm, a robustness test was conducted by observing how effective the control would be if the plant characteristics change. The plant model thus far was modeled and the control designed for a ventral fin mounted on a laboratory table. The modal frequencies can shift and change the characteristics of the fin just by loosening of a bolt on the mount. This means that when the fin is mounted on the aircraft, there may be significant shifts in the modal frequencies. The test consisted of adding a mass on the structure and conducting the same experiment as in Section 3.12. A ten pound mass was placed on the center of the bottom edge of the fin, which successfully shifted the modal frequencies up to 6 Hz. Figure 3.34 shows the new mass-added ventral fin versus the original. The controller was then tested on this modified fin and the performance was measured at the new modal frequencies.

61

3.14 Custom Amplifier Testing

The custom power amplifier built by AFIT's Sean Miller was tested to determine its suitability for the flight test application. The custom amplifier uses the F-16's 28-volt DC power source for general powering of the internal components and the 115-volt 400 Hz AC power source for the high voltage amplification. The amplifier is a class-D switching amplifier that takes in an analog signal and outputs a differential high voltage signal to the actuator. The amplifier test consisted of collecting plant transfer function data for both 2×2 and 4×2 systems and testing sample control algorithms to determine performance. The same procedures as in Section 3.12 was followed.

This chapter established the methods for designing the controller algorithm for a particular structure. Once the fin was identified, the actuators and sensors were installed, and control system components were assembled, the controller design process began with determining a mathematical plant model. This was followed by designing the controllers by modifying the design parameters. The margins were then calculated and the power requirements were determined through simulation to determine compliance with the design criteria. Once the controllers were designed, they were tested in the laboratory to determine their actual performance. The next chapter covers the results of this process.

IV. Results and Analysis

This chapter presents the results and analysis of the research. The chapter covers the results of all steps mentioned in Chapter III starting from the component tests. The chapter will also cover the results of characterizing the plant system and present the models used for testing. Then the chapter covers the results of the controller design process, the effectiveness of those controllers and of the additional tests conducted for flight application.

4.1 System Design

Once the patches were installed and appropriate wiring connected, the system components were tested with a laboratory amplifier. The first issue that became apparent early was the need to remove the 100:1 charge attenuators because the sensor signals were much too low, in the range of ± 5 mV, with the available fin excitation methods. Once the charge attenuator was removed, excitations by an external force, such as the palm of the hand, was large enough to saturate the sensor. The relationship between the charge converter voltage output and direct sensor output was compared and the direct output had a 1.4 times greater voltage magnitude than the charge converter output. From this result, the 100:1 charge attenuator requirement was re-evaluated and a 20:1 charge attenuator is recommended instead. Since the direct sensor signal (from ACTIVE FIN [8]) that was seen was less than ± 200 volts, that value was divided by 10, the peak-to-peak range of the charge converter. This led to the change in charge attenuation from 100:1 to 20:1.

No other shortcomings were found in the system design with the laboratory amplifier.

4.2 Plant Characterization

The plant was characterized with the laboratory amplifier for both the two-input two-output and four-input two-output plant. Figure 4.1 shows the Bode magnitude

plot of the FRF collected through sigCalc 2x2 model and Figure 4.2 shows the same plot for the 4×2 plant.
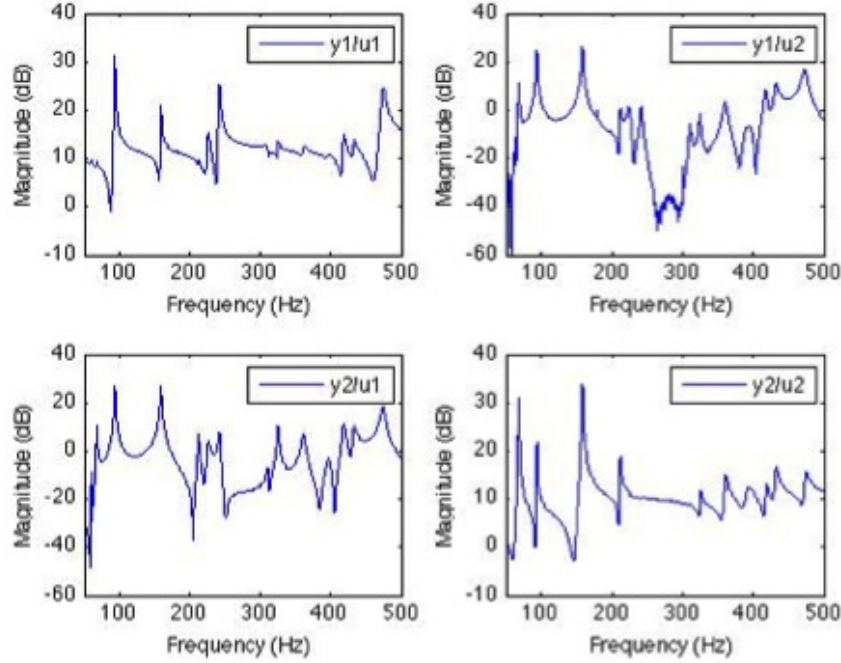
Figure 4.1: 2×2 Plant FRF

ERA was applied using Cobb's ERA Toolbox and a 60-state 2×2 model and a 80-state 4×2 model was developed. A result of the ERA fit of the y_1/u_1 FRF is shown in Figure 4.3. The full ERA model plots can be found in Section A.1.

The 60-state and 80-state ERA models both covered all the way beyond 1000 Hz. This coverage of frequency range was plenty to have an accurate model to be used in simulations as well as for controller design. It was noted that there was a slight shift in modal frequencies of the fin, but was attributed to the stiffness added by the installation of the piezo actuators. The first four modes now corresponded with 68.35, 94.20, 159.14, and 212.59 Hz. The deviation of the phase plot at higher frequencies was also an expected result due to the ERA software calculating a continuous model rather than a discrete model. The software will output either continuous or discrete realizations, but continuous was used for the control design and testing. The phase

64
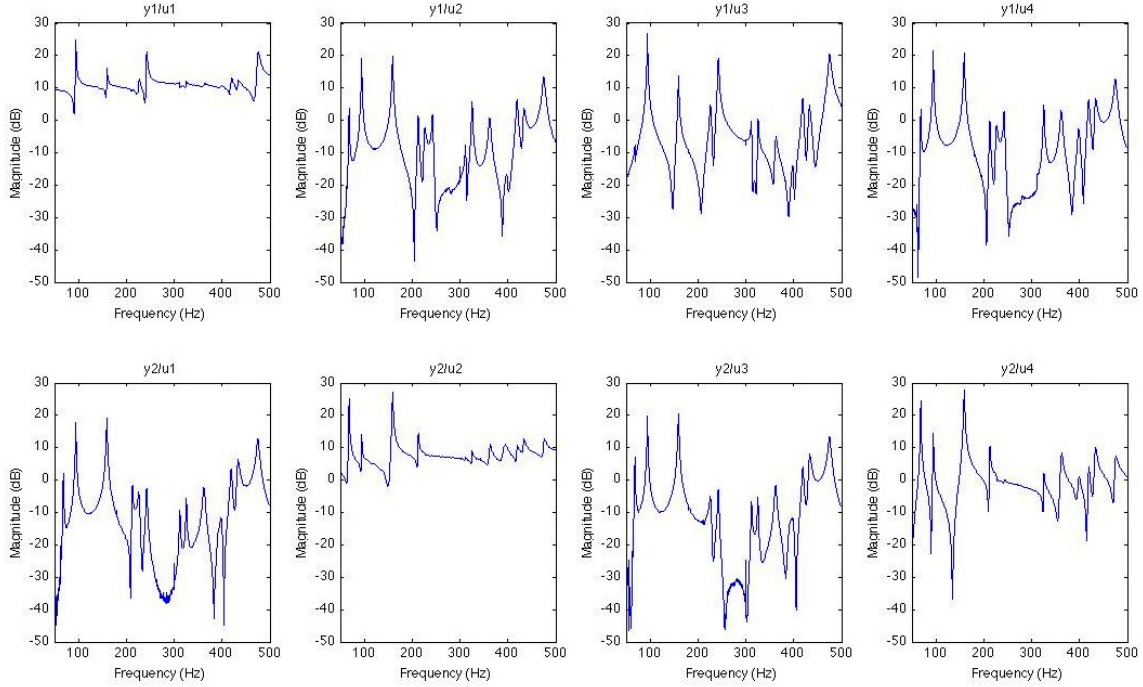
Figure 4.2: 4×2 Plant FRF

delay is a direct effect of discretizing at the sample time used when collecting the data on SigCalc. Use of the resulting continuous model did not affect the outcome of the research. As a note, MATLAB® allows for the controller design process to be conducted completely in discrete methods, but this was not explored during this research.

4.3   Control Algorithm

Overall the effectiveness of the controllers were surprisingly similar. The attenuation level achieved and the resulting closed-loop Bode plots were all very similar as well. The biggest differences were the efficiency of the controller's use of the actuators and the stability margins. Bode plots of the best controllers can be found in Section A.3. Results of all tested controllers can be found in Tables A.1 and A.2.

4.3.1 SISO PPF.   The SISO PPF algorithm was the simplest to develop because of inherent properties of the PPF filter. Each targeted mode was mainly

65
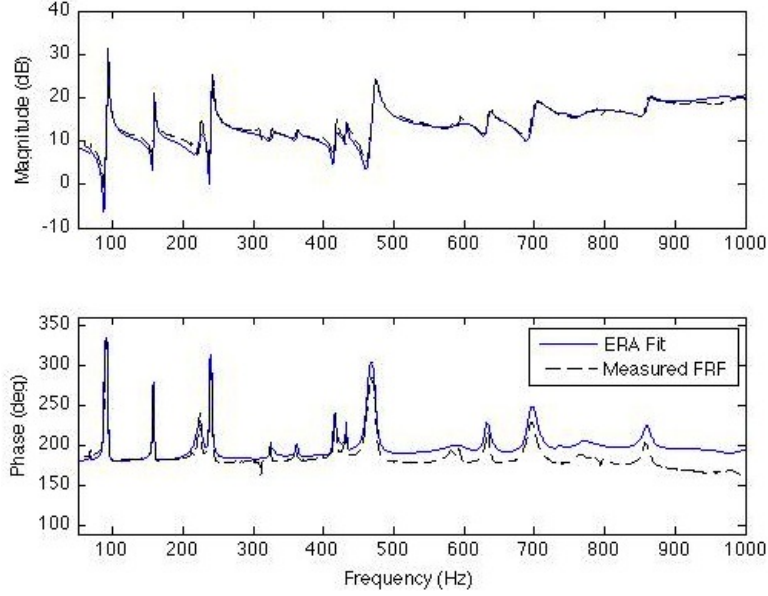
Figure 4.3:   ERA Fit of y_1/u_1 FRF

Table 4.1:   Two Mode SISO PPF Design Parameters

System	Frequency (ω_f)	Damping Ratio (ζ_f)	Gain (g_f)
Front	94.20	0.2	0.09
Aft	159.14	0.2	0.05

isolated from any other mode and the interaction between the two systems (forward and aft) was minimal that the change in design parameters in each did not significantly affect the margins or performance. In general a damping ratio of 0.2 was the best compromise between balancing performance versus stability. Increasing the controller damping ratio, the attenuation was lower but the margins were greater, while decreasing the damping ratio increased the attenuation but also decreased the margins.

For the two-mode SISO PPF, with each system only targeting one mode, the results were as expected and each mode was attenuated. The design parameters for the final two-mode SISO PPF controller is listed in Table 4.1.

The resulting IGM and IPM when both systems were combined were 11.46 dB and 21.5 degrees. The single-loop margins were determined from the Nichols plot of

66

individual systems shown in Figure 4.4. The gain and phase margins for the front system were 39.7 dB and 68.2 degrees respectively. The margins for the aft system were 33.2 dB and -63.5 degrees respectively. The negative phase margin did not signify instability in this case, but that it was of smaller magnitude than phase margin in the other direction.
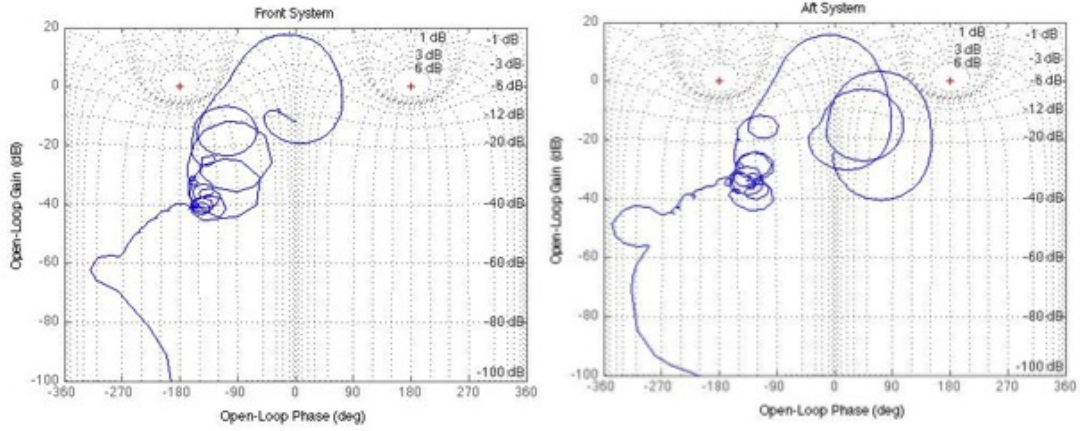
Figure 4.4:   Nichols Plots of 2-Mode SISO PPF Result

The experimental result of this controller is presented in Figure 4.5. A comparison of expected attenuation from simulation and actual results are presented in Table 4.2. The expected attenuation from simulation was the average of the attenuations achieved at each loop, which turned out to be very close in value as the experimental results.
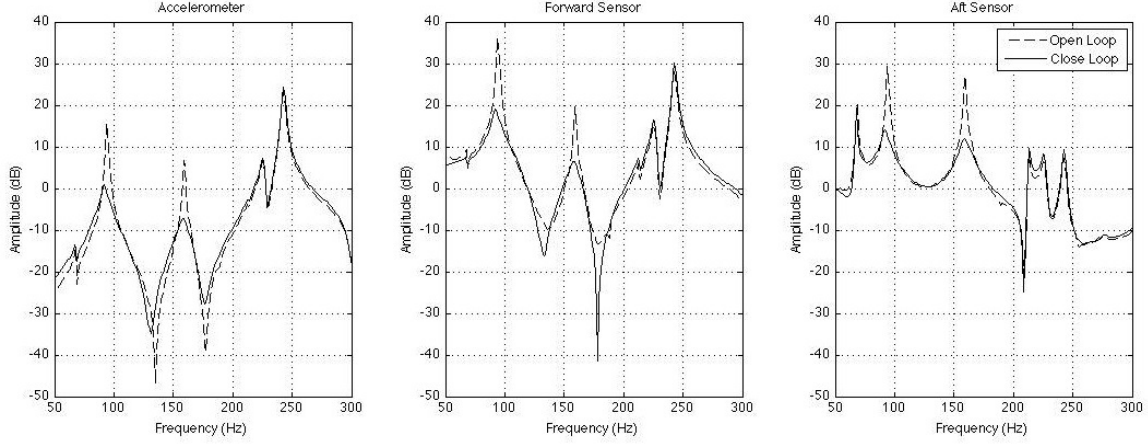
Figure 4.5:   2-Mode SISO PPF Result

Table 4.2:   Two Mode SISO PPF Attenuations

		Experiment (dB)		
Mode	**Simulation (dB)**	Accelerometer	Front Sensor	Aft Sensor
2nd (94.20 Hz)	17.96	16.14	18.15	16.37
3rd (159.14 Hz)	13.88	14.03	13.35	15.17

For the four-mode SISO PPF controller, the forward system targeted modes two and four and the aft system targeted modes one and three. The damping ratio was the same for all modes at 0.2 and the final gain values were the same for each mode for the system. Table 4.3 shows the design parameters for the four-mode controller.

Table 4.3:   Four Mode SISO PPF Design Parameters

System	**Frequency (ω_f)**	**Damping Ratio (ζ_f)**	**Gain (g_f)**
Front	94.20 / 212.59	0.2 / 0.2	0.04 / 0.04
Aft	68.35 / 159.14	0.2 / 0.2	0.063 / 0.063

The resulting controller produced a system with IGM and IPM of 12.1 dB and 22.0 degrees respectively. Even with the addition of controlling two extra modes with the same configuration, the IPM and IGM were not significantly affected. The single loop margins were 26.8 dB and 65.7 degrees for the front system and 33.7 dB and
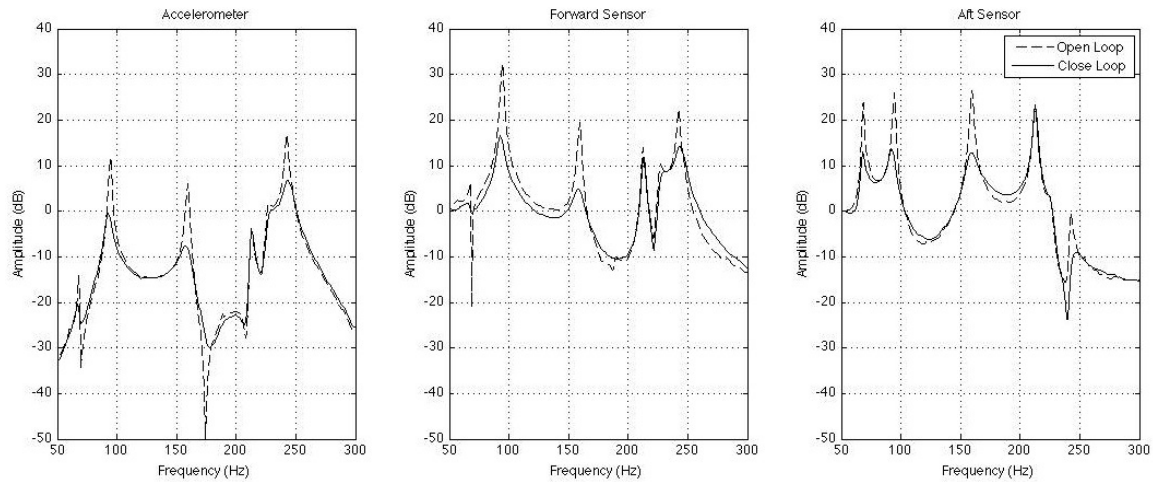
Figure 4.6:   4-Mode SISO PPF Result

Table 4.4:   Four Mode SISO PPF Attenuations

		Experiment (dB)		
Mode	Simulation (dB)	Accelerometer	Front Sensor	Aft Sensor
1st (68.35 Hz)	11.09	6.92	6.03	10.70
2nd (94.20 Hz)	16.24	13.30	16.81	13.90
3rd (159.14 Hz)	15.83	14.09	14.73	13.60
4th (212.59 Hz)	0.85	0.27	2.06	-0.12

83.1 degrees for the aft system and were also not significantly different from the two mode controller. The experimental result is presented in Figure 4.6 and Table 4.4.

As can be seen from the plots, certain modes such as mode one, showed different attenuation levels depending on the sensor location. The results, however, were all expected since the shape of the first mode concentrates the displacement in the aft section of the fin and the forward sensors would register minimal signals. This analysis led to also changing the location of the impact point for the impact hammer to an aft location to excite all the targeted modes. For all four mode controllers, this new aft impact location was used.

The results showed that the actuator patches, as installed, were effective for modes one, two, and three but not for four. A peculiar result was the effect of the mode four control spilling over to what would be modes five and six. There was a

significant level of attenuation at those modes rather than in mode four. This effect can be explained by the spillover effect noted by Browning [9] where if the modes were close in frequency, there is no way to avoid the control affecting those neighboring modes. The lack of attenuation in mode four cannot be explained by spillover effects but may be attributed to the patch configuration not being effective enough for that mode with one system.

4.3.2 Multivariable PPF.   As noted in Chapter III, the multivariable PPF controller development required the development of a first-order state-space model of the plant. This was attempted for both two and four target mode cases, but was only successful for the two target mode case. The algorithm used for the optimization process reduced the value of the cost function to below 0.5. In the four mode case, the best achievable was around 30 and the phase plot could not be matched. The four mode case was abandoned and the multivariable PPF was only developed for the two mode case. The resulting state space matrices for the two-mode case and the graphical comparison of the fit model and the reduced plant model can be found in Section A.2. The magnitude was a close match, especially in the target mode frequency region and the phase plot also matches with a slight discrepancy at higher frequencies, which did not affect the controller design process.

The final design parameters are listed in Table 4.5. The IGM and the IPM with the resulting controller were 10.2 dB and 20.2 degrees respectively. The Nichols plots of each open loop (Figure 4.7) showed margins greater than 20 dB and 53 degrees in all loops.

Table 4.5:   Two Mode Multivariable PPF Design Parameters

System	Frequency (ω_f)	Damping Ratio (ζ_f)	Gain (g_f)
Front	94.20	0.2	0.06
Aft	159.14	0.2	0.03

The attenuation that was achievable for the multivariable PPF was slightly better than the SISO PPF (3 dB) while maintaining similar stability margins. The
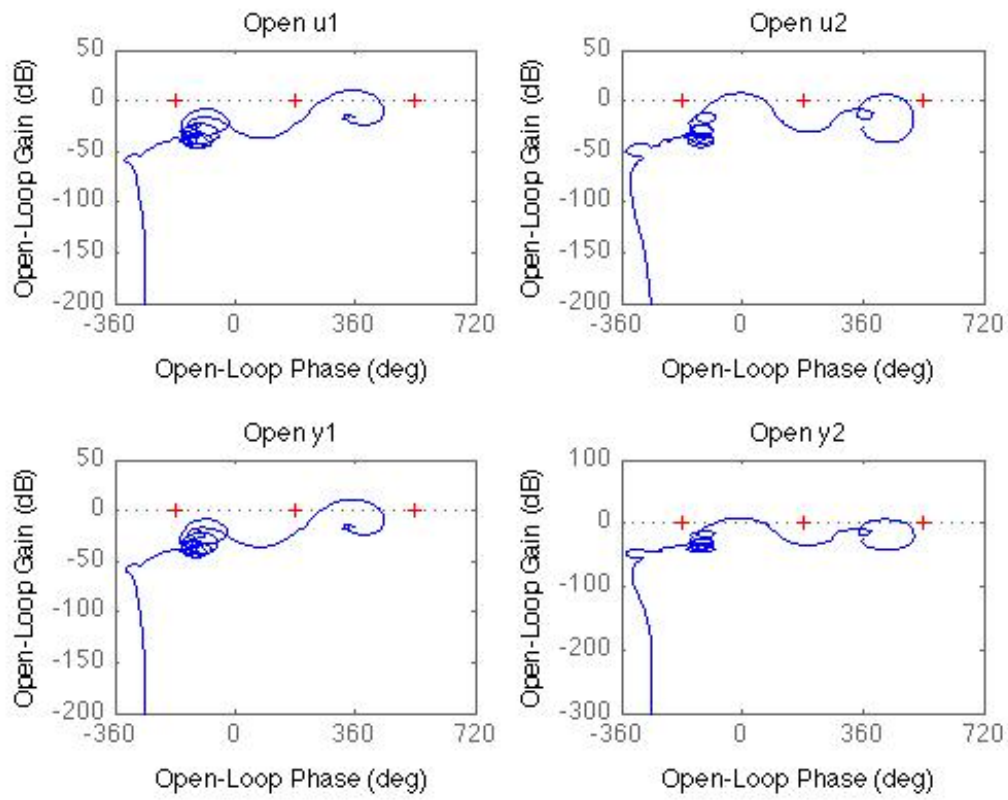
Figure 4.7:   Nichols Plots of Multivariable PPF Control

Bode magnitude plot of the attenuation results is presented in Figure 4.8 and the numerical results in Table 4.6.
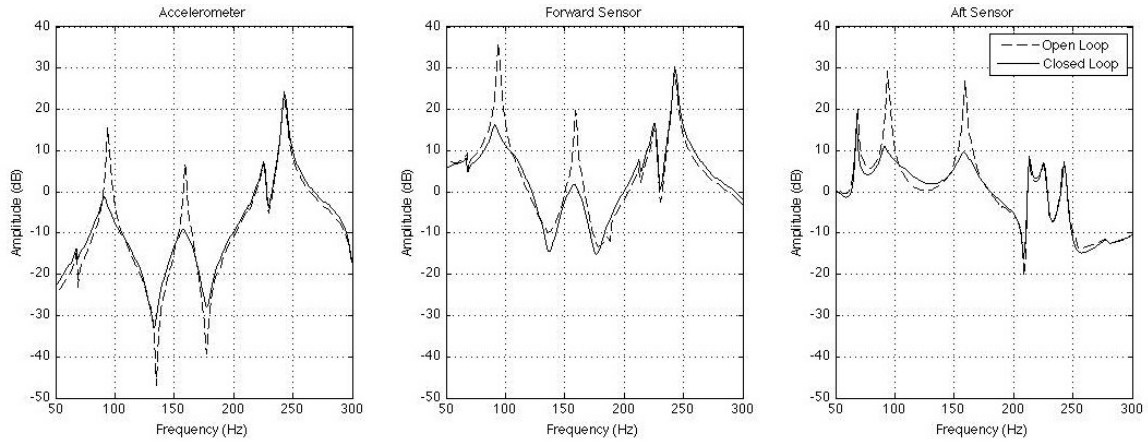
Figure 4.8:   Two Mode Multivariable PPF Result

Table 4.6:   Two Mode Multivariable PPF Attenuations

		Experiment (dB)		
Mode	Simulation (dB)	Accelerometer	Front Sensor	Aft Sensor
2nd (94.20 Hz)	20.07	18.79	21.47	19.29
3rd (159.14 Hz)	16.00	16.17	18.08	17.54

4.3.3 MIMO LQG.   The MIMO LQG design process was the most complex with numerous design parameters that had to be modified. To simplify the process and limit the scope of this research, only the sensor and input weighting matrices, $\mathbf{Q}$ and $\mathbf{R}$, were used as the design parameters. The rest of the design parameters were set to unity or identity matrices to best represent the unknown noise components of the plant system. Two configurations of the plant were tested with the MIMO LQG, the 2×2 and the 4×2 plant.

The MIMO LQG controller for the 2×2 plant produced a two-input two-output controller. The 2×2 plant model did not have any first-order modes in its state-space model so the first eight states corresponded to the first four modes. The two design

72

parameters **Q** and **R** are listed in table 4.7 for both the two mode and four mode controller.

Table 4.7:   2 × 2 LQG Design Parameters

Number of Modes	Sensor Weighting (Q)	Control Weighting (R)
Two Modes	$diag([0, 0, 1, 1, 1, 1, 0, 0, ..., 0])$	$diag([600, 1300])$
Four Modes	$diag([1, 1, 10, 10, 1, 1, 1, 1, 0, ..., 0])$	$diag([2500, 2100])$

The independent stability margins of the closed-loop systems were 20.9 dB and 27.1 degrees for the two-mode case, and 20.3 dB and 26.9 degrees for the four-mode case. In both cases the single loop margins were greater than 25 dB and 90 degrees. The reason the controller was not pushed further to decrease the IGM was due to the limit in actuator power (Section 4.4). The Nichols plot of the four mode 2 × 2 LQG system is presented in Figure 4.9.
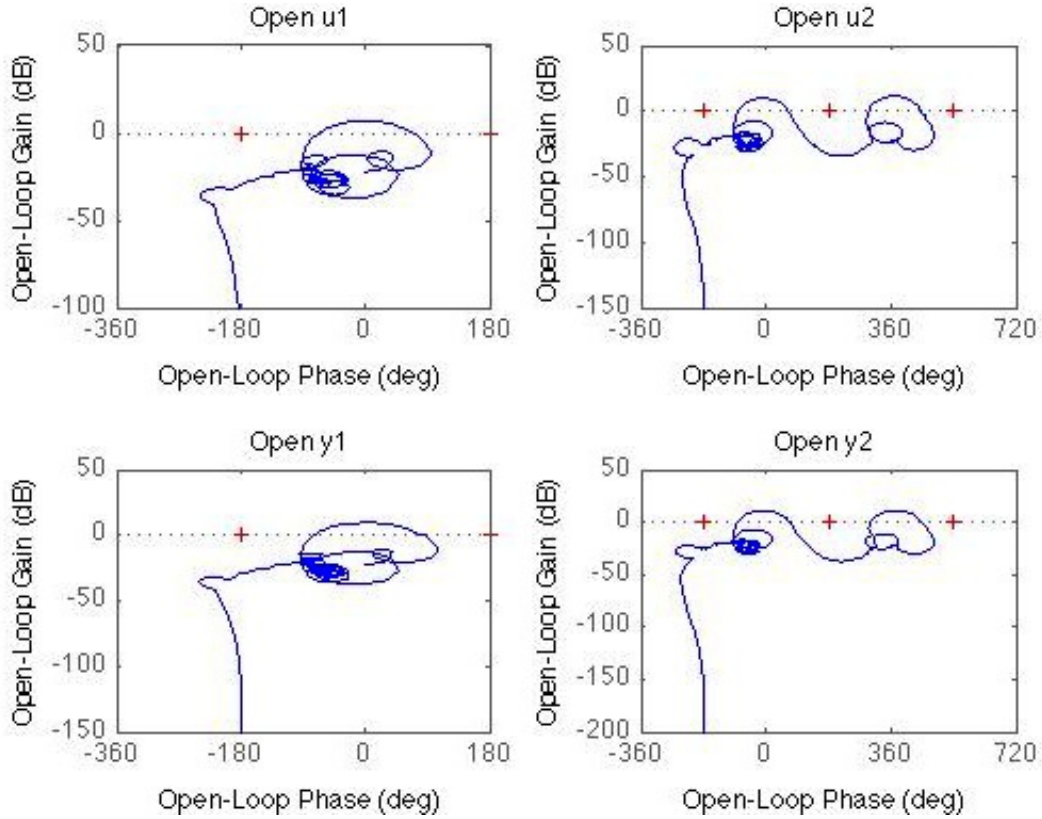
Figure 4.9:   Nichols Plots of 2 × 2 Four Mode LQG Control

The attenuation results of the 2×2 LQG controller closely resembled the performance by the multivariable PPF rather than the SISO PPF. Compared to the multivariable PPF, the two mode controller attenuated both modes more evenly while the multivariable PPF attenuated the second mode more than the third mode. This result was in part due to the selected design parameters, but during the design process, it was easier to find the parameters necessary for an even distribution of energy using an LQG algorithm than either of the PPF's. The Bode magnitude plots of the two mode case is presented in Figure 4.10 and the four mode case is presented in Figure 4.11. Numerical results are presented in Tables 4.8 and 4.9 respectively. Control of mode one was much more effective with the LQG controller than the SISO PPF. Mode four also saw positive attenuations and there was no spillover into the higher modes as was seen in the SISO PPF control.
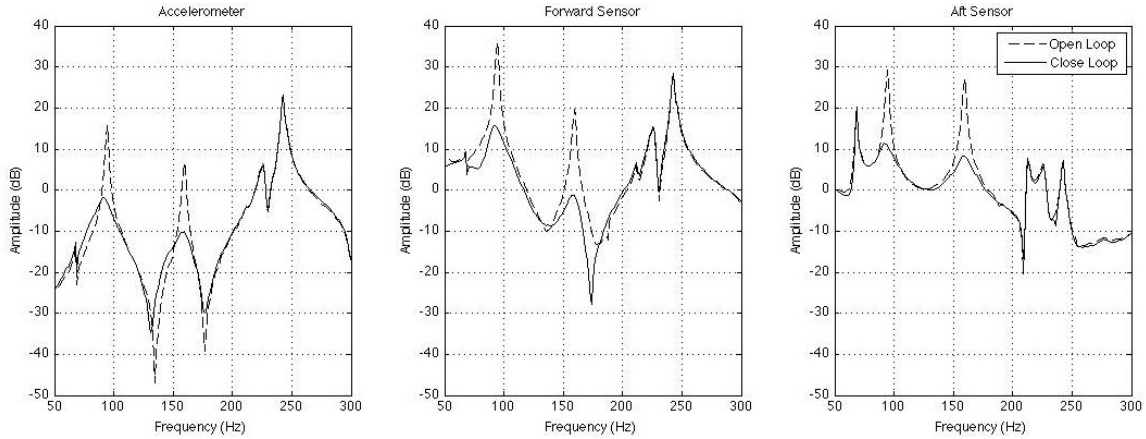
Figure 4.10: 2×2 Two Mode LQG Result
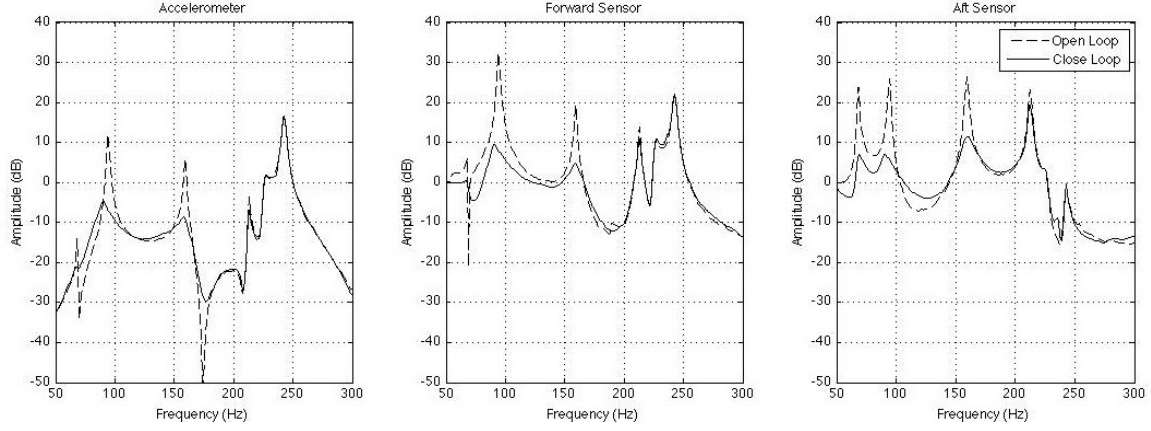
Figure 4.11:   2 × 2 Four Mode LQG Result

Table 4.8:   2 × 2 Two Mode LQG Attenuations

		Experiment (dB)		
Mode	**Simulation (dB)**	Accelerometer	Front Sensor	Aft Sensor
2nd (94.20 Hz)	18.85	18.35	20.90	18.40
3rd (159.14 Hz)	17.05	17.09	21.11	18.80

Table 4.9:   2 × 2 Four Mode LQG Attenuations

		Experiment (dB)		
Mode	**Simulation (dB)**	Accelerometer	Front Sensor	Aft Sensor
1st (68.35 Hz)	8.77	7.04	6.45	17.13
2nd (94.20 Hz)	21.11	18.48	24.27	20.03
3rd (159.14 Hz)	15.32	14.96	14.61	14.93
4th (212.59 Hz)	3.04	3.21	3.12	3.85

The second plant configuration, the 4 × 2 plant, resulted in a two-input four-output (2 × 4) controller. The four independent actuators added two more elements in the **R** value increasing the number of design parameters. The design parameters that were settled on are presented in Table 4.10. The 4 × 2 plant state space model included two first order modes at lower frequencies which moved the design parameter states to start from the third element and on.

Table 4.10: 2×4 LQG Design Parameters

# of Modes	Sensor Weighting (Q)	Control Weighting (R)
Two Modes	$diag([0, 0, 0, 0, 5, 5, 1, 1, 0, ..., 0])$	$diag([250, 600, 300, 700])$
Four Modes	$diag([0, 0, 1, 1, 10, 10, 1, 1, 1, 1, 0, ..., 0])$	$diag([600, 1800, 800, 1700])$

The resulting IGM and IPM of the two controllers were 9.4 dB and 19.3 degrees for both cases. The single-loop margins were not looked at for the 2×4 controller due to the complexity of the system. The Bode magnitude plots of the two mode case is presented in Figure 4.12 and the four mode case is presented in Figure 4.13. Numerical results are presented in Tables 4.11 and 4.12 respectively.
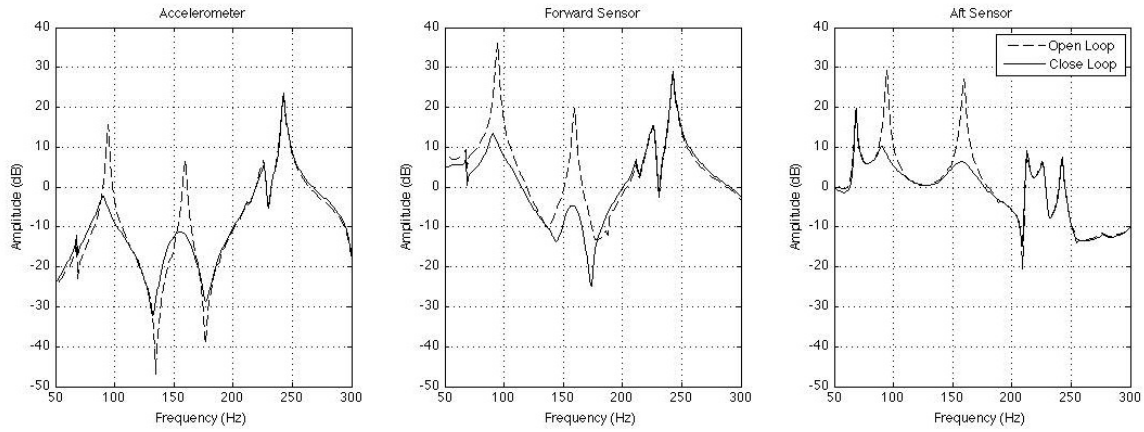
Figure 4.12: 2×4 Two Mode LQG Result
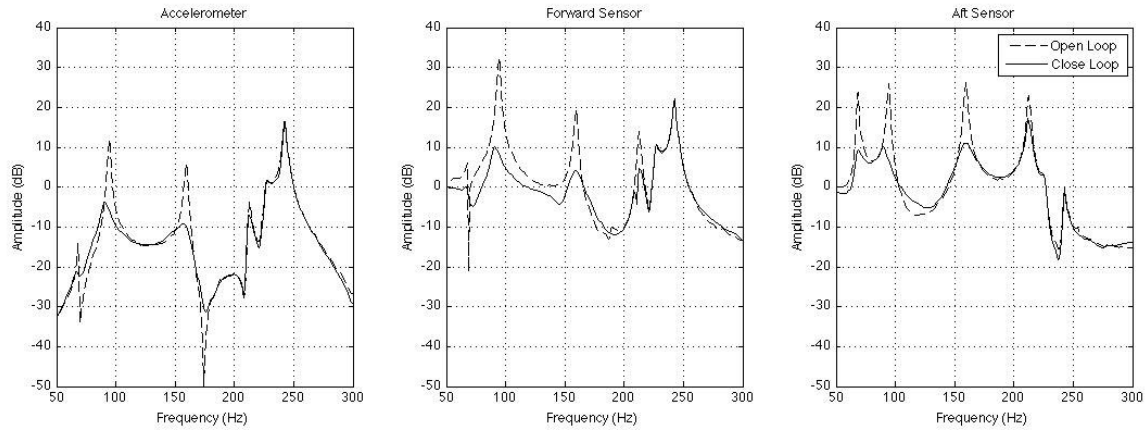
Figure 4.13: 2×4 Four Mode LQG Result

76

Table 4.11:   2 × 4 Two Mode LQG Attenuations

		Experiment (dB)		
Mode	**Simulation (dB)**	Accelerometer	Front Sensor	Aft Sensor
2nd (94.20 Hz)	20.94	20.51	24.81	21.04
3rd (159.14 Hz)	18.67	18.60	24.55	20.82

Table 4.12:   2 × 4 Four Mode LQG Attenuations

		Experiment (dB)		
Mode	**Simulation (dB)**	Accelerometer	Front Sensor	Aft Sensor
1st (68.35 Hz)	11.07	7.41	6.99	14.57
2nd (94.20 Hz)	20.50	17.73	23.94	18.88
3rd (159.14 Hz)	16.06	15.74	15.38	15.26
4th (212.59 Hz)	4.92	3.22	9.14	6.79

The 2×4 LQG controller performed slightly better than the 2×2 LQG controller. In the two mode case, the mode two attenuations were about equal in all three sensors for the 2 × 4 controller, which shows that this controller is capable of controlling the dynamics of mode two better and attenuates the entire fin rather than a specific section. Mode three showed similar results as the 2 × 2 LQG controller and favored the front section of the fin more than the aft. In the four mode case, the opposite was seen where mode three was more evenly controlled than the mode two.

4.4   Control Power Requirements

Despite what controller is used, the limit of power has to be considered. This limitation will saturate the actuators causing non-linearities and possibly lead to instability. In Section 3.6 the actuator voltage was limited to 700 volts peak. The only way to test each algorithm for this limit was in simulation using the sensor signals obtained from ACTIVE FIN. Figure 4.14 is the simulation result of the 2 × 4 LQG controller sensor measurement from ACTIVE FIN flight test at 0.95 Mach and 7,500 feet pressure altitude. Browning conducted a similar simulation after the fact and determined that his controller required up to 1900 volts of actuator power. It can be
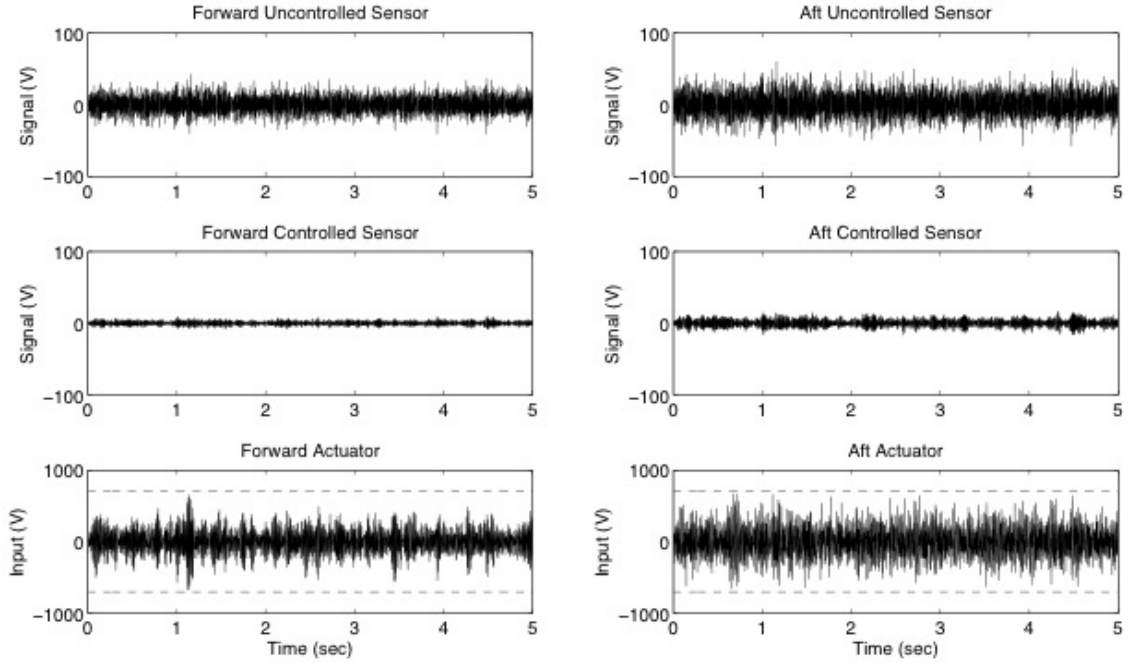
Figure 4.14: Simulation Result Using ACTIVE FIN 7,500 feet, 0.95 Mach [9] and a 2×2 Four Mode Controller

seen in this case that the controls did not saturate and the controlled sensor signals were significantly smaller than the uncontrolled sensor signals.

The simulation was run using SIMULINK$^®$ and the peak control voltage as well as the root mean square (RMS) of the control signal were determined. For all algorithms the peak actuator voltage ranged from 606 to 690 volts and the RMS ranged from 144 to 180 volts. Table 4.13 shows the results for all the two mode control algorithms and Table 4.14 shows the result for the four mode controls.

Table 4.13: Actuator Power Simulation Results - Two Mode

Control	Peak Voltage ($u_1/u_2/u_3/u_4$)	RMS Voltage ($u_1/u_2/u_3/u_4$)
SISO PPF	690.0/668.7/690.0/668.7	179.3/167.5/179.3/167.5
Multivariable	606.3/656.8/606.3/656.8	144.6/169.5/144.6/169.5
2×2 LQG	622.8/652.9/622.8/652.9	173.3/154.6/173.3/154.6
2×4 LQG	633.1/684.6/648.6/653.3	177.3/172.5/180.7/162.1

Table 4.14:   Actuator Power Simulation Results - Four Mode

Control	Peak Voltage ($u_1/u_2/u_3/u_4$)	RMS Voltage ($u_1/u_2/u_3/u_4$)
SISO PPF	663.6/648.0/663.6/648.0	175.4/160.9/175.4/160.9
2×2 LQG	672.5/673.1/672.5/673.1	161.3/200.6/161.3/200.6
2×4 LQG	674.5/640.5/626.2/625.3	175.6/173.5/164.8/174.0

All controllers achieved the actuator power requirement of less than ± 700 volts. There were several controllers such as the multivariable PPF and the two mode LQGs that still had some margin in actuator power that could be harnessed for possibly more attenuation.

4.5   Robustness Analysis

All the controllers presented so far met the criteria required for flight test. It was mentioned previously that the ventral fin dynamics may change when mounted on the aircraft instead of the laboratory table. To test the controller's performance in situations where the plant system is different from the one used in design, the controller was implemented on a modified ventral fin. The mass that was added to the ventral fin successfully shifted modes one and two of the fin by 7 and 5 Hz respectively.

Table 4.15 shows the frequency shifts at each mode for the modified fin, Table 4.16 shows the attenuation results at the new modal frequencies for the two mode controllers, and Table 4.17 shows the attenuation results for the four mode controllers. All tested controllers showed effective reductions in vibrations even with the shifted modes.

Table 4.15:   Modal Frequency Shift Results

Mode	Original (Hz)	New (Hz)	Change (Hz)
1st	68	61	7
2nd	94	89	5
3rd	159	157	2
4th	213	211	2

Table 4.16: Attenuations for the Modified Fin (dB) - Two Mode

Mode	SISO PPF	Multi PPF	2×2 **LQG**	2×4 **LQG**
2nd	8.24	11.93	13.08	13.58
3rd	12.48	15.28	16.38	17.65

Table 4.17: Attenuations for the Modified Fin - Four Mode

Mode	SISO PPF (dB)	2×2 **LQG** (dB)	2×4 **LQG** (dB)
1st	6.85	10.00	9.63
2nd	10.14	17.38	15.13
3rd	12.64	13.25	14.39
4th	1.12	2.64	5.87

4.6   Digital Controller

Test were conducted to determine how large of a sampling frequency the controller can run at with the selected control algorithms. The larger the sampling frequency, the smaller the delay, which allowed for better phase margin. A preliminary design of the program for the MABXII contained all four control algorithms in one. The MABXII processor could not sustain the programming at 40 kHz. With the same programming, the best sampling frequency was at 25 kHz where the computer did not experience any problems. Each control algorithm was then tested individually, meaning that each programming had one control algorithm. This allowed all controllers to run at 40 kHz without encountering any overrun problems. The three PPF algorithms were then tested in one programming and the MABXII again ran at 40 kHz without any issues. It is recommended for flight test to organize the test algorithms to allow for running the PPF controllers in one programming and the individual LQG controller on their own programs.

4.7   Custom Amplifier Testing

The custom amplifier was tested in the prototype condition before all the components were placed in its housing. The amplifier was a class D switching amplifier that took in analog signals from the control computer. The analog signal was pro-

cessed through an ADC and converted into pulse-width modulated (PWM) signal using a microprocessor. Four microprocessor boards were made, one for each actuator section. Two PWM signals were outputted from the processor boards, one controlling the high side amplifier and the other controlling the low side amplifier. The duty cycle of the PWM signals and the difference between the high and the low side controlled the high voltage output. During the design process of the amplifier, a high voltage filter was added after the amplification to reduce the high frequency noise. Another major design parameter in the amplifier related to noise and phase delay was the dead time between the high and low side. It was apparent that the lowpass filter was not enough to reduce the noise, and the dead time was adjusted to attempt to remove it [20]. The final design dead time was set at 1.6 microseconds which significantly reduced the noise while avoiding overlap of the high side and the low side.
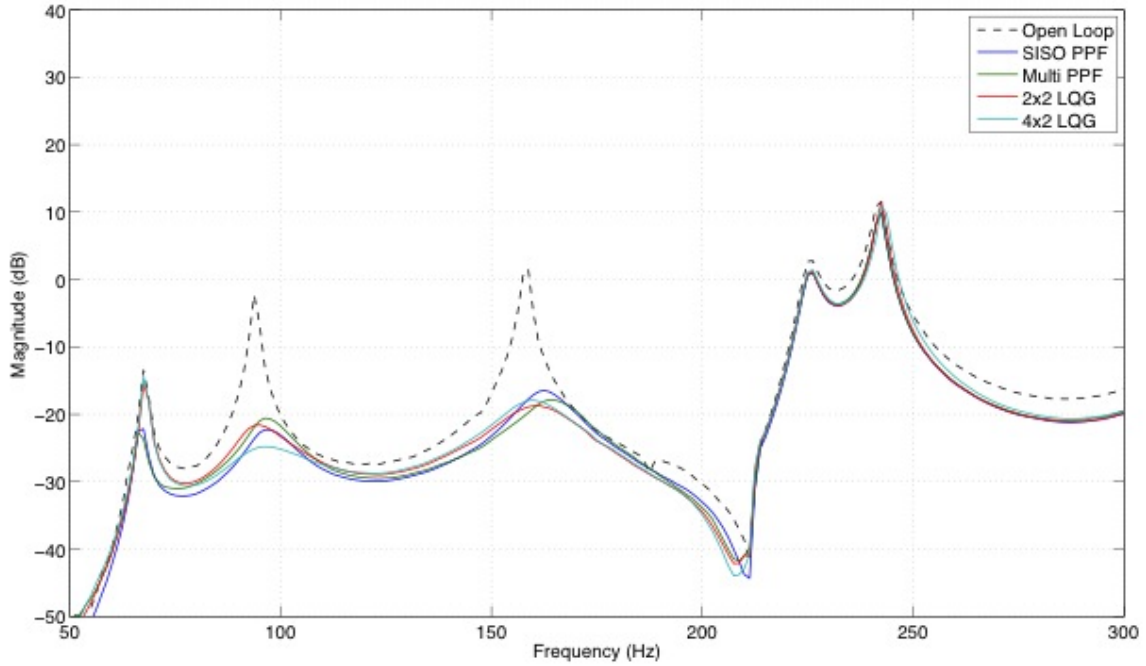
Figure 4.15:   Accelerometer Results of All Two Mode Controllers with Custom Amplifier

The resulting amplifier had a bandwidth of around 1200 Hz but the phase started to roll off immediately at low frequencies and hit -24 degrees by 210 Hz. This was in contrast to the linear Trek amplifier which did not have any phase rolloff. The delay was fairly large and was a concern at first, but stable control algorithms were still possible. Due to limited time available with the custom amplifier, cursory designs of the controllers were accomplished to prove that the system with the amplifier could attenuate the modes. Figure 4.15 shows the results of those controllers. The controllers were successful in attenuating the modes while maintaining stability.

Several concerns were noted during the testing. The first was when the plant model was compared to those of the laboratory amplifier model. Figure A.11 and A.12 shows the comparisons of the two models. Figure A.11 shows all Bode plots with a 180 degree phase difference at zero frequency. Looking at Figure A.12 it can be seen that the starting phases are clearly 180 degrees off in the the In(1) to Out(1) and In(2) to Out(2) Bode plots. Since the ERA process produces estimation errors in the lower frequencies due to the higher noise, the FRFs were analyzed. The analysis resulted in the DC phases for the 4x2 plants as shown in Table 4.18. The

Table 4.18:   DC Phase Comparisons of the 4×2 Plant FRF

Sensor	Lab Amp Actuator				Custom Amp Actuator			
	In(1)	In(2)	In(3)	In(4)	In(1)	In(2)	In(3)	In(4)
Out(1)	-172°	n/a	169°	n/a	-35°	n/a	162°	n/a
Out(2)	n/a	-20°	n/a	0°	n/a	-23°	n/a	162°

table shows that the actuators may have been wired differently with the laboratory amplifier than with the custom amplifier. The importance of consistent wiring became apparent since a significant difference in system dynamics are observed due to the differences in DC phase. With the current setup using the inboard sensor as the control measurement, when the inboard actuator sees a positive input, the sensor stretches in the same direction and should output a positive signal. This would mean that the phase should be near zero at low frequencies. When the outboard actuator is excited, a positive signal to the actuator would compress the inboard sensor and

the sensor should output a negative signal. This would result in a DC phase of 180 degrees. From Table 4.18 it can be seen that actuator one and four in the laboratory amplifier setup may have been wired backwards. Despite the discrepancies in wiring, both amplifiers effectively attenuated the vibrations. This is because the control design methods were applied independently to the two setups and the differences in dynamics were taken into account in the models produced by ERA, and hence the controllers. This shows that the design methods used during this research is effective if started from characterizing the plant. It is recommended to analyze the plant model before moving on to the controller design to ensure the wiring is correct and the plant model shows the expected dynamics, this will ensure full effectiveness of the actuator configuration.

The second concern that was noted during the testing was that with enough input force from the impact hammer, the sensor measurements would saturate and cause the system to go unstable. When the system became unstable, the controller would send out maximum control inputs and hit the actuator saturation values that were programmed. For all PPF cases, the instability caused a limit cycle oscillation (LCO) and continued until the controller was turned off. The LQG controllers, however, were able to recover itself and did not control the fin into an oscillation. The latter reaction was present during laboratory testing with the Trek amplifier but because of its self-recovery characteristics, it was never a concern. The sensor saturation can be mitigated by adding the previously proposed charge attenuator but further analysis should be made on the LCO susceptibility/non-susceptibility of the controllers when encountering saturation.

Further analysis was accomplished using MATLAB® and simulations after the custom amplifier was no longer available. Analysis was conducted on the new plant model using controllers with the exact same design parameters as those tested with the lab amplifier (different from 4.15 values). Minor differences included the different elements for the state weighting matrices and the the multivariable PPF reduced model fit. In all controllers, the smallest loop gain margin decreased with the custom

Table 4.19:　Simulation Comparison of Laboratory Amplifier to Custom Amplifier

Controller	Percent Difference*			
	SISO PPF	**MPPF**	**2x2 LQG**	**2x4 LQG**
Min Loop GM	-45%	-15%	-61%	
Min Loop PM	34%	6%	-7%	
IGM	19%	9%	-68%	28%
IPM	8%	5%	-42%	14%
Mode 2	6%	7%	8%	-6%
Mode 3	-10%	12%	5%	-17%
Amp 1, 3 Power	-86%, -86%	-9%,-9%	182%, 182%	121%, 152%
Amp 2, 4 Power	24%, 24%	193%, 193%	48%, 48%	-0.1%, 6%

Percent Difference = 100%(custom-lab)/lab

amplifier. The loop phase margin increased for the PPF controllers but decreased for the LQG controllers. The IGM increased for all controllers but decreased for the both 2×2 LQG controllers. The same was seen for the IPM. Attenuations were mixed with some modes increasing while others decreasing and did not seem to depend on the type of the controller. The critical difference was in the power consumption. The amount of power required to run the controllers were very different. Some actuators required up to 193% more power while another actuator required 86% less power. This result further emphasizes the necessity to go through the controller design process to optimize the controls for the actual plant system they will be used on. Especially in this case where it was noted that the laboratory amplifier setup may have been wired differently and the plant models were significantly different in some places. Table 4.19 summarizes the percent difference between the laboratory amplifier setup and the custom amplifier setup for the two mode controllers.

V. Summary and Conclusions

The overall objective of this research was to improve on the vibration control system used in the ACTIVE FIN to attempt another flight test. Improvement of the design entailed the addition of signal conditioning devices, increasing actuation power, and using MIMO control algorithms to more efficiently attenuate the vibrations. This chapter summarizes the results of the testing in this research and provides recommendations for future testing and research.

5.1 Summary

The newly obtained ventral fin was identified as a different version compared to the ventral fin used in ACTIVE FIN. Both the modal analysis by accelerometers and mode shape comparison using the LDV showed that the fin dynamics at lower frequencies were clearly different. Since the new fin was identified to be the same as the FEM analysis conducted by Morgenstern, the piezo actuator patches were installed the way he proposed from his FEM analysis. The principal strain directions determined experimentally also matched the FEM analysis. Modes two and three were the primary targets for the installed actuators.

A graphic summary of results from the accelerometer for the two mode controller is shown in Figure 5.1 and the four mode control is shown in Figure 5.2. Figure 5.3 shows the results of the robustness test. Table 5.1 shows the attenuations at the accelerometer, independent margins and the power usage results of all the two mode controllers. Table 5.2 shows the same results for all the four mode controllers.

Each two mode controller showed effective attenuations at modes two and three without any spillover effects. This showed that the installed actuator patches were indeed effective in attenuating the modes that they specifically targeted. With the four mode controllers, two extra modes, one and four, were also targeted while still using the actuators that were installed optimally for the other two modes. The controllers showed some attenuation at mode one but not much in mode four. For the SISO PPF controller, mode four was not affected at all and the attenuations were seen in modes five and six.

The 2x2 LQG controller was able to achieve the highest independent gain and phase margins for both two and four mode cases while keeping the actuator power requirements below ± 700 volts. With the sacrifice of the independent gain and phase margins, the 2x4 LQG was able to achieve the largest attenuations while staying within the maximum voltage limits. The SISO PPF were the simplest controllers to design but were not as effective and were susceptible to affecting modes that were not targeted. All controllers, however, met the requirements set forth at the beginning of this research and are viable candidates for future testing in flight.

During the robustness test, all the controllers were able to attenuate the shifted modes but at a lesser magnitude during the test with the modified ventral fin. The LQG was the most robust and had the best attenuations during this test. Despite the smaller attenuations, the controllers were proven to be effective with minor shifts in modal frequencies. As can be seen from the results, since the controllers were not designed for the new plant, their effectiveness was lower. During fight test, to ensure the best results can be realized, it is recommended that the control algorithms be modified to meet the actual plant system that ensues once the fin is installed on the aircraft.

Finally testing with the custom amplifier showed that attenuation was possible with the controllers that were developed using the design process. Due to additional phase lag in the custom amplifier, using the same design parameters as those used in the laboratory amplifier setup did not produce the same performance or stability margins.

Table 5.1:   Summary of Results for Two Mode Controllers

Control	Mode 2	Mode 3	IGM	IPM	Max Voltage
SISO PPF	16.1 dB	14.0 dB	11.5 dB	21.5°	690, 669, 690, 669
Multi PPF	18.8 dB	16.1 dB	10.2 dB	20.2°	606, 657, 606, 657
2x2 LQG	18.4 dB	17.1 dB	20.9 dB	27.1°	623, 653, 623, 653
4x2 LQG	20.5 dB	18.6 dB	9.4 dB	19.2°	633, 685, 649, 653

Table 5.2:   Summary of Results for Four Mode Controllers

Control	Mode 1	Mode 2	Mode 3	Mode 4	IGM	IPM	Max Voltage
SISO PPF	6.9 dB	13.3 dB	14.1 dB	0.3 dB	12.1 dB	22.0°	664, 648, 664, 648
2x2 LQG	7.0 dB	18.5 dB	15.0 dB	3.2 dB	20.3 dB	26.9°	673, 673, 673, 673
4x2 LQG	7.4 dB	17.7 dB	15.7 dB	3.2 dB	9.4 dB	19.3°	674, 641, 626, 625
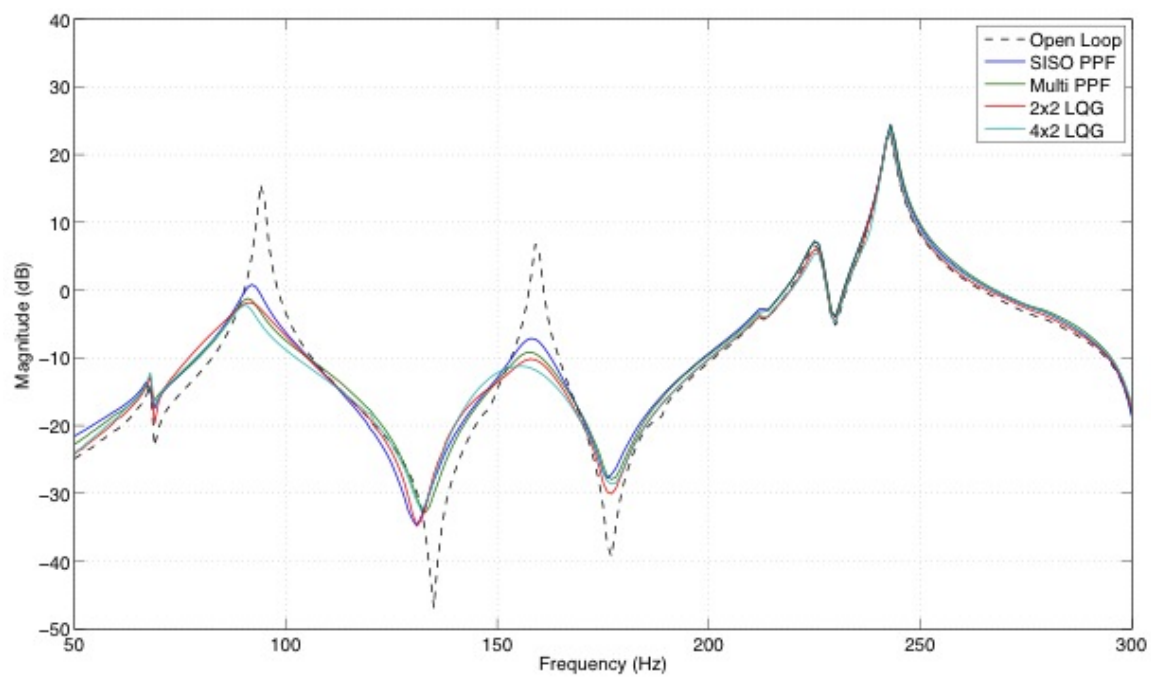
Figure 5.1:   Accelerometer Results of All Two Mode Controllers
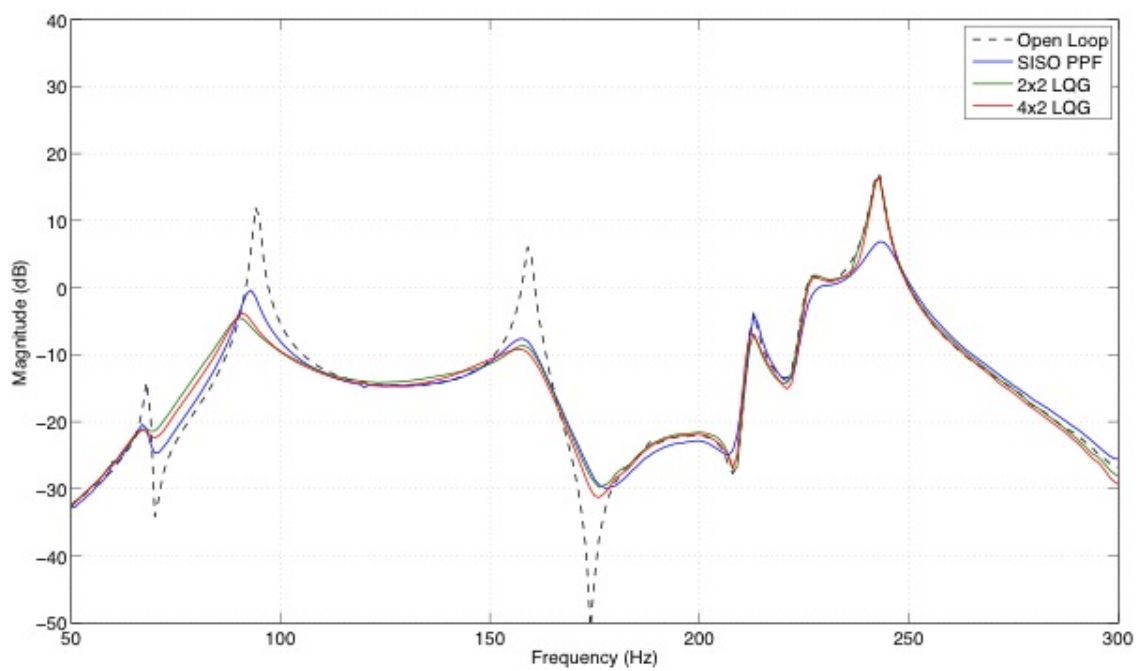
Figure 5.2:   Accelerometer Results of All Four Mode Controllers
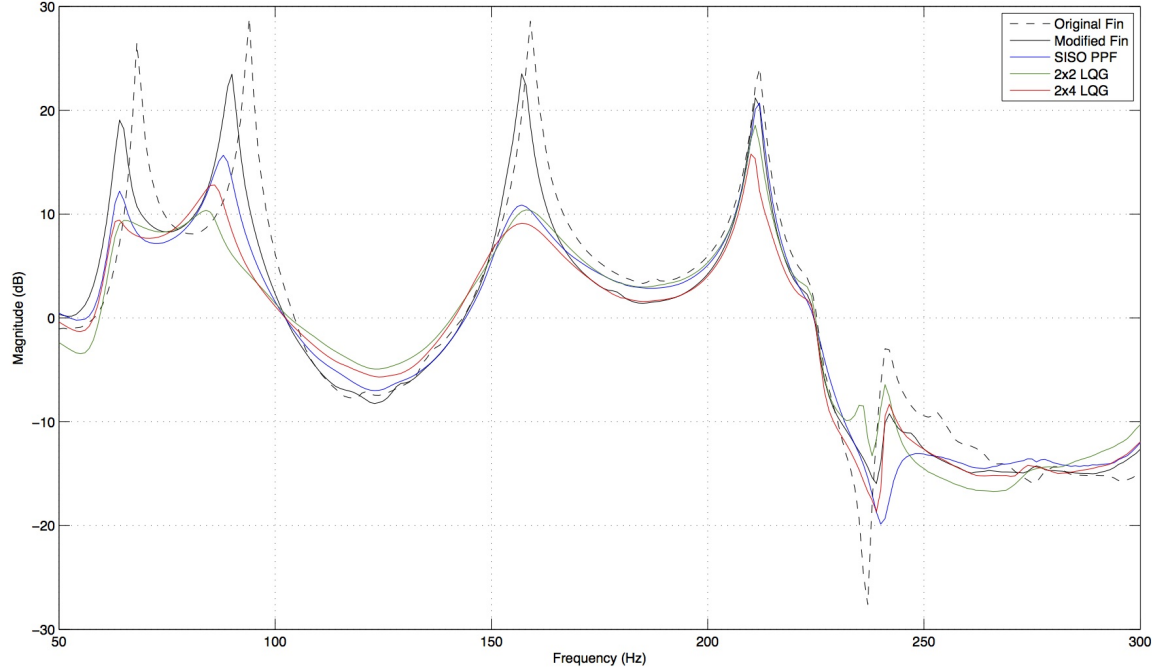
Figure 5.3:   Robustness Test for Four Mode Controllers

5.2 Recommendations

The following recommendations were developed during this research as a guide for the upcoming flight test as well as future research.

5.2.1 Flight Test Recommendations.

1. Use 20:1 charge attenuators between the piezo sensor and the charge converter to capture the full range of sensor signals, and to avoid non-linear effects caused by saturation.

2. Characterize the plant system once the fin is installed on the aircraft and tune the controllers to meet the changes.

3. Analyze the plant model before controller design to ensure the wiring is correct and the plant model shows the expected dynamics.

4. Run the PPF algorithms separate from LQG algorithms in flight to maintain 40 kHz MABXII sampling frequency to avoid overloading the computer.

5.2.2 Research Recommendations.

1. Investigate the effects of the input disturbance, measurement noise, and fictitious noise spectral density during the Kalman filter design process for the LQG controller.

2. Investigate LCO susceptibility/non-susceptibility of the controllers when encountering saturation or other non-linear conditions.

3. Investigate the application of adaptive control to improve robustness and counteract changes in the plant system due to unpredictable aerodynamic loads and aircraft structural changes.

4. Investigate the benefits or drawback of additional actuators or sensors to target more modes effectively.

5. Re-evaluate the target modes to be controlled by the current actuator setup.

Appendix A. Experimental Results

The following sections are the full results of the tests conducted during this research.

A.1 Plant Bode Plots
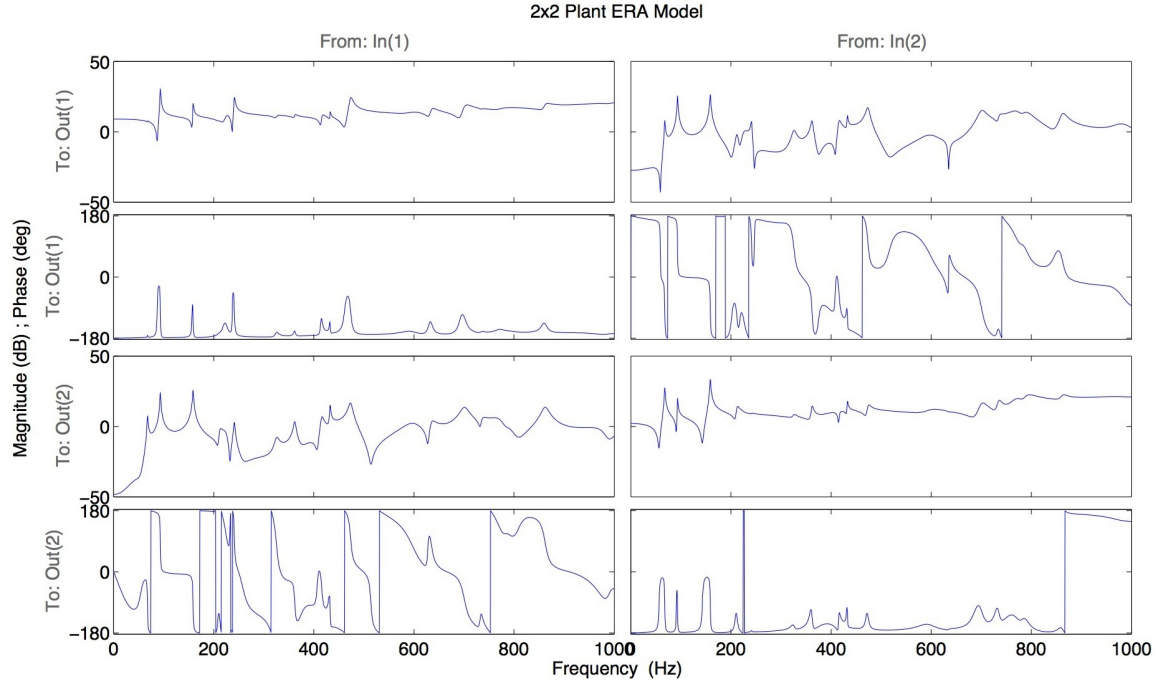
Figure A.1: 2×2 Plant ERA Bode Plot
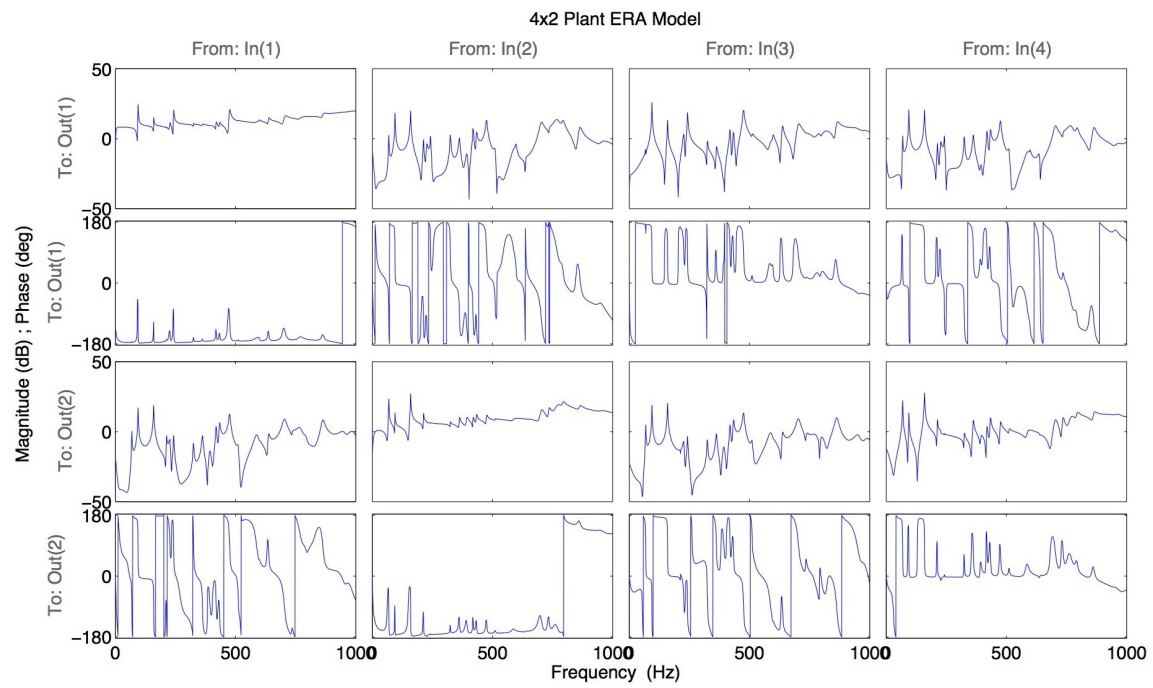
Figure A.2: 4×2 Plant ERA Bode Plot

A.2 Multivariable PPF Reduced Model Fit State Space Equation

$$
A = \begin{bmatrix} 0 & 1 & 0 & 0 \\ -(586.57^2) & -2(586.57)(0.006) & 0 & 0 \\ 0 & 0 & 0 & 1 \\ 0 & 0 & -(997.08^2) & -2(997.08)(0.005) \end{bmatrix}
$$

$$
B = \begin{bmatrix} 0 & 0 \\ 59773 & -32611 \\ 0 & 0 \\ 5.901 & 14.133 \end{bmatrix}
\qquad\qquad (\text{A}.1)
$$

$$
C = \begin{bmatrix} 2.4786 & 0 & 14621 & 0 \\ -1.219 & 0 & 33706 & 0 \end{bmatrix}
$$

$$
D = \begin{bmatrix} 0 & 0 \\ 0 & 0 \end{bmatrix}
$$
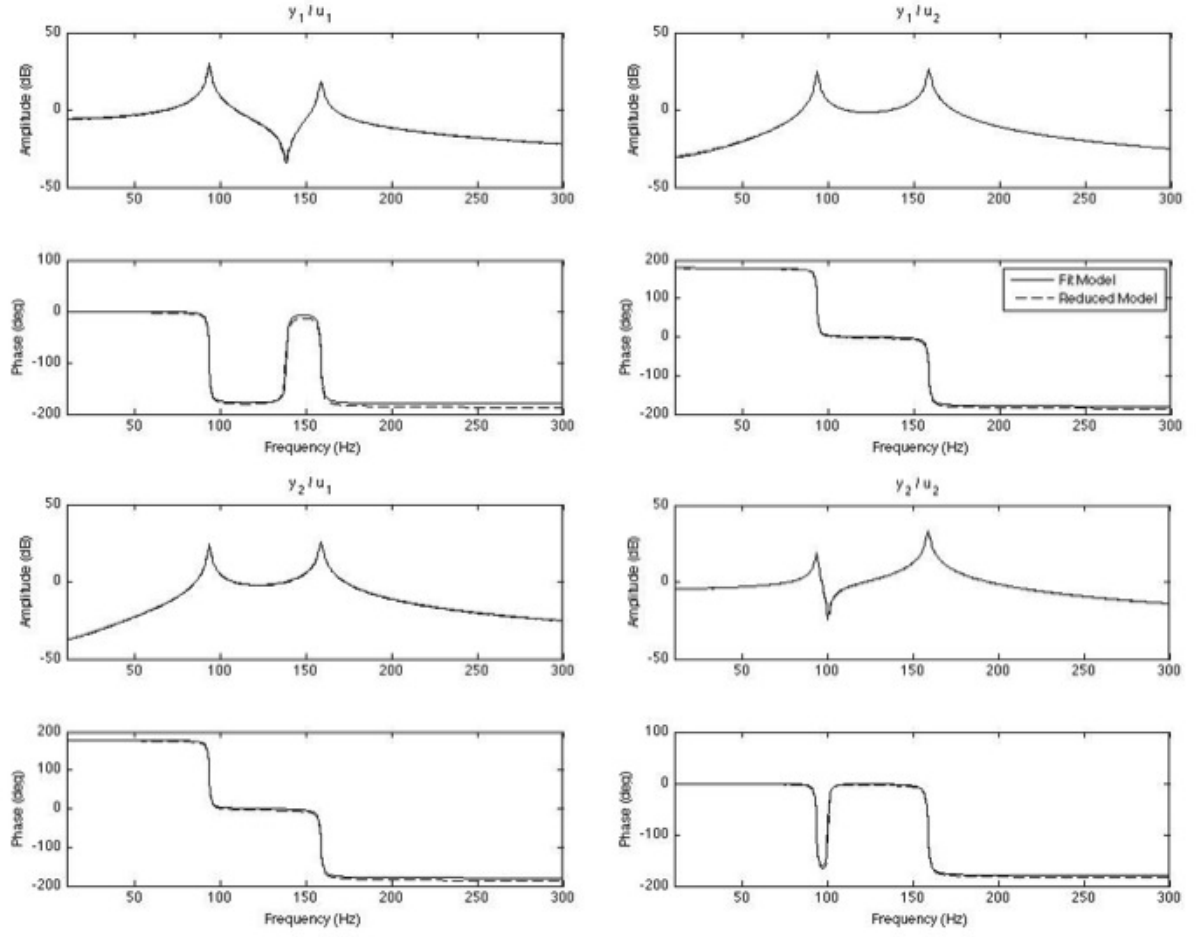
Figure A.3:   Two Mode Fit Model

A.3 Controller Bode Plots
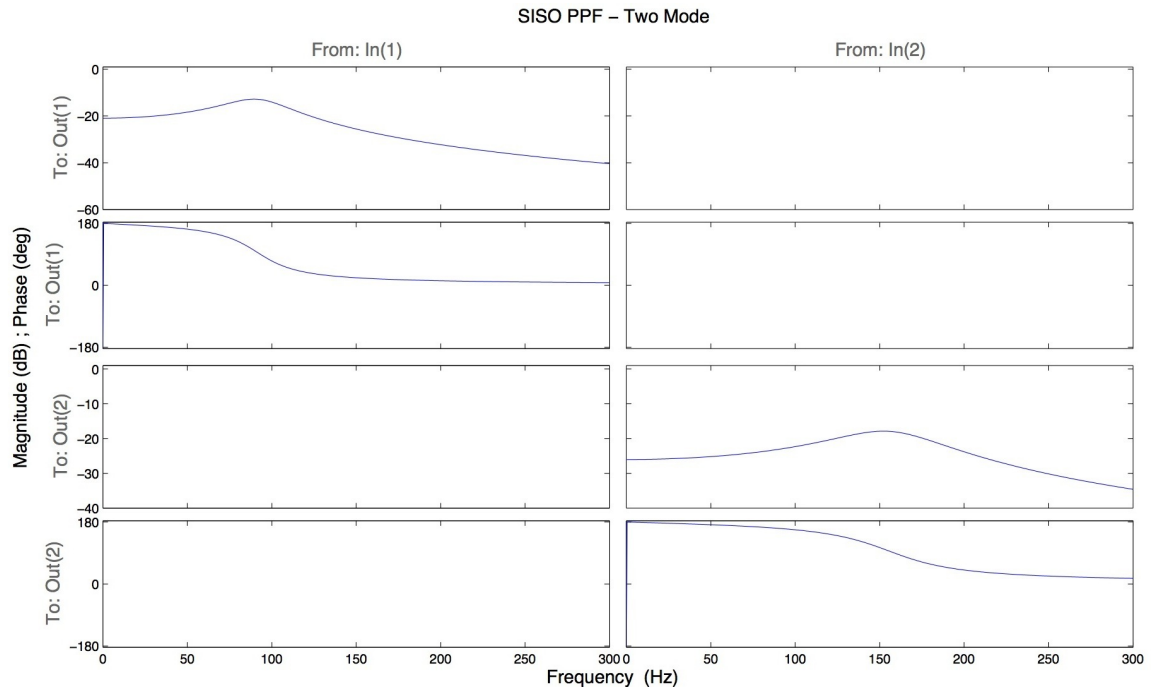
Figure A.4:   SISO PPF - Two Mode Bode Plot
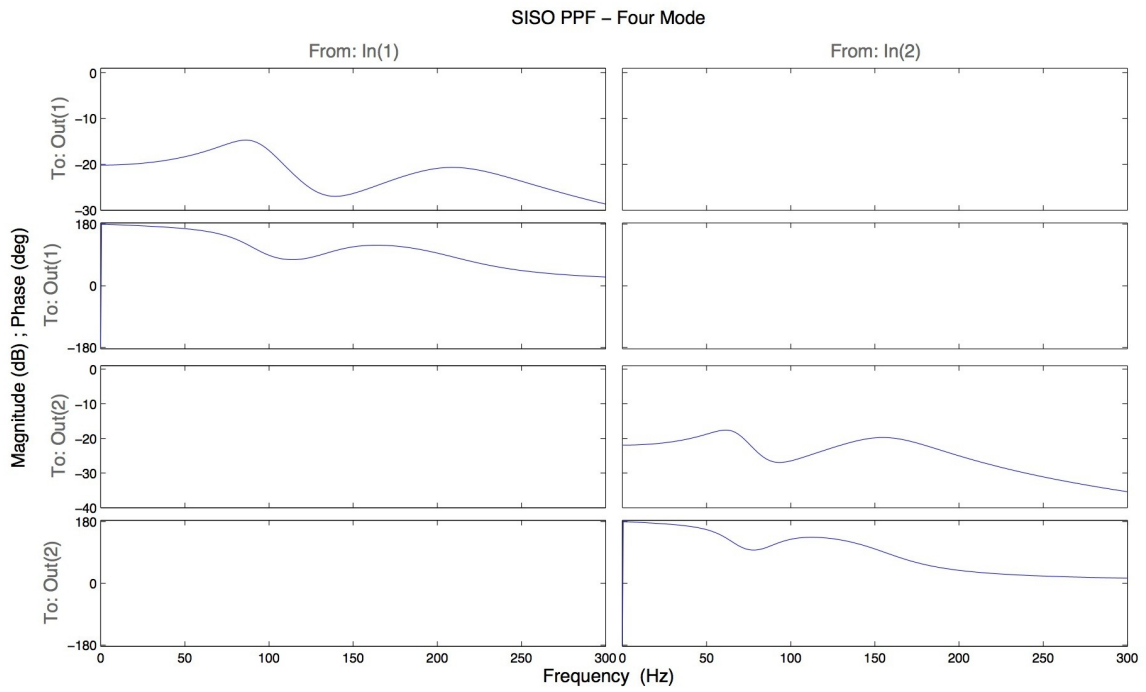
Figure A.5:   SISO PPF - Four Mode Bode Plot

Multivariable PPF

Figure A.6:   Multivariable PPF Bode Plot

2x2 LQG – Two Mode

Figure A.7: 2×2 LQG - Two Mode Bode Plot

Figure A.8: 2×2 LQG - Four Mode Bode Plot

Figure A.9: 2×4 LQG - Two Mode Bode Plot

Figure A.10: 2×4 LQG - Four Mode Bode Plot

A.4 Controller Lab Results

Table A.1:   Lab Results for All Tested PPF Controllers

Controller	Design Parameters (Front System)			Design Parameters (Aft System)			IGM	IPM	Accelerometer Vibration Reduction (dB)				FWD Sensor Vibration Reduction (dB)				AFT Sensor Vibration Reduction (dB)				Max Control (V)			
	Freq	Gain	Damping	Freq	Gain	Damping			Mode 1	Mode 2	Mode 3	Mode 4	Mode 1	Mode 2	Mode 3	Mode 4	Mode 1	Mode 2	Mode 3	Mode 4	U1	U2	U3	U4
SISO PPF (Two Mode)	94.2	0.09	0.2	159.14	0.05	0.2	11.5	21.5	1.16	16.14	14.03	-1.55	3.08	18.15	13.35	-3.09	0.75	16.37	15.17	-1.42	690.0	668.7	690.0	668.7
	93.36	0.05	0.2	158.82	0.05	0.2	11.5	21.5	3.41	13.55	15.43	-0.63	3.21	14.26	15.09	-1.97	2.75	14.2	16.52	-1.52	577.1	668.5	577.1	668.5
	93.36	0.08	0.2	158.86	0.02	0.1	12.5	22.4	-0.44	22.23	9.61		1.72	26.48	8.56		1.95	21.76	9.96		891.0	392.0	891.0	392.0
	93.36	0.08	0.2	158.84	0.08	0.2	10.4	20.4	-1.38	18.2	18.95		1.81	20.09	19.71		4.96	19.6	21.32		857.1	991.7	857.1	991.7
	93.36	0.1	0.2	158.87	0.1	0.2	9.23	19.1	5.04	18.68	20.72	-0.69	4.77	20.99	20.55	-3.74	8.43	19.56	23.65	-1.37	1037.4	1175.5	1037.4	1175.5

Controller	Design Parameters (Front System)			Design Parameters (Aft System)			IGM	IPM	Accelerometer Vibration Reduction (dB)				FWD Sensor Vibration Reduction (dB)				AFT Sensor Vibration Reduction (dB)				Max Control (V)			
	Freq	Gain	Damping	Freq	Gain	Damping			Mode 1	Mode 2	Mode 3	Mode 4	Mode 1	Mode 2	Mode 3	Mode 4	Mode 1	Mode 2	Mode 3	Mode 4	U1	U2	U3	U4
SISO PPF (Four Mode)	94.20, 212.59	0.04, 0.04	0.2, 0.2	68.35, 159.14	0.063, 0.063	0.2, 0.2	12.1	22	6.92	13.3	14.09	0.27	6.03	16.81	14.73	2.06	10.7	13.9	13.6	-0.124	663.57	647.95	663.57	647.95
	94.20, 212.60	0.035, 0.035	0.2, 0.2	68.35, 159.15	0.04, 0.04	0.2, 0.2	15.7	24.7	6.31	8.74	12.42	-1.02	4.02	10.57	12.67	-0.47	9.56	9.25	12.23	-1.97	691.3	646.4	691.3	646.4
	94.20, 212.61	0.04, 0.03	0.2, 0.2	68.35, 159.16	0.04, 0.04	0.2, 0.2	16.3	25.1	7.36	10.09	13.32	0.22	5.17	11.97	13.13	0.5	10.72	10.47	13.05	-0.96	691.4	649.2	691.4	649.2

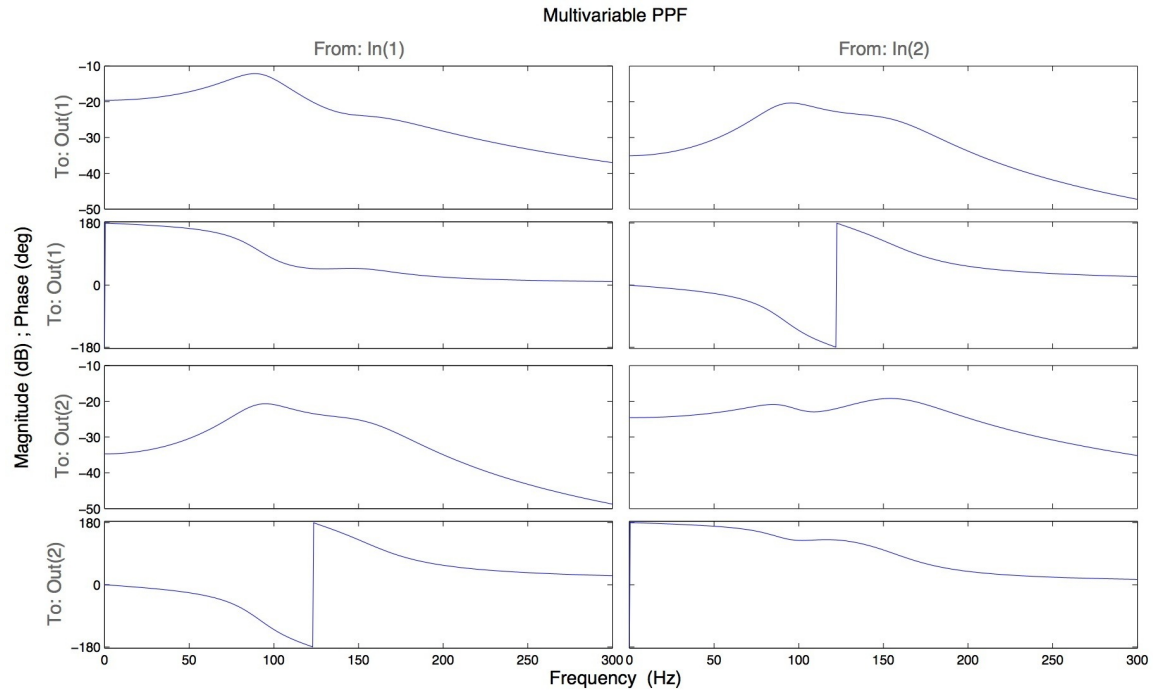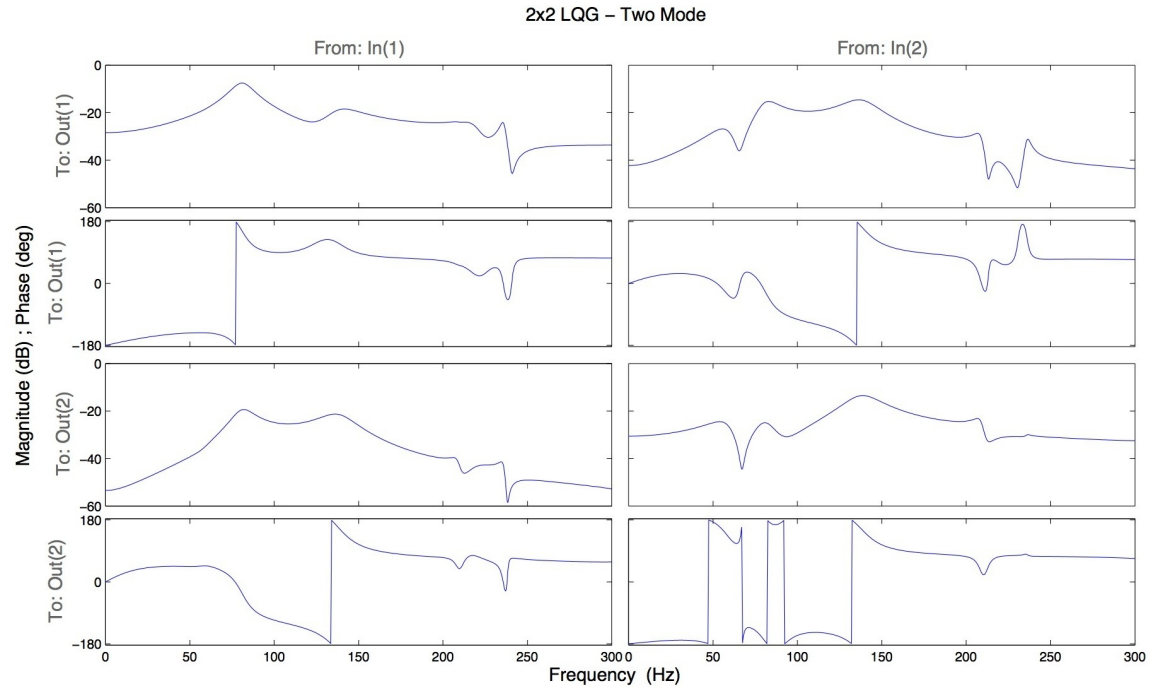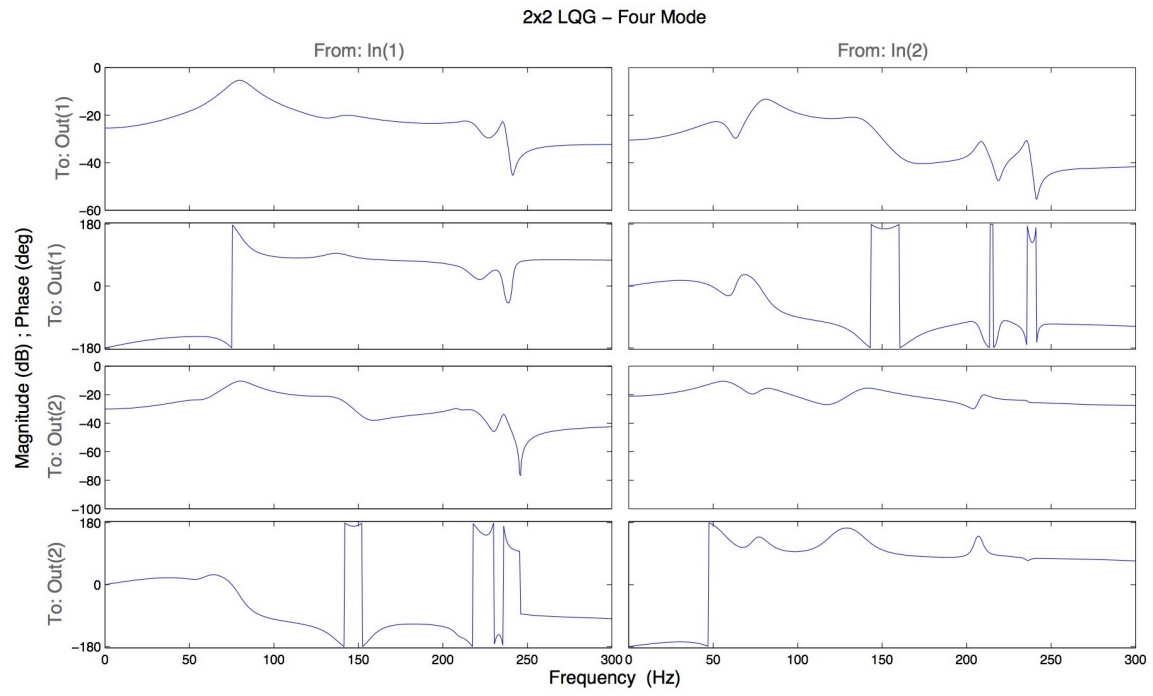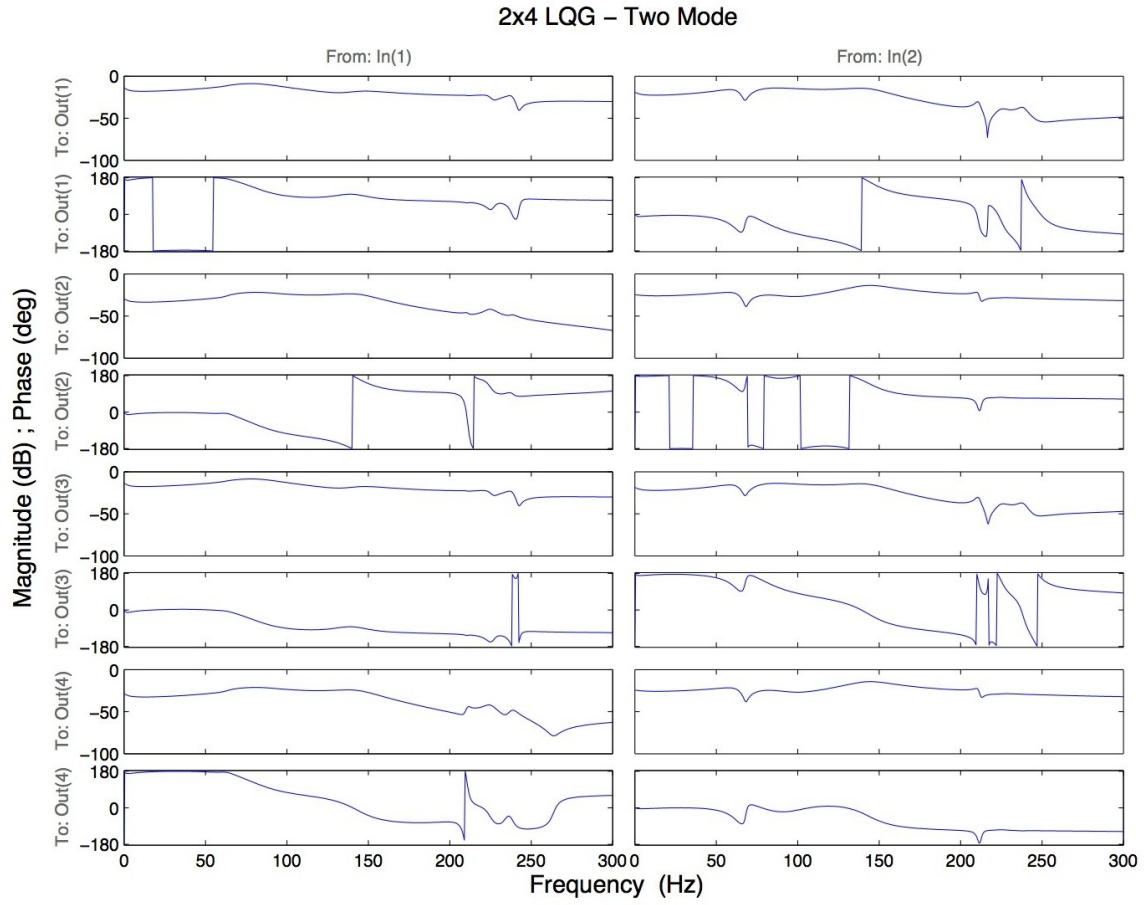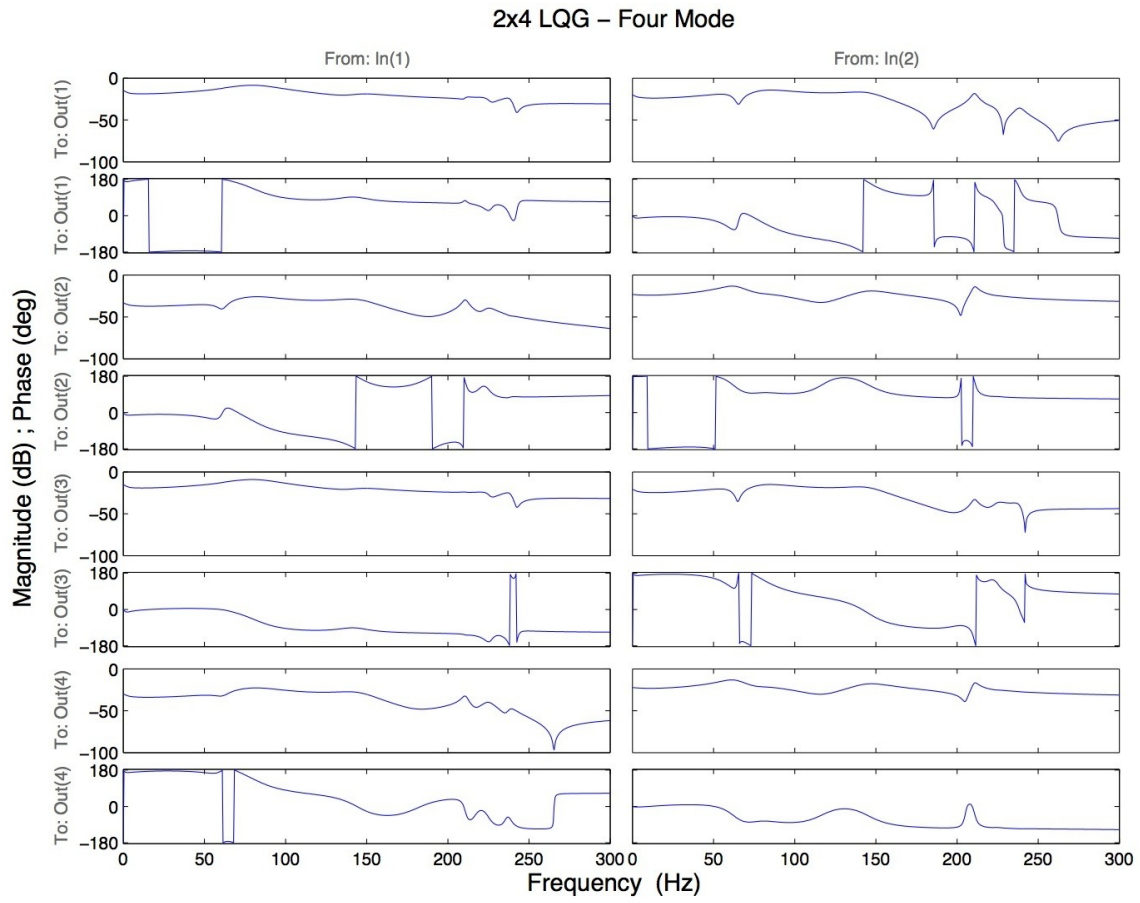| Controller	Design Parameters (Front System)			Design Parameters (Aft System)			IGM	IPM	Accelerometer Vibration Reduction (dB)				FWD Sensor Vibration Reduction (dB)				AFT Sensor Vibration Reduction (dB)				Max Control (V)			
	Freq	Gain	Damping	Freq	Gain	Damping			Mode 1	Mode 2	Mode 3	Mode 4	Mode 1	Mode 2	Mode 3	Mode 4	Mode 1	Mode 2	Mode 3	Mode 4	U1	U2	U3	U4
Multivariable PPF	94.2	0.06	0.2	159.14	0.03	0.2	10.2	20.2	1.13	18.79	16.17	-1.19	4.4	21.47	18.08	-3.78	3.33	19.29	17.54	-0.44	606.3	656.8	606.3	656.8
	93.36	0.025	0.2	158.81	0.025	0.2	12.4	22.4	2.24	13.59	15.82	-0.49	3.49	14.21	17.03	-2.37	2.15	13.35	16.82	-1.09	561.10	622.10	561.10	622.10
	93.36	0.08	0.2	158.9	0.035	0.1	8.41	18.1	2.6	22.73	23.57	-0.34	6.74	26.58	28.16	-3.73	7.31	23.75	27.96	-2.11	1177.7	1055.8	1177.7	1055.8
	93.36	0.08	0.2	158.91	0.08	0.2	7.52	16.8	2.94	22.71	23.88	-0.38	4.9	26.45	28.12	-3.88	13.95	23.74	28.95	5.04	1344.3	1715.4	1344.3	1715.4

Table A.2:   Lab Results for All Tested LQG Controllers

Controller	Frequencies	State Weighting Matrix	Control Weighting Matrix	q	IGM	IPM	Accelerometer Vibration Reduction (dB)				FWD Sensor Vibration Reduction (dB)				AFT Sensor Vibration Reduction (dB)				Max Control (V)			
							Mode 1	Mode 2	Mode 3	Mode 4	Mode 1	Mode 2	Mode 3	Mode 4	Mode 1	Mode 2	Mode 3	Mode 4	U1	U2	U3	U4
LQG 2x2 (Two Mode)	94.20, 159.14	[0 0 1 1 1 1 0 ... 0]	[600 1300]	1	20.9	27	-1.02	18.35	17.09	-0.13	0.1	20.9	21.11	-1.6	1.39	18.4	18.79	0.53	606.26	659.79	606.26	659.79
	93.36, 158.69	[0 0 1 1 1 1 0 ... 0]	[100 100]	1	15.3	24	-2.03	26.13	26.26	0.53	3.48	30.23	36.14	-1.65	2.42	28.07	32.78	1.81	1634.4	1831.5	1634.4	1831.5
	93.36, 158.70	[0 0 1 1 1 1 0 ... 0]	[1000 1000]	1	22.6	28	0.53	18.55	18.84	-0.02	0.36	19.93	22.15	-1.22	7.64	19.13	20.83	-0.37	805.3	909.5	805.3	909.5
	93.36, 158.71	[0 0 1 1 1 1 0 ... 0]	[2500 2500]	1	29.3	29	0.69	14.69	15.61	0.52	0.91	15.68	17.5	-0.19	2.99	14.81	16.73	-0.29	550.6	638.8	550.6	638.8
	93.36, 158.72	[0 0 1 1 1 1 0 ... 0]	[2500 2500]	10	22.2	28	2.68	16.75	16.74	0.88	0.05	17.92	19.14	0.69	2.23	16.8	18.14	-0.05	940.0	918.0	940.0	918.0
	93.36, 158.73	[0 0 1 1 1 1 0 ... 0]	[2500 2500]	100	22.4	28	2.19	16.67	16.93	0.96	-0.1	17.85	19.32	0.21	3.86	16.96	18.27	-0.14	951.3	937.6	951.3	937.6
	93.36, 158.74	[0 0 1 1 1 1 0 ... 0]	[2500 2500]	1000	22.4	28	2.48	16.85	16.93	0.91	0.34	18.09	19.45	0.7	2.68	16.91	18.34	0.35	951.0	936.6	951.0	936.6
	93.36, 158.75	[0 0 1 1 1 1 0 ... 0]	[40 40]	1	11.9	22	-0.99	26.71	28.05	2.27	6.74	35.35	34.73	1.04	3.46	29.02	39.34	5.5	1991.0	2230.1	1991.0	2230.1
	93.36, 158.76	[0 0 1 1 1 1 0 ... 0]	[500 500]	1	25.6	28	5.94	21.36	21.38	0.23	1.15	23.41	27.07	-1.38	12.19	22.22	24.46	-0.04	1021.4	1180.5	1021.4	1180.5

Controller	Frequencies	State Weighting Matrix	Control Weighting Matrix	q	IGM	IPM	Accelerometer Vibration Reduction (dB)				FWD Sensor Vibration Reduction (dB)				AFT Sensor Vibration Reduction (dB)				Max Control (V)			
							Mode 1	Mode 2	Mode 3	Mode 4	Mode 1	Mode 2	Mode 3	Mode 4	Mode 1	Mode 2	Mode 3	Mode 4	U1	U2	U3	U4
LQG 2x4 (Two Mode)	94.20, 159.14	[0 0 0 0 5 5 1 1 0 ... 0]	[250 600 300 700]	1	9.35	19	-1.6	20.51	18.6	-0.43	2.08	24.81	24.55	-1.42	1.7	21.04	20.82	-1.14	633.1	684.6	648.6	653.3
	94.20, 159.14	[0 0 0 0 10 10 1 1 0 ... 0]	[1500 2000 2000 2000]	1	10.3	20	0.0	19.74	16.32	0.16	1.53	23.13	19.32	-0.9	7.68	21.65	17.83	-1.86	615.9	536.6	571.3	601.4

Controller	Frequencies	State Weighting Matrix	Control Weighting Matrix	q	IGM	IPM	Accelerometer Vibration Reduction (dB)				FWD Sensor Vibration Reduction (dB)				AFT Sensor Vibration Reduction (dB)				Max Control (V)			
							Mode 1	Mode 2	Mode 3	Mode 4	Mode 1	Mode 2	Mode 3	Mode 4	Mode 1	Mode 2	Mode 3	Mode 4	U1	U2	U3	U4
LQG 2x2 (Four Mode)	68.35, 94.20, 159.14, 212.59	[1 1 10 10 1 1 1 0 ... 0]	[2500 2100]	1	20.3	27	7.04	18.48	14.96	3.21	6.45	24.27	14.61	3.12	17.13	20.03	14.93	3.85	672.5	673.1	672.5	673.1
	68.35, 94.20, 159.14, 212.59	[1 1 1 1 1 1 1 0 ... 0]	[2500 2500]	1	25.3	28	8.48	13.51	14.55	2.91	4.09	14.93	14.04	3.12	14.06	13.6	14.54	3.43	610.4	659.6	610.4	659.6

Controller	Frequencies	State Weighting Matrix	Control Weighting Matrix	q	IGM	IPM	Accelerometer Vibration Reduction (dB)				FWD Sensor Vibration Reduction (dB)				AFT Sensor Vibration Reduction (dB)				Max Control (V)			
							Mode 1	Mode 2	Mode 3	Mode 4	Mode 1	Mode 2	Mode 3	Mode 4	Mode 1	Mode 2	Mode 3	Mode 4	U1	U2	U3	U4
LQG 2x4 (Four Mode)	68.35, 94.20, 159.14, 212.59	[0 0 1 1 10 10 1 1 1 0 ... 0]	[600 1800 800 1700]	1	9.4	19	7.41	17.73	15.74	3.22	6.99	23.94	15.38	9.14	14.57	18.88	15.26	6.79	674.5	640.5	626.2	625.3
	68.35, 94.20, 159.14, 212.59	[0 0 1 1 1 1 1 1 1 0 ... 0]	[2500 2500 2500 2500]	1	18.6	26	9.63	12.57	14.28	4.37	4.98	13.96	13.65	5.87	14.24	12.8	14.09	6.28	266.0	634.2	323.7	598.2
	68.35, 94.20, 159.14, 212.60	[0 0 1 1 10 10 1 1 1 0 ... 0]	[2500 2500 2500 2500]	1	11.1	21	8.41	17.46	14.39	3.86	5.68	21.27	14	5.31	14.91	18.81	14.23	5.67	512.5	578.6	650.7	544.4
	68.35, 94.20, 159.14, 212.60	[0 0 1 1 10 10 1 1 1 0 ... 0]	[2500 2500 2500 2500]	1	11.1	21	1.77	19.56	14.57	-0.66	1	22.28	16.39	-1.7	17.06	20.37	15.57	5.29	512.5	578.6	650.7	544.4

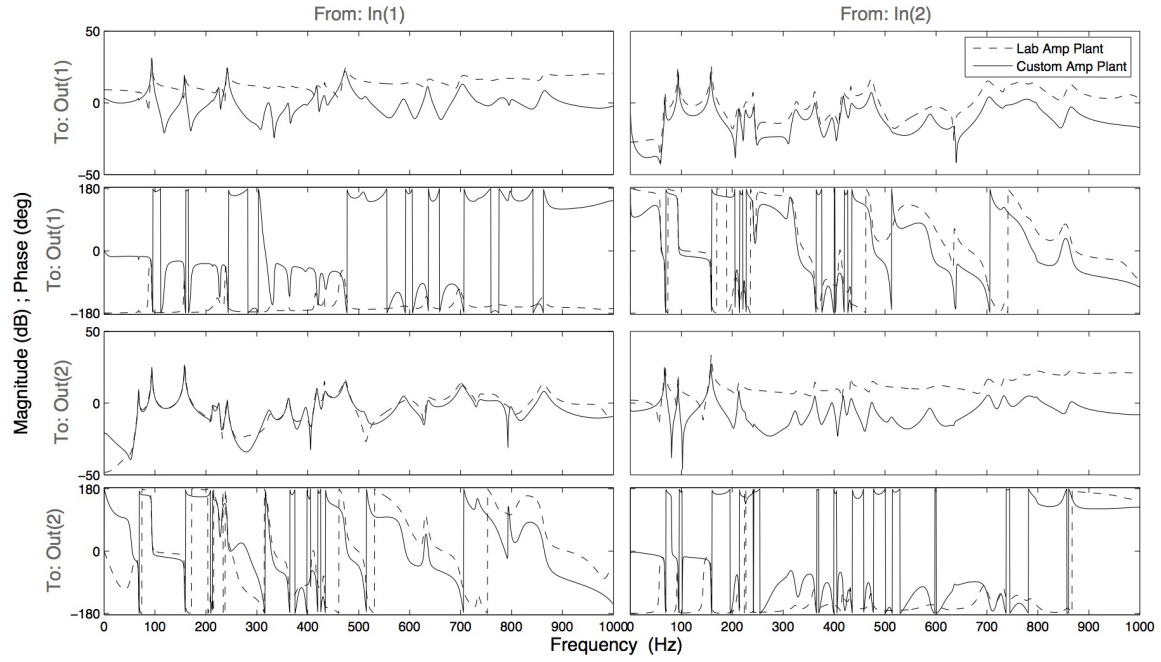## A.5   Custom Amplifier Plant Bode Plots

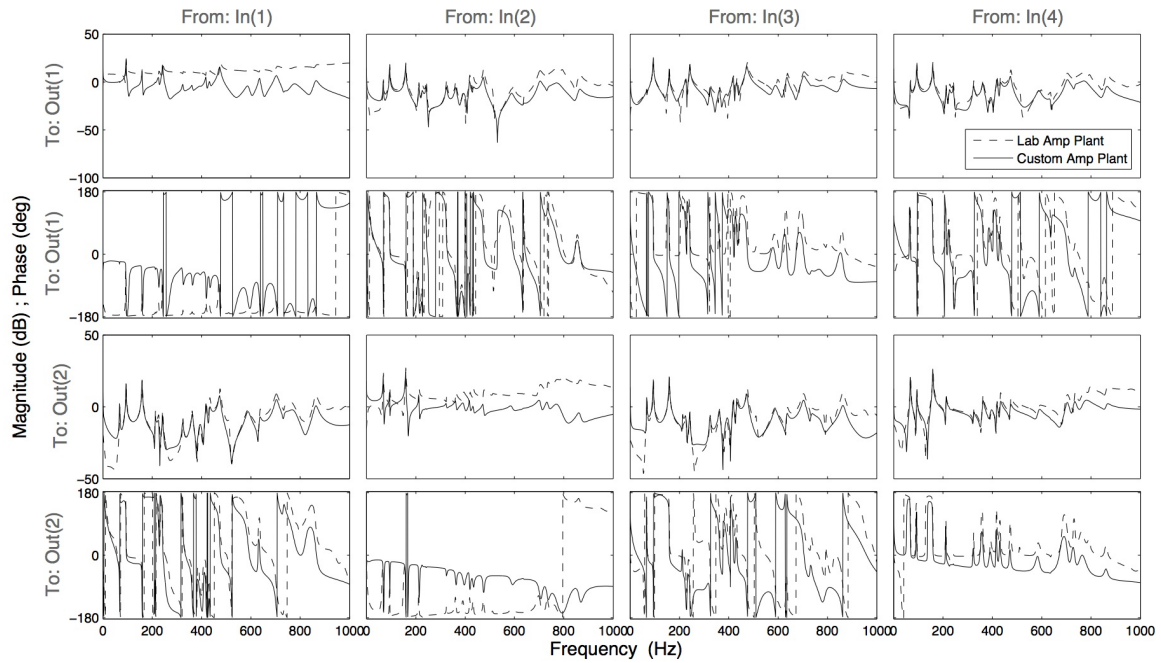Figure A.11:   Comparison of 2×2 Plant Models

Figure A.12:   Comparison of 4×2 Plant Models

Bibliography

1. "Charge attenuator for electrical charge signals," Kistler Instrumente AG, Amherst, NY, Data Sheet 5361A-000-326e-08.07, no date.

2. "Microautobox II," dSPACE GmbH, Paderborn, Germany, Data Sheet, 2010.

3. "Model 2771c remote charge converter." Endevco Corporation, San Juan Capistrano, CA, Data Sheet, no date.

4. "Piezoelectric measurement system comparison: Charge mode vs. low impedance voltage mode (lvim)," Dytran Instruments, Inc., Chatsworth, CA, 2010.

5. L. K. Austin and M. van den Bergh, "Implementation of new materials on aging aircraft structure," in *New Metallic Materials for the Structure of Aging Aircraft*, Corfu, Greece, 1999.

6. P. Avitabile, "Experimental modal analysis a simple non-mathematical presentation," *S V Sound and Vibration*, vol. 35, no. 1, pp. 20–31, 2001.

7. M. C. Brennan and A.-M. R. McGowan, "Piezoelectric power requirements for active vibration control," in *Smart Structures and Materials 1997: Mathematics and Control in Smart Structures*, vol. 3039, San Diego, CA, 1997, pp. 660–669.

8. J. Browning, S. Teo, C. Buckley, C. Seager, and L. Haubelt, "Active fin: F-16 ventral fin buffet alleviation using piezoelectric actuators." Air Force Flight Test Center, Edwards AFB, CA, Technical Information Memorandum AFFTC-TIM-09-06, 2009.

9. J. Browning, "F-16 ventral fin buffet alleviation using piezoelectric actuators," M.S. thesis, School of Engineering and Management, Air Force Institute of Technology, Wright-Patterson AFB, OH, 2009.

10. J. B. Burl, *Linear optimal control: H.* Menlo Park, CA: Addison Wesley Longman, 1999.

11. S. Chandrasekaran and D. K. Lindner, "Power flow through controlled piezoelectric actuators," *Journal of Intelligent Material Systems and Structures*, vol. 11, no. 6, pp. 469–481, 2000.

12. R. Cobb, "State-space model identification using the eigensystem realization algorithm toolbox for MATLAB®". Software User Interface, Nov 2003. Version 1.1.

13. J. W. Dally and W. F. Riley, *Experimental stress analysis*, 3rd ed. New York, NY: McGraw-Hill, 1991.

14. S. J. Dyke, B. F. Spencer, P. Quast, M. K. Sain, D. C. Kaspari, and T. T. Soong, "Experimental verification of acceleration feedback control strategies for an active

tendon system," National Center for Earthquake Engineering Research, Buffalo, NY, Tech. Rep. NCEER-94-0024, 1994.

15. J. L. Fanson and T. K. Caughey, "Positive position feedback control for large space structures," *AIAA Journal*, vol. 28, no. 4, pp. 717–724, 1990.

16. J. Fei and Y. Wang, "Active vibration control of a flexible structure using optimal control and piezoelectric actuators," *Advances in Modelling & Analysis C: Systems Analysis, Control & Design Simulation, CAD*, vol. 61, no. 4, pp. 57–66, 2006.

17. M. Q. Feng and A. Mita, "Vibration control of tall buildings using mega subconfiguration," *Journal of Engineering*, vol. 121, no. 10, p. 1082, 1995.

18. C. J. Goh and T. K. Caughey, "On the stability problem caused by finite actuator dynamics in the collocated control of large space structures," *International Journal of Control*, vol. 41, no. 3, pp. 787–802, 1985.

19. S. Hanagud, "F-15 tail buffet alleviation: A smart structure approach," Georgia Institute of Technology, Atlanta, GA, Tech. Rep. F33615-96-C-3204, 1998.

20. J. Honda and J. Adams, "Class D audio amplifier basics," International Rectifiers, El Segundo, CA, 2005.

21. J. N. Juang and R. S. Pappa, "An eigensystem realization alogrithm for modal parameter identification and model reduction," *Journal of Guidance, Control, and Dynamics*, vol. 8, no. 5, pp. 620–627, 1985.

22. K. Krishnamurthy and M. C. Chao, "Active vibration control during deployment of space structures," *Journal of Sound and Vibration*, vol. 152, no. 2, p. 205, 1992.

23. M. K. Kwak, "Real-time multiple-parameter tuning of ppf controllers for smart structures by genetic algorithms," *Proceedings of SPIE, the international society for optical engineering*, vol. 3984, p. 279.

24. M. K. Kwak and S. Heo, "Active vibration control of smart grid structure by multiinput and multioutput positive position feedback controller," *Journal of Sound and Vibration*, vol. 304, no. 1-2, pp. 230–245, 2007.

25. C. R. Larson, E. Falanges, S. K. Dobbs, R. R. Neurgaonkar, J. G. Nelson, J. S. Rosenthal, C. L. Hustedde, and S. F. McGrath, "Piezoceramic active vibration-suppression control system development for the b-1b aircraft," in *Smart Structures and Materials 1998: Industrial and Commercial Applications of Smart Structures Technologies*, vol. 3326, 1998, pp. 294–305.

26. Y. Luo, S. Xie, and X. Zhang, "The actuated performance of multi-layer piezoelectric actuator in active vibration control of honeycomb sandwich panel," *Journal of Sound and Vibration*, vol. 317, no. 3-5, pp. 496–513, 2008.

27. J. L. McFarland and R. Perez, "F-15 structural life enhancement," in *Ageing Mechanisms and Control. Specialists' Meeting on Life Management Techniques for Ageing Air Vehicles*, Manchester, UK, 2003.

28. S. O. R. Moheimani, B. J. G. Vautier, and B. Bhikkaji, "Experimental implementation of extended multivariable ppf control on an active structure," *Control Systems Technology, IEEE Transactions on*, vol. 14, no. 3, pp. 443–455, 2006.

29. S. D. Morgenstern, "Alleviation of buffet-induced vibration using piezoelectric actuators," M.S. thesis, School of Engineering and Management, Air Force Institute of Technology, Wright-Patterson AFB, OH,2006.

30. S. D. Morgenstern, H. C. Giebner, D. Wong, A. A. Tucker, and A. Violetti, "Limited characterization of dual bimorph synthetic jet actuators: Aeroelastic load control - phase i (project have puff)," Air Force Flight Test Center, Edwards AFB, CA, Tech. Rep. AFFTC-TIM-05-07, 2005.

31. R. W. Moses, "Active vertical tail buffeting alleviation on a twin-tail fighter configuration in a wind tunnel," NASA Langley Technical Report Server, Hampton, VA, Tech. Rep., 1997.

32. I. K. Peddle, "Discrete state space control," in *Control Systems 414*, Dublin City University, Dublin, Ireland, 2007.

33. D. M. Pitt, M. J. Thomas, and S. L. Liquore, "Air vehicles technology integration program (avtip)," Air Vehicles Directorate, Air Force Research Laboratory, Wright-Patterson AFB, OH, Tech. Rep. AFRL-VA-WP-TR-2006-3005, 2005.

34. A. Preumont, *Vibration control of active structures: an introduction*, 2nd ed. Boston, MA: Kluwer Academic Publishers, 2002.

35. P. Ret, "F-16 block 40 ventral fin failure (failure analysis)," University of Dayton Research Institute, Dayton, OH, Evaluation Report WL/MLS 97-062, 1997.

36. D. B. Ridgely and S. S. Banda, "Introduction to robust multivariable control," Flight Dynamics Laboratory, Wright-Patterson AFB, OH, Tech. Rep. AFWAL-TR-85-3102, 1986.

37. M. Schussler, "Measurement of 2d dynamic stress distributions with a 3d-scanning laser doppler vibrometer," *Modal Analysis Topics, Volume 3: Proceedings of the 29th IMAC, A Conference on Structural Dynamics 2011*, vol. 3, pp. 141–151, 2011.

38. V. Shankar, B. V. Nagaraja, R. Balasubramaniam, A. S. Sethuram, and S. N. Muthaiah, "System design for active vibration control of aerospace structures," in *Proceedings of SPIE*, vol. 5062, 2003, pp. 530–537.

39. E. F. Sheta, "Alleviation of vertical tail buffeting of f/a-18 aircraft," *Journal of Aircraft*, vol. 41, no. 2, pp. 322–330, 2004.

40. J. Sirohi and I. Chopra, "Fundamental understanding of piezoelectric strain sensors," *Journal of Intelligent Material Systems and Structures*, vol. 11, pp. 246–257, 2000.

41. J. H. van Tongeren, "F-16 ventral fin analysis," National Aerospace Laboratory, Netherlands, Tech. Rep. NLR-CR-99366, 1999.

42. J. Zhang, L. He, E. Wang, and R. Gao, "A lqr controller design for active vibration control of flexible structures," in *Computational Intelligence and Industrial Application, 2008. PACIIA '08. Pacific-Asia Workshop on*, vol. 1, 2008, pp. 127–132.

Vita

Captain Tomoyuki D. Ono graduated from Brookline High School in Brookline, Massachusetts. He entered undergraduate studies at the University of Michigan in Ann Arbor, Michigan where he graduated with a Bachelor of Science degree in Aerospace Engineering in April 2005. He completed a four year Reserve Officer Training Corps program during his undergraduate program and commissioned as a Second Lieutenant.

Following ICBM operator training, Captain Ono was assigned to the 10th Missile Squadron at Malmstrom AFB, MT. There he served as an ICBM combat crew operator, instructor and eventually as a senior evaluator.

In early 2009 he was selected to the Air Force Institute of Technology (AFIT) and USAF Test Pilot School (TPS) joint program and attended AFIT for his Master of Science degree in Aeronautical Engineering. He attended the USAF TPS Class 11A in 2011 and completed a year long course to obtain a Master of Science degree in Flight Test Engineering and was certified as an Experimental Flight Test Engineer (FTE). Upon completion of this thesis and graduation from AFIT, Captain Ono will be assigned to the 780th Test Squadron, Eglin AFB, CA as an FTE.

Permanent address: 2950 Hobson Way
Air Force Institute of Technology
Wright-Patterson AFB, OH 45433

REPORT DOCUMENTATION PAGE

Public reporting burden for this collection of information is estimated to average 1 hour per response, including the time for reviewing instructions, searching data sources, gathering and maintaining the data needed, and completing and reviewing the collection of information. Send comments regarding this burden estimate or any other aspect of this collection of information, including suggestions for reducing this burden to Washington Headquarters Service, Directorate for Information Operations and Reports, 1215 Jefferson Davis Highway, Suite 1204, Arlington, VA 22202-4302, and to the Office of Management and Budget, Paperwork Reduction Project (0704-0188) Washington, DC 20503.

PLEASE DO NOT RETURN YOUR FORM TO THE ABOVE ADDRESS.

1. REPORT DATE (DD-MM-YYYY) 22-03-2012	2. REPORT TYPE Master's Thesis	3. DATES COVERED (From - To) January 2010 – March 2012

4. TITLE AND SUBTITLE
Application of Multi-Input Multi-Output Feedback Control for F-16 Ventral Fin Buffet Alleviation Using Piezoelectric Actuators

5a. CONTRACT NUMBER

5b. GRANT NUMBER

5c. PROGRAM ELEMENT NUMBER

6. AUTHOR(S)
Ono, Tomoyuki D., Captain, USAF

5d. PROJECT NUMBER
11Y144B, 12Y388

5e. TASK NUMBER

5f. WORK UNIT NUMBER

7. PERFORMING ORGANIZATION NAME(S) AND ADDRESS(ES)
Air Force Institute of Technology
Graduate School of Engineering and Management (AFIT/EN)
2950 Hobson Way
WPAFB OH 45433-7765

8. PERFORMING ORGANIZATION REPORT NUMBER
AFIT/GAE/ENY/12-M31

9. SPONSORING/MONITORING AGENCY NAME(S) AND ADDRESS(ES)
USAF Test Pilot School
Attn: Maj. Clinton J. Armani
220 S. Wolfe Ave
Edwards AFB, CA 93524
(937) 277-3000 clinton.armani@edwards.af.mil

10. SPONSOR/MONITOR'S ACRONYM(S)
USAF TPS

11. SPONSORING/MONITORING AGENCY REPORT NUMBER

12. DISTRIBUTION AVAILABILITY STATEMENT
APPROVED FOR PUBLIC RELEASE; DISTRIBUTION IS UNLIMITED

13. SUPPLEMENTARY NOTES
This material is declared a work of the U.S. Government and is not subject to copyright protection in the United States.

14. ABSTRACT

Control of structural vibrations has been a popular topic. Use of MFC piezoelectric actuators and co-located sensors allows for an active rather than passive control method. The F-16 ventral fin is susceptible to buffet induced vibrations and is a perfect test structure for active vibration control for flight-testing. The research follows the previous ACTIVE FIN project and improves on the design by increasing the number of actuator layers, available actuator power, and using multi-input multi-output (MIMO) control algorithms. The research involved experimental identification of the ventral fin and its principle strain directions, selection of system components, determination of mathematical plant model, and design and test of control algorithms. The research resulted in a control system suitable for flight, a practical controller design process, and comparisons of different control algorithms to include single-input single-output (SISO) positive position feedback (PPF), multivariable PPF, two-input two-output linear quadratic Gaussian (LQG), and two-input four-output LQG. Controller effectiveness on target modes, actuator power consumption, and controller robustness were tested in the laboratory. The laboratory results showed that reductions of 7.4 dB, 17.7 dB, 15.7 dB and 3.2 dB in modes one, two, three, and four respectively were achieved using the MIMO LQG controller while maintaining sufficient gain and phase margins.

15. SUBJECT TERMS
active control, structural vibration suppression, MIMO, ventral fin, piezoelectric actuator, positive position feedback, linear quadratic gaussian

16. SECURITY CLASSIFICATION OF:			17. LIMITATION OF ABSTRACT UU	18. NUMBER OF PAGES 126	19a. NAME OF RESPONSIBLE PERSON Dr. Richard Cobb (ENY)
a. REPORT U	b. ABSTRACT U	c. THIS PAGE U			19b. TELEPONE NUMBER (Include area code) (937) 255-3636, x4559 richard.cobb@afit.edu

Standard Form 298 (Rev. 8-98)
Prescribed by ANSI-Std Z39-18